

University of Southern Queensland
Faculty of Engineering and Surveying

Examining the Re-entry of a Tumbling Object During Freefall

A dissertation submitted by

Gregory Hartmann

in fulfilment of the requirements of

ENG4111 and ENG4112 Research Project

towards the degree of

**Bachelor of Engineering (Mechanical) (Honours) and Bachelor of
Science (Physical Sciences)**

Submitted October, 2021

Abstract

A humanity continues to advance its knowledge and understandings in the field of science, technology and engineering, society will always continue to push and redefine their limitations and approaches towards gaining this knowledge and understanding of the universe. This includes but is not limited to the research related to astronomical studies, planetary bodies and the commercialisation of the space industry. However, there are problems that arise from these advancements, one of which is the risks and hazards associated with launching, monitoring, tracking and deorbiting of old spacecraft and debris orbiting the Earth. These risks and hazards are currently being observed today, where one of the most recent uncontrolled atmospheric re-entries occurred on the 8th May 2021. Which involved the core 5B booster from the Chinese Long Mach CZ-5B rocket, where it re-entered and performed an uncontrolled re-entry into the Earth's atmosphere. Due to the uncontrolled re-entry of this object, private and government institutions struggled to determine the exact location for where the object would make impact. Therefore, this uncertainty increases the risks and likelihood of an object impacting and damaging a populated area. This research project identifies and examines the effect and trajectory of spacecrafts or pieces of debris that have re-entered into the Earth's atmosphere in an uncontrolled flight path. Therefore, main aim of this research project is to design an apparatus that can artificially simulate and examine the re-entry trajectory of an object tumbling at high speed during freefall from orbit within a hypersonic wind tunnel.

In order to conduct this research project, the limitations and design requirements for the proposed apparatus needed to be outlined and established before testing could commence. This was achieved by examining the design of the TUSQ facility and the release mechanism. These limitations were then used in design stages of the apparatus and were used to explore three possible apparatus designs, however, only one was utilised in this project. In addition, these limitations and operating conditions of the TUSQ facility was also utilised in the theoretical calculations used to determine the mass, drag force, frictional force and the force applied to the test objects during the project.

Further, the apparatus underwent three stages of testing before the final test could be performed. These were the freefall test, the performance test and the preliminary/bench test performed at the TUSQ facility. Initially four different test objects were going to be tested within the hypersonic wind tunnel, however, only one object (cube) was tested. This was due to time restraints.

After conducting the final test within the TUSQ facility at USQ Toowoomba, Queensland and analysing the collected results, the results revealed the following; the calculated RPM and the drag coefficient of the test object and the temperature, pressure and density of the fluid's flow was approximately 6975.22, 1.33, 70.33 K, 772.35 Pa and 0.0000048 kg/m³, respectively. Furthermore,

when comparing the RPM and drag coefficient back to the theoretical data used in the design stage of this research project, there was a calculated percentage error of approximately 52.19, and 26.67, respectively. However, due to some errors the accuracy of the data may have affected the final results. These include; the increase surface area that the fluid's flow has on the test object, as the object continues to change its angle of attack, the increase voltage supplied to the motor and speed controller, the accuracy of the dimensions of the test object, the positioning of the test object with respect to the centre of gravity of the apparatus, the interference from the separation of the test platform and the test object and the effect from the vibration from the DC motor.

University of Southern Queensland
Faculty of Health, Engineering and Sciences
ENG4111/ENG4112 Research Project

Limitations of Use

The Council of the University of Southern Queensland, its Faculty of Health, Engineering & Sciences, and the staff of the University of Southern Queensland, do not accept any responsibility for the truth, accuracy or completeness of material contained within or associated with this dissertation.

Persons using all or any part of this material do so at their own risk, and not at the risk of the Council of the University of Southern Queensland, its Faculty of Health, Engineering & Sciences or the staff of the University of Southern Queensland.

This dissertation reports an educational exercise and has no purpose or validity beyond this exercise. The sole purpose of the course pair entitled “Research Project” is to contribute to the overall education within the student’s chosen degree program. This document, the associated hardware, software, drawings, and other material set out in the associated appendices should not be used for any other purpose: if they are so used, it is entirely at the risk of the user.

University of Southern Queensland
Faculty of Health, Engineering and Sciences
ENG4111/ENG4112 Research Project

Certification of Dissertation

I certify that the ideas, designs and experimental work, results, analyses and conclusions set out in this dissertation are entirely my own effort, except where otherwise indicated and acknowledged.

I further certify that the work is original and has not been previously submitted for assessment in any other course or institution, except where specifically stated.

Gregory Hartmann



Acknowledgements

I would like to acknowledge and thank my supervisor Professor David Buttsworth for guiding and advising myself throughout this year and also providing me with the opportunity for perusing this research project. I would also like to thank all of the staff members from P and Z Block at the University of Southern Queensland Toowoomba campus who helped me with the final testing phase of my project and for providing me with the resources and equipment necessary to complete this project.

I would also like to acknowledge and thank Grahame Walker for the use of his resources and equipment that were necessary to complete this project. And to thank all of my friends and family for supporting myself. I would also like to thank my partner Tayla for her patience and support throughout the year.

Table of Contents

Abstract	2
Limitations of Use.....	4
Certification of Dissertation.....	5
Acknowledgements.....	6
Table of Contents.....	7
List of Figures	10
List of Tables	13
Nomenclature	14
Table of Mathematical Symbols	15
Chapter 1 - Introduction.....	17
1.1 Preamble	17
1.2 Introduction.....	17
1.3 The Problem.....	19
1.4 Research Objective	20
1.5 Project Methodology.....	20
1.6 Consequential Effects	21
1.7 Summary	22
Chapter 2 - Literature Review.....	23
2.1 Introduction.....	23
2.2 Space Industry.....	23
2.2.1 Market.....	24
2.3 Drag and lift forces	25
2.3.1 Drag Force	27
2.3.2 Lift.....	29
2.3.3 Flow Types and the propagation of the Mach Cone	29
2.3.4 Isentropic Stagnation Properties Flow	30
2.3.5 Supersonic/Hypersonic Flow	31
2.4 Re Entry	34
2.4.1 Re-entry Calculations.....	36
2.5 Academic Literature.....	38
2.5.1 Literature Knowledge and Gap	41
2.6 Summary	42

Chapter 3 – Project Design and Methodology	43
3.1 Introduction.....	43
3.2 Design Overview – Testing Facility	43
3.2.1 Design Options.....	45
3.3 Final Design.....	46
3.3.2 Apparatus Design and Limitations.....	47
3.3.2 Test Objects	48
3.4 Testing Procedure	51
3.5 Theoretical Design Calculations for the Test Objects	52
3.6 Conclusion	54
4 Results and Discussion	55
4.1 Introduction.....	55
4.2 Preliminary Results.....	55
4.3 Final Test Results.....	62
4.3.1 Experimental Calculations	73
4.4 Discussion	81
4.5 Summary	82
5 Conclusion and Recommendation	83
5.1 Introduction.....	83
5.2 Conclusion	83
5.3 Recommendations.....	86
5.3.1 Recommendations Related to this Research Project.....	86
5.3.3 Future Work and Experimental Recommendations	87
5.4 Summary	88
Appendix	89
Appendix A – Project Specification	89
Appendix B – Concept Designs.....	90
Appendix C – Preliminary Methodology.....	92
Appendix C.1 Resource Planning	94
Appendix C.2 Preliminary Risk Assessment	95
Appendix D – Apparatus Schematics	97
Appendix E – Test Objects Schematics	100
Appendix F Preliminary/Bench and Final Test Snapshot Breakdown	104

Appendix F.1 Final Test	106
Appendix F.2 Preliminary/Bench Test Load 20 Percent	112
Appendix F.3 Preliminary/Bench Test Load 30 Percent	114
Appendix F.4 Preliminary/Bench Test Load 40 Percent	116
Appendix F.5 Preliminary/Bench Test Load 50 Percent	118
Appendix F.6 Preliminary/Bench Test Load 60 Percent	120
Appendix F.7 Preliminary/Bench Test Load 70 Percent	122
Appendix F.8 Preliminary/Bench Test Load 80 Percent	124
Appendix F.9 Preliminary/Bench Test Load 90 Percent	126
Appendix F.10 Preliminary/Bench Test Load 100 Percent	128
Appendix F.11 Preliminary/Bench Test No Load	130
Appendix G Calculations of Test Objects	132
Appendix G.1 General Calculations for all Test Objects	132
Appendix G.2 Theoretical Cube Calculations	132
Appendix G.3 Theoretical Sphere Calculations.....	134
Appendix G.4 Theoretical Cylinder Calculations.....	136
Appendix G.5 Theoretical Rectangle Calculations.....	138
References.....	140

List of Figures

Figure 1.1: Payloads Launched by Country	18
Figure 2.1: Fundamental Forces on an Airplane	26
Figure 2.2: Effect of Drag Form when Streamlining Design	28
Figure 2.3: Hypersonic Shock Layer	32
Figure 2.4: Entropy Layer	33
Figure 2.5: Re-entry Corridor	35
Figure 2.6: Vehicle Re-entry Velocity Profile	35
Figure 3.1: Schematic of TUSQ facility with main components	44
Figure 3.2: Sphere Test Object	49
Figure 3.3: Cube Test Object	49
Figure 3.4: Cylinder Test Object	50
Figure 3.5: Rectangle Test Object	50
Figure 4.1: Image of the Release Mechanism	56
Figure 4.2: Frame 1 of Test Object at One-Hundred Percent	57
Figure 4.3: Frame 60 of Test Object at One-Hundred Percent	57
Figure 4.4: Frame 120 of Test Object at One-Hundred Percent	57
Figure 4.5: Frame 150 of Test Object at One-Hundred Percent	58
Figure 4.6: Frame 1 with No Load at One-Hundred Percent	58
Figure 4.7: Frame 120 with No Load at One-Hundred Percent	58
Figure 4.8: Frame 240 with No Load at One-Hundred Percent	59
Figure 4.9: Test Object's Approximated and Calculated RPM with No Load	60
Figure 4.10: Test Object's Approximated and Calculated RPM with 88.7g Load	61
Figure 4.11: Apparatus Assembly on Release Platform	63
Figure 4.12: Speed Controller	63
Figure 4.13: Power Supply Unit	64
Figure 4.14: Frame 1 of Final Test at Forty Percent	65
Figure 4.15: Frame 100 of Final Test at Forty Percent	65
Figure 4.16: Frame 200 of Final Test at Forty Percent	65
Figure 4.17: Frame 300 of Final Test at Forty Percent	66
Figure 4.18: Frame 400 of Final Test at Forty Percent	66
Figure 4.19: Frame 500 of Final Test at Forty Percent	66
Figure 4.20: Frame 600 of Final Test at Forty Percent	67
Figure 4.21: Frame 625 of Final Test at Forty Percent	67

Figure 4.22: Frame 700 of Final Test at Forty Percent.....	67
Figure 4.23: Frame 800 of Final Test at Forty Percent.....	68
Figure 4.24: Frame 850 of Final Test at Forty Percent.....	68
Figure 4.25: Experiment Pressure Results.....	69
Figure 4.26: Calibration of the Video.....	70
Figure 4.27: X and Y Co-ordinate of the Test Object in Relation to time at the centre of the object... Figure 4.28: X and Y Co-ordinate of the Test Object in Relation to time at the top left edge of the Object.....	70
Figure 4.29: X and Y Co-ordinate of the Test Object in Relation to Frame Number at the centre of the Object.....	71
Figure 4.30: X and Y Co-ordinate of the Test Object in Relation to Frame Number at the top left edge of the Object.....	72
Figure 4.31: Test Object Trajectory at the Centre of the Object.....	72
Figure 4.32: Test Object Trajectory at the top left edge of the Object.....	73
Figure 4.33: Start of Linear Trajectory Path of the Final Test for Drag Coefficient	74
Figure 4.34: End of Linear Trajectory Path of the Final Test for Drag Coefficient	75
Figure B.1: Design Concept One	90
Figure B.2: Design Concept Two	91
Figure C.1: Project Plan Outline.....	93
Figure D.1: Schematic of Test Object Platform.....	97
Figure D.2: Schematic of Motor Housing Unit.....	98
Figure D.3: Schematic of Motor Stabilising Plate	99
Figure E.1: Schematic of Test Object ‘Cube’	100
Figure E.2: Schematic of Test Object ‘Rectangle’.....	101
Figure E.3: Schematic of Test Object ‘Cylinder’	102
Figure E.4: Schematic of Test Object ‘Sphere’	103
Figure F.1: Experiment Setup Side View	104
Figure F.2: Experiment Setup Rear View	104
Figure F.3: Experiment Setup Side Close-Up View	105
Figure F.4: Final Test Images/Snapshots.....	111
Figure F.5: 20 Percent Load Preliminary/Bench Test Images/Snapshots.....	113
Figure F.6: 30 Percent Load Preliminary/Bench Test Images/Snapshots.....	115
Figure F.7: 40 Percent Load Preliminary/Bench Test Images/Snapshots.....	117
Figure F.8: 50 Percent Load Preliminary/Bench Test Images/Snapshots.....	119
Figure F.9: 60 Percent Load Preliminary/Bench Test Images/Snapshots.....	121
Figure F.10: 70 Percent Load Preliminary/Bench Test Images/Snapshots.....	123

Figure F.11: 80 Percent Load Preliminary/Bench Test Images/Snapshots.....	125
Figure F.12: 90 Percent Load Preliminary/Bench Test Images/Snapshots.....	127
Figure F.13: 100 Percent Load Preliminary/Bench Test Images/Snapshots.....	129
Figure F.14: No Load Preliminary/Bench Test Images/Snapshots.....	131

List of Tables

Table 3.1: TUSQ Facility Components.....	44
Table 3.2: TUSQ Facility Standard Operating Conditions	45
Table 3.3: Design Option Decision Matrix.....	47
Table 3.4: Design Limitations and Equipment Requirements.	48
Table 3.5: Assume Property Values for Each Test Object.....	52
Table 3.6: Dimension Limitations for the Test Objects.....	53
Table 3.7: Summary of Theoretical calculations for all of the test objects.....	53
Table 3.8: Object's Revolution Per Second.	53
Table 4.1: Test Object's Approximated and Calculated RPM with No Load.....	59
Table 4.2: Test Object's Approximated and Calculated RPM with 88.7g Load.	61
Table 4.3: Velocity Profiles and Traveling Distance from the edge of the cube to the next edge with respect to its Top Left Corner.	79
Table 4.4: Velocity Profiles and Traveling Distance from one side of the cube to the next side with respect to its Top Left Corner.	80
Table 4.5: Velocity Profiles and Traveling Distance from the edge of the cube to the side with respect to its centre.	80
Table 4.6: Velocity Profiles and Traveling Distance from the side of the cube to the edge with respect to its centre.	80
Table C.1: Breakdown of Project Plan.....	92
Table C.2: Preliminary Outline of Project's Design Stages.....	94
Table C.3: Resources required for the project.	94
Table C.4: Risk Assessment of this Project and Future Projects	96

Nomenclature

The following abbreviations have been utilised throughout this document

USSR	Union of Soviet Socialist Republics
USA	United States of America
ESA	European Space Agency
NASA	National Aeronautics and Administration
LEO	Low Earth Orbit
GEO	Geostationary Orbit
CV	Control Volume
SCARAB	Spacecraft Atmospheric Re-entry and Aero thermal Break-up
TUSQ	
ORSAT	Object Re-entry Survival Analysis Tool
SAPAR	Survivability Analysis Program for Atmosphere Re-entry
DRAPS	Debris Re-entry and Ablation Prediction System

Table of Mathematical Symbols

The following mathematical symbols have been utilised throughout this document including the bibliography:

F_{drag}	Drag Force (N)
m	Mass (kg)
a	Acceleration/Deceleration (m/s^2)
ρ	Density (kg/m^3)
v	Velocity (m/s)
C_D	Drag Coefficient
A	Cross-sectional Area (m^2)
L	Lift Force (N)
C_L	Lift Coefficient
ρ_o	Stagnation Density (kg/m^3)
k	Specific Heat Ratio
M	Mach Number
T_o	Stagnation Temperature (K)
T	Temperature (K)
P_o	Stagnation Pressure (Pa)
P	Pressure (Pa)
BC	Ballistic Coefficient (kg/m^2)
a_{max}	Maximum Acceleration/Deceleration (m/s^2)
$V_{\text{Re-entry}}$	Velocity Re-entry (m/s)
β	Atmospheric Scale Height (m^{-1})
γ	Object's Flight Path Angle (degree or radians)
Altitude _{a_{max}}	Altitude at Maximum
	Acceleration/Deceleration (m)
ρ_{atm}	Atmospheric Density at Sea Level (kg/m^3)
\dot{q}	Heat Rate (W/m^2)
ρ_{air}	Density of Air (kg/m^3)
r_{nose}	Object's Nose Radius (m)
Altitude _{q_{max}}	Altitude at Maximum Heat Rate (m)
F_f	Frictional Force (N)
μ	Coefficient of Friction

$d_{travelled}$	Distance Travelled (m)
t	Time (s)
u	Initial Velocity (m/s)
r	Radius (m)
S	Side Length (m)
g	Gravity (m/s ²)

Chapter 1 - Introduction

1.1 Preamble

As society continues to advance its knowledge and understandings in the fields of science, technology and engineering within the known universe, humanity will always continue to push the limitations and approaches on how they will obtain their goals. This includes but is not limited to; the design, development and implementation of projects within space, communication, navigation and monitoring of the Earth's atmosphere and environmental conditions.

However, through technological advancements, the following problem has arisen; the monitoring, tracking and deorbiting of old spacecraft and debris from past manned and unmanned projects/missions. If an object enters the atmosphere and begins its freefalling decent, this object poses the risk of possibly damaging structures or injuring the inhabitants on the planet, however, this risk increases if the object performs an uncontrolled re-entry. By designing and testing an apparatus that can simulate and examine the trajectory of an object freefalling within a controlled environment, the results obtained from this project could be used to predict not only the object's trajectory and landing zone in real scenarios, but also help expand our knowledge and understanding about the properties effects from the forces interacting with the object.

1.2 Introduction

In today's society, the space industry/sector is playing an increasingly important role in society. Where this industry is now utilised for communication in modern society; ranging from personal use, to private companies and the world governments. Additionally, this industry has also helped society to monitor the environmental changes that occur and help predict future climate forecasts. Furthermore, it has provided the opportunity for society to conduct research in varying fields of studies, such as technology and science including; physics, astronomy, astrophysics, climatology and more.

The space industry/sector initially traced back to 1957 during a period known as the 'Space Race' or 'Space Age' era (Royal Museums Greenwich 2021). Where humanity witnessed the first successful launch and deployment of the artificial satellite Sputnik 1 by the Union of Soviet Socialist Republics (USSR) on the 4th October 1957 (Royal Museums Greenwich 2021).

This then led to various major milestones, such as the Apollo 11 mission in 1969 (Royal Museums Greenwich 2021). However, since the first successful launch of Sputnik 1 in 1957, there has been a total of approximately 6020 rockets launched into space (excluding failures), deploying approximately 11370 satellites for which there is approximately 6900 are still in space today and where only approximately 4000 are still functioning (European Space Agency 2021). Furthermore, there are approximately 28160 pieces of debris currently orbiting Earth, that has been caused by more than 560 break-ups, explosions, collisions or anomalous events resulting in fragments dispersion (European Space Agency 2021). However, the total number of launches are increasing yearly (as seen in Fig. 1.1), and this increase will result in more spacecraft and pieces of debris to remain in orbit until they are re-moved or they re-enter the Earth's atmosphere.

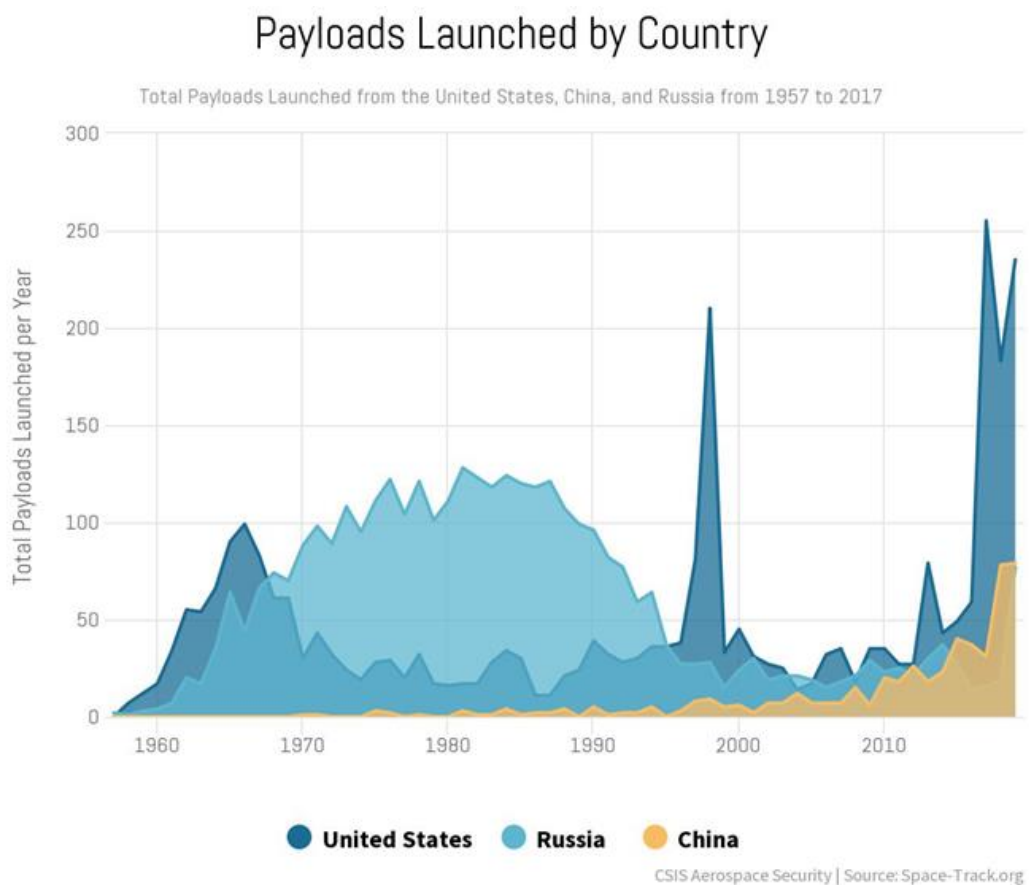


Figure 1.1: Payloads Launched by Country (The Aerospace Security Project 2020).

1.3 The Problem

Since the first successful launch and deployment of a spacecraft (Sputnik 1 by the USSR) in 1957 into Earth's Orbit, humanity's presence of artificial satellites and other man-made equipment/structures in Low Earth Orbit (LEO) through to Geostationary Orbit (GEO) have increased rapidly (Royal Museums Greenwich 2021). However, at the beginning of this technological era, scientists, engineers and governments have not effectively outlined or established the policy and procedures that would be used to terminate or remove these spacecrafts/objects from orbit. Due to the lack of the political policies and standards, these objects have remained in orbit, which in turn has resulted in creating an issue that humanity faces today, the hazard of space travel, deorbiting and tracking these objects (spacecraft or debris) and the risk of injuries from deorbiting these objects. This is evident from the recent event that occurred on the 8th May 2021, where the core 5B booster from the Chinese Long March CZ-5B rocket weighting approximately twenty tonnes, re-entered and performed an uncontrolled re-entry into the Earth's atmosphere (Rourke 2021; Wall 2021). This was due to a design flaw, where the booster could not perform a controlled re-entry into the Earth's atmosphere (Rourke 2021). However, this has not been the first time an object has re-entered the atmosphere in an uncontrolled trajectory, these include the Skylab space station where it landed in outback Australia in July 1979 and the Soviet Union's Salyut 7 space station where it re-entered over Argentina in February 1991 (Wall 2021). Therefore, the problem that this project addresses is the ability to predict and track objects that are freefalling while tumbling from orbit in order to minimise the risk of causing damage to structures or harming the inhabitants on Earth.

In today's society, the job of tracking and the monitoring of space objects/debris in orbit are both not only controlled by government organisations or institutions but also private companies or start-ups. These include; the National Aeronautics and Administration (NASA), the European Space Agency (ESA), Obruta Space Solutions, OrbitGuardians, Share My Space, Clearspace today and Astroscale. However, these organisations and private companies still require public funding through grants and other means of support.

1.4 Research Objective

This project's main aim is to design an apparatus and artificially simulate and examine the re-entry trajectory of an object tumbling at high speed during freefall from orbit within a hypersonic wind tunnel. The main objectives that are required to achieve the primary aim of this project are as follows;

1. Review previous academic research and background information on objects re-entering the earth's atmosphere, this includes re-entry and object trajectory calculations and hypersonic fluid flows.
2. Review and examine the design restrictions and limitations of the prototype with the University of Southern Queensland Hypersonic Wind Tunnel (TUSQ) hypersonic wind tunnel test section and the release mechanism.
3. Design and construct a prototype that can perform the experiment with the test objects within the TUSQ hypersonic wind tunnel facility.
4. Perform the experiment and capture/collect all data relating to the project.
5. Consolidate and examine the captured/collected data.
6. Provide recommendations on the design of the experiment and future experiments.

If there is time available:

7. Design and construct an object to create a supersonic shock wave.
8. Perform the experiment with the supersonic shock wave.

The target market for this proposal are government departments, privately owned companies and university research departments that are interested or are funding space travel or orbiting issues such as re-entry. Additionally, this proposal could also be utilised for future scientific and engineering research and design projects.

1.5 Project Methodology

This project will be divided into five main chapters each comprising of multiple subsections:

- Chapter 1 – Introduction
- Chapter 2 – Literature Review
- Chapter 3 – Project Design

- Chapter 4 – Results
- Chapter 5 – Conclusions and Recommendations

Chapter 1 introduces the project proposal and justifies the necessity to explore and research the effect of tumbling while objects are free falling through the Earth's atmosphere.

Chapter 2 contains the Literature Review, which outlines the importance of deorbiting space debris and predicting the object's trajectory. Additionally, this section will examine and compare previous research that has been conducted in the past and the theoretical calculations related to fluid mechanics and hypersonic flow.

Chapter 3 explores and outlines the TUSQ facility, the design requirements and limitations based on theoretical calculations for the test objects and the motor housing unit gathered from the TUSQ facility. Furthermore, this section will also outline the testing options available and methodology of the testing procedure.

Chapter 4 aims to establish and outline the results that have been collected from the preliminary/bench tests and the final test within the TUSQ facility.

Chapter 5 will outline and summarises the relevant information and the results from the previous four chapters. Furthermore, this chapter will also outline and discuss any recommendation that can be implemented to this current research project and to any future research projects or proposals relevant to or extensions to this research project.

1.6 Consequential Effects

The problem associated with this proposal is the ability to accurately track and predict the trajectory of an object that is tumbling and freefalling through the Earth's atmosphere. If this project is successful, it could have the potential positive effect on the space industry in regards to monitoring and tracking objects re-entering Earth's atmosphere. These benefits include but are not limited to:

- The ability to establish a procedure and the technology that could be used to successfully deorbit the objects and track complex trajectories,
- The ability to track and predict the trajectories of unplanned/unexpected freefalling tumbling objects,

- Decrease the risk of damage to structures and injures to the animals, environment and to human life on Earth,
- Promote future research and innovation within the engineering, technology and science fields,
- Provide future investment opportunities for research and innovation in a variety of fields, and
- Contribute to the overall success of private companies and government organisations and institutions.

However, even with the benefits outlined above, there will always be limitations/repercussions that can cause a negative impact on society from this project. These include but are not limited to the following:

- The accuracy of the data for it to have the ability for it to suit every possible scenario,
- Political and social implication for utilising the information,
- Companies' interaction between one another due to co operations requirements for implementing the project's outcome,
- Environmental effects from the development and testing of the design, and
- The feasibility of implementing the project's outcome.

After comparing both the positive and negative financial, ethical, political and environmental effects from the outcome of this project. It is clear that the project's outcomes benefits will have more of an impact than the negative effects.

1.7 Summary

In conclusion, the introduction briefly examines the past and present contributions and the effect that the space industry has had on society today. Additionally, the introduction also identifies and outlines the problem that society faces today due to the accumulation of spacecraft and debris formed by previous manned and unmanned mission in space. Furthermore, the reasoning for conducting this research project, the overall objectives that will be achieved, the project's structure and the advantages and disadvantages that this research project will have on society and on the targeted market have been outlined and presented within this section.

Chapter 2 - Literature Review

2.1 Introduction

Within this chapter, the literature review will aim to establish the necessity for designing and simulating the effect of a tumbling freefalling object that has entered the Earth's atmosphere. This chapter begins by first exploring the space industry, by investigating the industry's contributions to society and the economy. The chapter then continues by establishing basic knowledge and theoretical calculations of vehicle flight and re-entry within the Earth's atmosphere, fluid mechanics; this includes; the types of fluid flow and the Mach cone propagation, the isentropic stagnation properties of fluid flow and supersonic and hypersonic flow. The chapter then concludes with an examination of previous academic literature performed by accredited professionals, on varying topics that are all related to objects/vehicles re-entering the Earth's atmosphere and an analysis of the knowledge gap within this field of research for this specific topic.

2.2 Space Industry

As society enters into the twenty-first century, the global market has seen some changes in the contribution in some economic sector, one of these sectors in particular is the space industry/economy. As defined by the Better Policies for Better Lives (2020), the space economy is comprised of the full range of activities and the resources that create and provides value and benefits to society in the course of exploring, understanding, managing and utilising space.

In addition, the space economy is not only comprised of the space manufacturing but also the increasingly universal impacts of space-derived products, services and knowledge on economies and societies (Organisation for Economic and Co-operation and Development 2020). These are divided into three main categories, which are; the upstream sector, this includes the research and development, manufacturing and launch (Organisation for Economic and Co-operation and Development 2020). The downstream sector, this includes the space infrastructure operations and 'down-to-earth' products and any services that rely on satellite data and signals (Organisation for Economic and Co-operation and Development 2020). The third category is any activities that are derived from space-derived

activities, such as the technology transferred from the space sector to other industries/sectors (Organisation for Economic and Co-operation and Development 2020).

In 2016, a report from Bryce Space and Technology (2019) estimated that the total global space industry is worth \$345 billion US, where three quarters of the total revenue is contributed by the commercial sector and only one quarter is contributed by government budgets, with the United States of America (USA) contributing approximately \$48 billion US spread across eleven agencies and offices. However, in 2020 the Organisation for Economic and Co-operation and Development (2020) reported that the global commercial revenues from the space sector was estimated to be worth approximately \$280-\$300 billion alone (Organisation for Economic and Co-operation and Development 2020). With the majority of the revenue coming from commercial satellite services such as telecommunication signals and the consumer electronic companies with an approximation of \$126-130 billion US and \$125-130 billion US, respectively (Organisation for Economic and Co-operation and Development 2020).

In today's market, there are five trends that stand out, these include; the technological advancements which provides a more cost-effective method for space activities (Bryce Space and Technology 2019). The increase in private investment from investors (Bryce Space and Technology 2019). A global economy becoming increasingly data dependent with effects on space capabilities and markets (Bryce Space and Technology 2019). The increasing shared vision of space, and finally, the military/strategic developments around space (Bryce Space and Technology 2019).

Furthermore, since the decommissioning of NASA's space shuttles, the privatisation of the space industry has grown dramatically due to the government contracts awarded to these private companies (Duffy 2021). These include; the recent contracts, where a 2021 \$2.9 billion US contract awarded to SpaceX to transport NASA's astronauts to the moon, the two 2021 US military contracts awarded to SpaceX totalling \$159 million US and the two US Department of Defence contracts totalling \$224.4 million US awarded to United Launch Alliance (Duffy 2021). Therefore, with this ever-growing market within the today's society the necessity and urgency of monitoring and tracking debris in space will become a priority for society.

2.2.1 Market

Due to the first successful launch of a satellite, Sputnik 1 in 1957 and the ground breaking innovations made in the fields of science, engineering and technology since 1957, the space industry has begun to

play an important role in society (Royal Museums Greenwich 2021). From military to civilian applications where some companies such as SpaceX and Boeing are becoming increasingly invested in and will continue to be invested in the near future. This has been due to the successful launch of SpaceX's Falcon 9 reusable rocket which has decreased the cost of launching one kilogram of equipment in space from approximately \$18 500 US to approximately \$ 2 720 US (Cobb 2019). However, due to the success, there has also been an increase in the number of objects launched into space every year, where by 2028 there could be approximately 990 satellites launched each year (Wood 2020).

Due to the increase in space related objects in orbit and the ever-expanding growth of society, by increasing the number of objects orbiting will result in the increasingly likelihood of an object entering the atmosphere and causing damage to structures, animals, environment or to human life on this planet. Furthermore, since the first launch of a satellite there has been numerous times where objects had re-entered the atmosphere and landed on the Earth's surface, these include; in 1979 some parts of NASA's skylab structure landed in the India Ocean and in some parts of south-western Australia (Whitley 2020). Then in 2011, NASA reported and estimated that twenty-six pieces of debris weighing approximately 544kg that were from the Upper Atmosphere Research Satellite (UARS), would land in the southern hemisphere over an estimated 800km squared landing zone (Potter 2011: O'Carroll 2011). Then in 2020 an eighteen tonne Chinese rocket passed over Los Angeles and New York before landing in the Atlantic Ocean (Wassermann 2020).

2.3 Drag and lift forces

When examining an object or vehicle in flight there are fundamentally four forces that will act upon that object/vehicle while it is in motion through the atmosphere (Federal Aviation Administration 2016). These forces are referred to as the aerodynamic forces and these are; drag, lift, thrust and gravitational due to the mass of the object/vehicle (as seen in Fig. 2.1) (Federal Aviation Administration 2016).

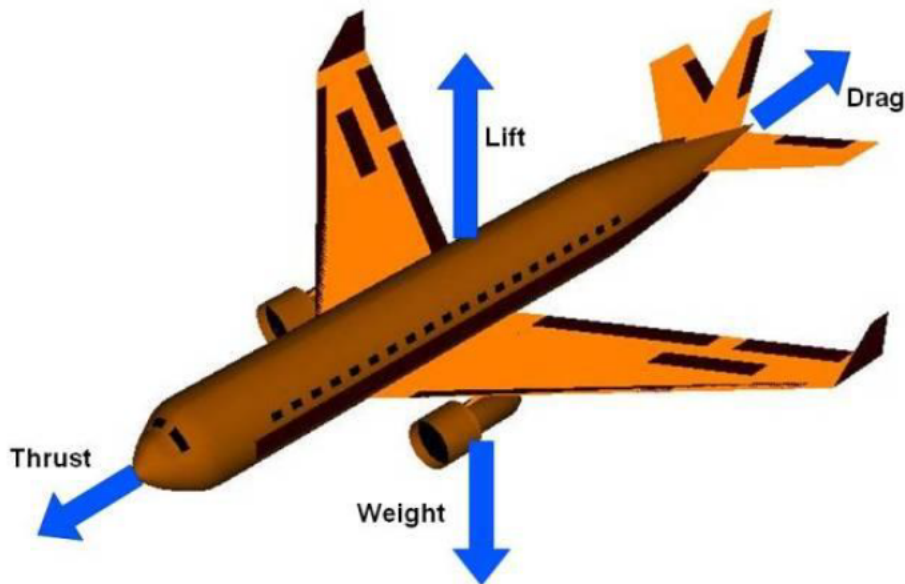
- The drag force is the resistance force that an object or vehicle experiences while the object/vehicle is in flight as it moves through a fluid (Federal Aviation Administration 2016). This force acts in the opposite direction of the thrust of the object/vehicle (as seen in Fig. 2.1) (Federal Aviation Administration 2016).

- Lift force is the force that is the product of the dynamic effect of the fluid acting on the object/vehicle (Federal Aviation Administration 2016). This force acts perpendicular to the object's/vehicle's flight path. Furthermore, this force opposes the force produced by the gravitational force acting on the mass of the object/vehicle (as seen in Fig 2.1) (Federal Aviation Administration 2016).
- Thrust is the force that is produced by the vehicle, and opposes the drag force produced by the flow (as seen in Fig. 2.1) (Federal Aviation Administration 2016). In order to sustain flight, the vehicle needs to produce enough thrust to overcome the drag force imposed on the vehicle (Federal Aviation Administration 2016).
- Gravitational force is the force that is imposed by gravity acting on the total mass of the object/vehicle (Federal Aviation Administration 2016). The gravitational force imposed on the object/vehicle opposes the lift forces produced from the object/vehicle (as seen in Fig. 2.1) (Federal Aviation Administration 2016).

National Aeronautics and Space Administration



Four Forces on an Airplane



www.nasa.gov

Figure 2.1: Fundamental Forces on an Airplane (National Aeronautics and Space Administration 2021).

2.3.1 Drag Force

As stated previously, drag is the force that resists a vehicle/object's movements through a flow field (Federal Aviation Administration 2016). There are two basic types of drag, these are parasite and induced drag (Federal Aviation Administration 2016). Parasitic drag is comprised of all of the forces that work to hinder and decrease the vehicle/object's velocity and does not contribute to the production of lift (Federal Aviation Administration 2016). These forces include; the turbulence from the airstream, the displacement of the flow by the vehicle and the interference due to the flow moving over the vehicle/object's surface (Federal Aviation Administration 2016). Furthermore, there are three types of parasitic drag, these include form drag, interference drag and skin friction (Federal Aviation Administration 2016).

- Form drag is the drag generated by the vehicle/object's shape and the fluid's flow around the shape (Federal Aviation Administration 2016). The amount of drag contributed by this type of drag is determined by the time required for the fluid's flow field to be reconnected downstream in the fluid's flow field (Federal Aviation Administration 2016). Therefore, the amount of drag contributed by this type of drag can be decreased by modifying the vehicle/object's design (as seen in Fig 2.2) (Federal Aviation Administration 2016).
- Interference drag is the drag generated by the intersection of the fluid's streamlines forming eddies currents, turbulence or restricts laminar flow (Federal Aviation Administration 2016).
- Skin friction drag is the vehicle/object's aerodynamic resistance due to the fluid's flow coming in contact with the surface of the object/vehicle (Federal Aviation Administration 2016). Therefore, as a result of this type of drag, a layer of free-stream molecules are formed between the object's surface and the fluid's laminar flow field, this is referred to as the boundary layer (Federal Aviation Administration 2016).

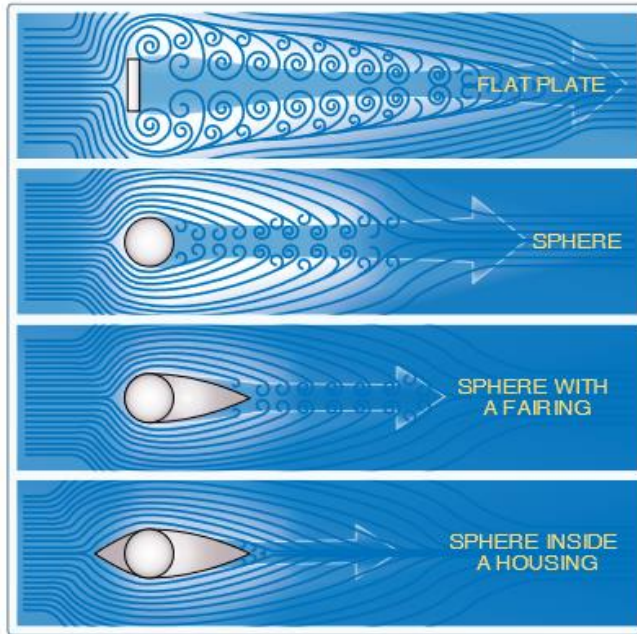


Figure 2.2: Effect of Drag Form when Streamlining Design (Federal Aviation Administration 2016).

Induced drag is the drag that is created by the vortices from the equalisation of the two pressures formed by the vehicle/object (Federal Aviation Administration 2016). Therefore, in fluid mechanics, the total drag force that is experienced on an object can be determined by the following formula;

$$F_{drag} = ma = \frac{1}{2} \rho v^2 C_D A \quad (2.1)$$

Where ' F_{drag} ' is the drag force (N), ' ρ ' is the density of the fluid (kg/m^3), ' V ' is the velocity of the object (m/s), ' C_D ' is the drag coefficient, ' A ' is the cross-sectional (m^2), ' m ' is the mass (kg) of the object and ' a ' is the acceleration (m/s^2) (Federal Aviation Administration 2003; Pritchard & Mitchell 2015). Furthermore, the drag coefficient is the dimensionless quantity that is used to quantify the object's resistance or drag in a fluid's flow (Federal Aviation Administration 2016).

2.3.2 Lift

In order to sustain flight, the gravitational forces imposed on the mass of the object/vehicle must be overcome this is referred to as lift (Federal Aviation Administration 2016). The amount of lift is generated/required to sustain flight and overcome the gravitational force is determined by a variety of factors these include; shape size and velocity of the object/vehicle (Federal Aviation Administration 2016). However, lift is created by the difference in pressure above and below the surface (Federal Aviation Administration 2016). When the pressure is higher on the surface below the object/vehicle than above the object/vehicle, the resultant net force is upwards thus creating the required amount of lift to sustain flight (Federal Aviation Administration 2016). Furthermore, when the opposite occurs, flight cannot be sustained (Federal Aviation Administration 2016). Therefore, in fluid mechanics, the total lift force that is experienced on an object can be determined by the following formula;

$$L = \frac{C_L \times \rho \times v^2 \times A}{2} \quad (2.2)$$

Where ‘ L ’ is the lift force (N), ‘ ρ ’ is the density of the fluid (kg/m^3), (v) is the velocity of the object m/s , ‘ C_L ’ is the lift coefficient, and ‘ A ’ is the cross-sectional (m^2) (Federal Aviation Administration 2003; Pritchard & Mitchell 2015). Additionally, the lift coefficient is the dimensionless quantity that is used to measure the difference in pressure between the object’s above and below surfaces as they moving through the fluid’s flow (Federal Aviation Administration 2016).

2.3.3 Flow Types and the propagation of the Mach Cone

Within the field of fluid mechanics, in particular fluids that exhibit compressible flow, there are four basic types of flow, these are subsonic flow, transonic flow, supersonic flow and hypersonic flow (Pritchard & Mitchell 2015). However, all of these types of flow are determined by the speed of sound (Pritchard & Mitchell 2015). Subsonic flow is when the velocity within the fluid’s field is less than the speed of sound, this is what we experience daily (Pritchard & Mitchell 2015). Supersonic flow is when the velocity within the fluid’s field is greater than the speed of sound, this is experience which supersonic aircraft (Pritchard & Mitchell 2015). Transonic is when the fluid has both subsonic and

supersonic flow within the flow field, this generally occurs between 0.9 to 1.2 the speed of sound and is experienced within the aircraft's compressors and fans (Pritchard & Mitchell 2015). Hypersonic flow is when the velocity within the fluid's field is five times greater than the speed of sound, this is experienced during re-entry and on missiles (Pritchard & Mitchell 2015).

2.3.4 Isentropic Stagnation Properties Flow

Within the field of fluid mechanics, in particular compressible flow, properties such as density, temperature, pressure, entropy, enthalpy, internal energy and velocity (these are denoted as ' ρ ', ' T ', ' P ', ' s ', ' h ', ' u ', and ' v ', respectively) may change as the fluid process through a system (Pritchard & Mitchell 2015). Therefore, a reference condition is required to relate the conditions of the fluid's flow (Pritchard & Mitchell 2015). This can be obtained when the fluid's flow is brought to rest at some point within the system (Pritchard & Mitchell 2015). This point is referred to as the stagnation point, and for the properties stated previously this point is denoted as ' ρ_o ', ' T_o ', ' P_o ', ' s_o ', ' h_o ', ' u_o ', and ' v_o ', respectively (Pritchard & Mitchell 2015). Since the condition of the fluid's flow changes, the process of bringing the fluid to rest in a system and obtaining these properties can be difficult (Pritchard & Mitchell 2015). However, this can be easily obtained in an isentropic process where there is no friction, heat transfer or turbulent flow (Pritchard & Mitchell 2015). However, the properties that would be obtain would only be the local isentropic stagnation properties, this is because each point in the flow can have its own isentropic properties (Pritchard & Mitchell 2015). The density, temperature and pressure properties can be obtained by the following formulas, respectively (Pritchard & Mitchell 2015);

$$\frac{\rho_o}{\rho} = \left[1 + \frac{k-1}{2} M^2 \right]^{\frac{1}{k-1}} \quad (2.3)$$

$$\frac{T_o}{T} = 1 + \frac{k-1}{2} M^2 \quad (2.4)$$

$$\frac{P_o}{P} = \left[1 + \frac{k-1}{2} M^2 \right]^{\frac{k}{k-1}} \quad (2.5)$$

Where, ‘ ρ_0 ’ is the stagnation density (kg/m^3), ‘ T_0 ’ is the stagnation temperature (K), ‘ P_0 ’ is the stagnation pressure (Pa), ‘ ρ ’ is the density of the fluid’s flow (kg/m^3), ‘ T ’ is the temperature of the fluid’s flow (K), ‘ P ’ is the pressure of the fluid’s flow (Pa), ‘M’ is the Mach number, and ‘k’ is the specific heat ratio (Pritchard & Mitchell 2015).

2.3.5 Supersonic/Hypersonic Flow

As an object approaches supersonic, the pressure density and temperature increase to a point where a shock wave is formed and what is referred to as a sonic boom (Anderson 2019). There are two types of shock waves that may form during flight; these are normal and oblique (Anderson 2019). During supersonic and hypersonic speeds, the object experience oblique comprising of varying layers, while an object travelling at transonic speeds will only experience normal shock waves, this is due to the wave formations remaining further apart (Anderson 2019).

Oblique shock waves are the waves that are observed at the leading and tailing edge of an object (Anderson 2019). Oblique shock waves can occur at any given flow direction angle and as the object increases in speed, the density across the shock wave also increases resulting in the shock wave increasing in size (Anderson 2019). However, as the density increases the mass flow behind the shock becomes more easily compressed through a small area, which in turn results in the distance between the body of an object and the shock wave to be small (Anderson 2019). This area or flow field between the body and the shock wave is referred to as the shock layer (as seen in Fig. 2.3) (Anderson 2019). Furthermore, at hypersonic speeds the shock wave angle can actually be very thin and when taking into consideration of the high temperatures experienced during hypersonic flight, the chemical reactions would further decrease the shock wave’s angle (Anderson 2019). However, due to the thin shock layer, there are some physical compilations that can occur at low Reynold’s numbers such as the merging of the shock wave with a thick viscous boundary layer growing from the body’s surface (Anderson 2019).

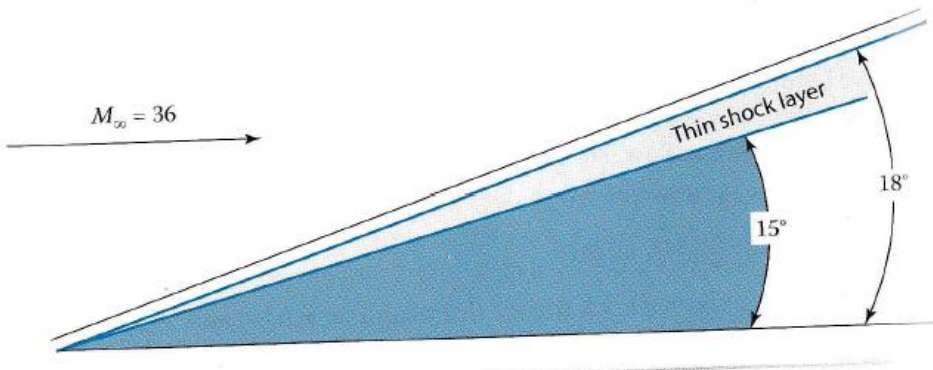


Figure 2.3: Hypersonic Shock Layer (Anderson 2019).

Another layer that is observed during hypersonic speeds for particularly blunt nosed objects due to the highly curved shock wave (as seen in Fig. 2.4) is the entropy layer (Anderson 2019). In hypersonic flow the entropy of the flow increases across the shock wave, and a stronger shock wave, results in a larger entropy increase (Anderson 2019). Therefore, as a streamline passing near the centreline of the flow, the flow will experience larger entropy increases than the surrounding streamlines (Anderson 2019). This is because within the nose region of the object, strong entropy gradients are generated and flows downstream along the object's body, effectively wetting the body (Anderson 2019). Due to these gradients, the boundary layer is also affected due to the strong vorticity interaction from the vorticities created within the entropy layer (Anderson 2019). This is because as the boundary layer along the surface grows in size within the entropy layer (Anderson 2019). This affect causes analytical problems when standard boundary-layer calculations are performed (Anderson 2019).

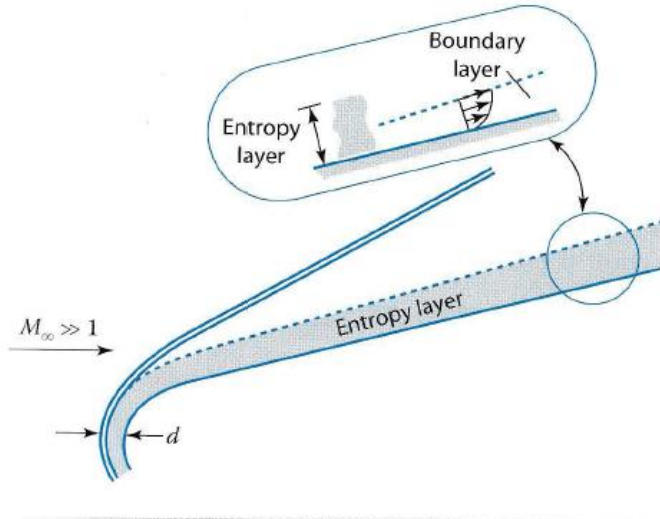


Figure 2.4: Entropy Layer (Anderson 2019).

Another affect that is observed in the boundary layer for a flat plate is the interaction between the kinetic energy and the internal energy of the gas (Anderson 2019). This is referred to as viscous dissipation and is due to the viscous effect, where the kinetic energy is partially transformed into the internal energy of the gas, resulting in a boundary's layer temperature to increase, thus controlling the characteristics of the hypersonic boundary layers such as the thickness of the boundary layer (Anderson 2019). Due to the thickness of the boundary layer, in hypersonic flow, the flow can exert a major displacement effect on the inviscid flow outside the boundary layer caused in the illusion of a larger body shape (Anderson 2019). As the size of the boundary layer increases, the outer inviscid flow changes, thus affecting the growth of the boundary layer (Anderson 2019). This is referred to as the viscous interaction, which effects the surface-pressure distribution thus effecting lift, drag and stability on the hypersonic vehicles/objects and increases the skin friction and heat transfer (Anderson 2019). Furthermore, it is then possible for the boundary layer on the hypersonic vehicle/object to became thick enough where the layer merges with the shock layer resulting in becoming fully viscous (Anderson 2019).

When extreme viscous dissipation occurs, the temperature of the layer can reach very high temperatures, where it is possible to excite the vibrational energy within the molecules and cause dissociation and possibly even ionization within the gas (Anderson 2019). Additionally, if the vehicle or object is coated in an ablative heat shield, the products of the ablation is also present within the boundary layer which in turn produces complex hydrocarbon reactions (Anderson 2019). Where both of these effects results in a chemically reacting boundary layer which can dominate the entire shock

wave (Anderson 2019). When an object or vehicle is accelerated to hypersonic speeds, the reacting gas temperature increases to high levels and the gas behaves nonideally (Anderson 2019). Where the vibrational energy of the molecules becomes excited, the specific heats values to become functions of temperature and as the temperature continues to increase, chemical reactions will occur (Anderson 2019). These phenomena are referred to as high temperature effects and can affect the lift, drag and moment of the vehicle/object (Anderson 2019). However, the most dominant effect of the high temperature is the heat transfer rate to the surface through convection or radiative heating (Anderson 2019).

2.4 Re Entry

Like vehicle launching, vehicle re-entry is a complicated process with hazardous risks involved, which requires the balancing of three main requirements (Federal Aviation Administration 2003). These are; deceleration; if the vehicle does not decelerate enough the vehicle could hit the atmosphere and be redirected back into space (Federal Aviation Administration 2003). Heating; as the vehicle re-enters the atmosphere, the molecules interact with the vehicle causing friction, causing the vehicle to heat up, where the higher the velocity the more friction is created (Federal Aviation Administration 2003). And the accuracy of landing/impact; during re-entry the vehicle is required to land in certain areas, the smaller the area, the higher the re-entry angle (Federal Aviation Administration 2003). Therefore, a vehicle must re-enter in a region that is referred to as the re-entry corridor (as shown in Fig. 2.5) (Federal Aviation Administration 2003). If the vehicle undershoots, the vehicle will have an increase in deceleration, where it will experience more drag, thus resulting in more friction (Federal Aviation Administration 2003). If the vehicle over shoots the vehicle will experience less drag and could bounce off the atmosphere and back into space (Federal Aviation Administration 2003). If the vehicle does enter the upper atmosphere through the re-entry corridor, the vehicle's velocity at the beginning stays constant, however, as the vehicle starts to descend further into the atmosphere, the velocity begins to rapidly decrease to a point until the vehicle is about to touchdown (as shown in Fig. 2.6) (Federal Aviation Administration 2003).

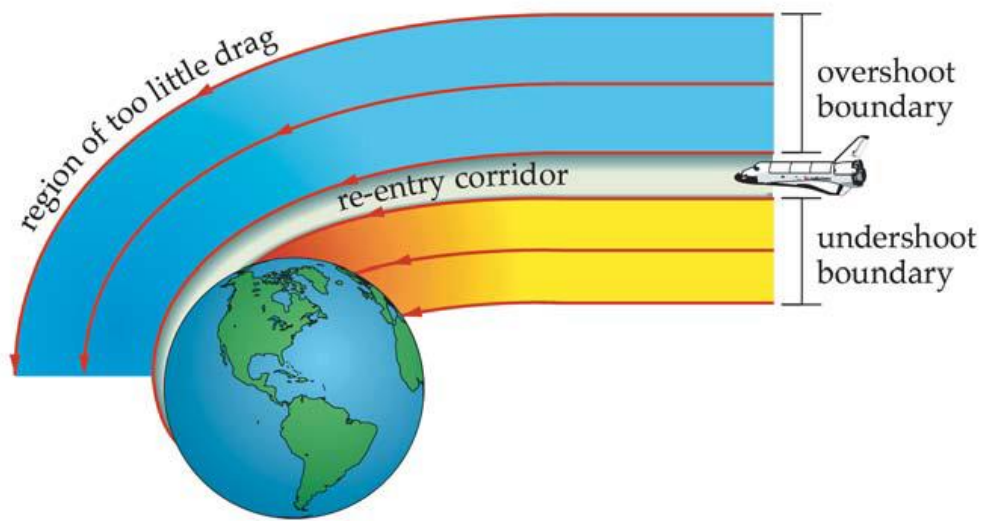


Figure 2.5: Re-entry Corridor (Federal Aviation Administration 2003).

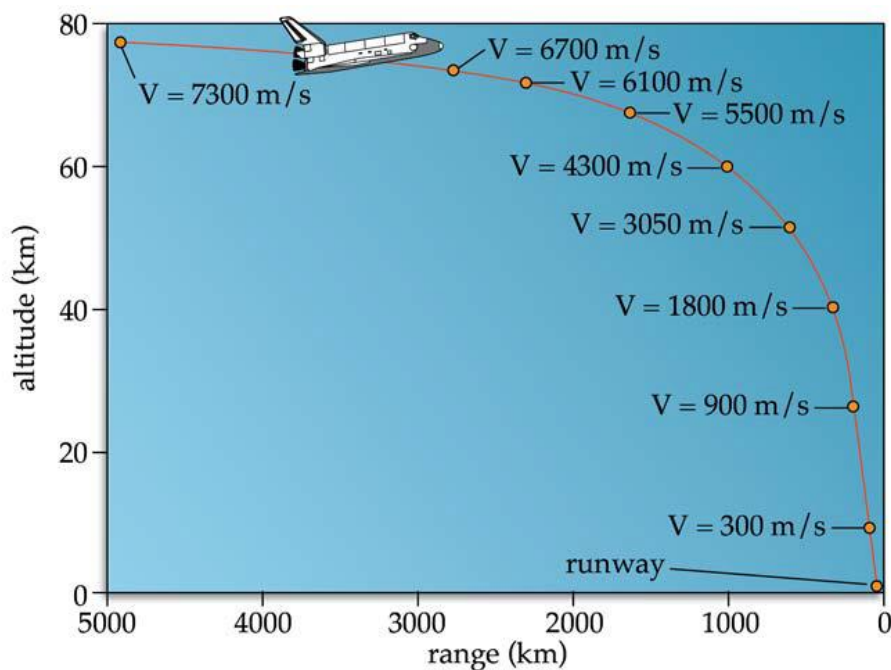


Figure 2.6: Vehicle Re-entry Velocity Profile (Federal Aviation Administration 2003).

2.4.1 Re-entry Calculations

During re-entry, a vehicle experiences three different forces; drag; this is the resistant force applied to a moving object (Federal Aviation Administration 2003). Lift; this is the force applied to an object as it passes over the object's surface (Federal Aviation Administration 2003). Gravitational; this is the force that attracts two objects together (Federal Aviation Administration 2003). In order to calculate a vehicle's re-entry characteristics, it is important to understand how to calculate the drag force that is experienced on an object, this can be calculated by Eq. 2.1 (Federal Aviation Administration 2003). However, Eq. 2.1 can be modified to in terms of acceleration, where (Federal Aviation Administration 2003);

$$a = \frac{1}{2} \rho V^2 \frac{C_D A}{m} \quad (2.6)$$

This then leads to the formation of the ballistic coefficient, which is the object's total amount of deceleration that an object experiences during flight, where (Federal Aviation Administration 2003);

$$BC = \frac{m}{C_D A} \quad (2.7)$$

Where, 'BC' is the ballistic coefficient (kg/m^2) (Federal Aviation Administration 2003). As the drag coefficient and the area increases, there is a decrease in the ballistic coefficient, resulting in an increase of the object's rate of deceleration (Federal Aviation Administration 2003). Therefore, blunt objects decelerate at a higher rate than streamlined objects.

As stated, previously while an object re-enters the atmosphere, the object starts to decelerate at a steady rate (Federal Aviation Administration 2003). However, at a certain point this then changes where the object's rate of acceleration increases rapidly to a maximum point (Federal Aviation Administration 2003). Once this point is reached the object's rate of deceleration then starts to decrease (Federal Aviation Administration 2003). The point for which the object maximum deceleration and altitude reaches can be calculated by the following formulas (Federal Aviation Administration 2003);

$$a_{max} = \frac{V_{re-entry}^2 \beta \sin \gamma}{2e} \quad (2.8)$$

$$Altitude_{a_{max}} = \frac{1}{\beta} \ln \left(\frac{\rho_{atm}}{BC \beta \sin \gamma} \right) \quad (2.9)$$

Where, ' a_{max} ' is the object's maximum deceleration (m/s^2), ' $V_{re-entry}$ ' is the vehicle's velocity at re-entry (m/s), ' β ' is the atmospheric scale height (0.000139 m^{-1}), ' γ ' is the object's flight path angle (deg or rad), ' e ' is the base of the natural logarithm, ' $Altitude_{a_{max}}$ ' is the maximum altitude (m) at maximum deceleration, and ' ρ_{atm} ' is the atmospheric density at sea level (Federal Aviation Administration 2003).

Furthermore, as stated earlier, an object re-enters the atmosphere, the object experiences friction when in turn generates heat, due to the energy being transferred from the molecules within the Earth's atmosphere to the object's material (Federal Aviation Administration 2003). This transference of energy can occur in three ways, these are; through radiation, conduction and convection (Federal Aviation Administration 2003). So, the rate of heat transferred can be approximated by the following formula (Federal Aviation Administration 2003);

$$\dot{q} = 1.83 \times 10^{-4} v^3 \sqrt{\frac{\rho_{air}}{r_{nose}}} \quad (2.10)$$

Where, ' \dot{q} ' is the heat rate of the object (W/m^2), ' v ' is the velocity of the object (m/s), ' ρ ' is the air density (kg/m^3), and ' r_{nose} ' is the object's nose radius (m) (Federal Aviation Administration 2003). In addition, the altitude for which the rate of heat transferred occur can be calculated by the following formula (Federal Aviation Administration 2003);

$$Altitude_{\dot{q}_{max}} = \frac{1}{\beta} \ln \left(\frac{\rho_{atm}}{3BC \beta \sin \gamma} \right) \quad (2.11)$$

Where, ' $Altitude_{\dot{q}_{max}}$ ' is the maximum altitude (m) at maximum heat rate of the object (Federal Aviation Administration 2003).

2.5 Academic Literature

While investigating and examining the majority of the academic literatures that were found, making reference to object tracking/monitoring during freefall were based around a variety of topics. These topics include; re-entry survival analysis, trajectory analysis and control, separation process during hypersonic flow, determining the risk analysis of spacecraft re-entry, the aerothermodynamics of spacecraft and spacecraft optimisation for re-entry.

The study ‘Dynamics of spherical space debris of different sizes falling to Earth’, presented by Sliz-Balogh et al. (2020) examines the re-entry and trajectory of spherical iron particles at different heights above the Earth’s surface for a variety of scenarios. The authors first started by examining the trajectories of a one-centimetre spherical iron particle that was launched at 1000km above the Earth’s surface with varying initial velocities and angles to determine the time required for the spheres to fall to the Earth’s surface (Sliz-Balogh et al 2020). The authors then widen the scenario by examining the trajectories of the spheres at different sizes (from 0.01mm to 10m) launched with varying angles, velocities and heights above the Earth’s surface after an elapsed time (90° at 100km with an initial velocity of 8.47km/s, at 150km with an initial velocity of 7.817km/s, at 50km with an initial velocity of 7.877km/s, 122.6° at 10 000km with an initial velocity of 4.57km/s and 45° at 100km with an initial velocity of 5.65km/s) (Sliz-Balogh et al 2020). Sliz-Balogh et al (2020) then examine the impact time, velocity and angle of the spherical particles with varying radius (from 0.01mm to 10m) and at varying heights (10km to 150km). Additionally, the authors simulate the trajectories of an explosion event at a height of 1000km above the Earth’s surface of 330 spherical particles with varying angles and radii (Sliz-Balogh et al 2020). The authors concluded by outlining varying ideas to decrease the amount of space debris in orbit (Sliz-Balogh et al 2020).

The study ‘Analytical and numerical re-entry analysis of simple shaped objects’, by Fritzsche, Lips and Koppenwallner (2007), examines three different methods to calculate the demise or survival of objects re-entering the Earth’s atmosphere, these were; analytical, numerical and the SCARAB. For the analytical method, the authors examined the radiative and calorimetric failure/demise criteria (Fritzsche, Lips & Koppenwallner 2007). The radiative criteria examines if the object reaches the maximum radiative equilibrium wall temperature, if the object does not reach the material’s melting point, the object will survive, if the material does reach the material’s melting point the object will not survive (Fritzsche, Lips & Koppenwallner 2007). The calorimetric criteria examine the heat storage capacity of the object (Fritzsche, Lips & Koppenwallner 2007). The numerical method utilises the predetermined parameters to determine the survivability of the object for each type of combination of the following parameters; the shape of the object (a sphere, box and cylinder were tested), geometric parameters including diameter, length and wall thickness, material composition (aluminium AA7075,

stainless steel A316, titanium, CFRP and zerodur, and the initial orbital parameters (altitude, velocity and flight path) (Fritsche, Lips & Koppenwallner 2007). The final method SCARAB analyses the shielding effect, that is present in real scenarios such as satellites, where the internal components are shielded by the shell (Fritsche, Lips & Koppenwallner 2007). This method analyses a variety of simple spheres, double spheres and triple spheres comprising of different combinations to determine the survivability of the object (Fritsche, Lips & Koppenwallner 2007). The authors found that all of the combinations would fail other than the triple sphere combination, which would allow the inner sphere to survive (Fritsche, Lips & Koppenwallner 2007). The authors concluded that all results from the three-methods agreed with one another (Fritsche, Lips & Koppenwallner 2007).

The study, ‘Estimation of debris dispersion due to a space vehicle breakup during re-entry’, by Reyhanoglu and Alvarado (2013), utilises the covariance propagation method and Monte Carlo method to estimate the debris dispersion area due to vehicle breakup at high altitudes (Reyhanoglu & Alvarado 2013). The authors found that the covariance method is much more computationally efficient when compared to the Monte Carlo method (Reyhanoglu & Alvarado 2013). This is because the Monte Carlo method requires the generation of 1024 sample trajectories to be integrated of 6144 first order differential equations (Reyhanoglu & Alvarado 2013). While the covariance propagation method requires the integration of six first order differential equations to obtain the six states of nominal trajectory and the integration of twenty-one first-order differential equations, totalling twenty-seven equations (Reyhanoglu & Alvarado 2013). The authors also identify that the covariance propagation method should be used in identifying the hazardous altitude layers at varying times when considering the high density and wind models for various ballistic coefficients (Reyhanoglu & Alvarado 2013). Additionally, this data could also be utilised during the risk management stage of the re-entry (Reyhanoglu & Alvarado 2013). The authors conclude by outlining the future research avenues, these include; analysing multiple simulations with various ballistic coefficients in regards to the debris dispersion, analysing the effect of random acceleration vectors and lift forces, and analysing the models when considering the physical properties of the debris such as the type of material and temperature (Reyhanoglu & Alvarado 2013).

The study ‘Spacecraft design optimisation for demise and survivability’, by Trisolini, Lewis and Colombo (2018), examines two models that have been developed to determine the demise and survivability of satellites in particular the tanks (Trisolini, Lewis & Colombo 2018). The authors decision to select the tanks for this case study was because they are sensitive to both design requirements and are both important to the missions’ goals and the demise process (Trisolini, Lewis & Colombo 2018). Additionally, the authors also establishes that the demise and survivability of the satellites are determined by the material selection, the geometry and the position within the spacecraft (Trisolini, Lewis & Colombo 2018). The authors tested and analysed cylindrical and spherical tanks with varying thickness, composition and number of vessels and the results revealed that only

particular solutions could satisfy the casualty risk of fifteen joule threshold (based on NASA's standard of risk due to injuries from impacts) (Trisolini, Lewis & Colombo 2018). Furthermore, the authors concluded that future experiments need to provide further effort to the definition of the survivability and demisability indices via applying constraints to the optimisation of the equipment (Trisolini, Lewis & Colombo 2018).

The study, 'Space Debris Re-entry Analysis Methods and Tools', by Wu and et al (2011), investigates and develops a new object-oriented debris re-entry analysis method; the Debris Re-entry and Ablation Prediction System (DRAPS). The authors first outline the current method; the Monte Carlo that is used for the uncertainty analysis, breakup prediction and parameters which are used to determine the survivability of an object (Wu & et al 2011). This analysis can then be classified into categories; the object-oriented method and the spacecraft-oriented method (Wu & et al 2011). The authors then continue by explaining their new DRAPS method (Wu & et al 2011). Which introduces fifteen new object shapes with fifty-one predefined motions and relevant aerodynamic and aerothermal models (Wu & et al 2011). The authors then conclude by recommending further improvements to these methods and the survivability of debris is largely determined by the size of the object (Wu & et al 2011).

The study, 'Separation process of multi-spheres in hypersonic flow', by Park and Park (2020), examines the separation process of multi-spheres in hypersonic flow that were conducted in a shock tunnel at Mach Six. The authors used a variety of spheres comprised of iron or acetal varying from 2.38 to 6mm, where the trajectory of a single and varying multiple sphere scenarios was analysed by optical images where the lateral velocities and the separation of the bodies were analysed (Park & Park 2020). Additionally, the authors also developed a new equation based on the Passey and Melosh's theory of two bodies (Park & Park 2020). When comparing the theoretical and experimental results they found both results were in agreement (Park & Park 2020). However, when the separation of the multiple spheres was compared to the single and two spheres, the results revealed that as the number of spheres increase there was an increased in the lateral velocities but however there was a decrease in the ballistic coefficient (Park & Park 2020). This result led to discrepancies in the ground footprint and downrange when compared to the single sphere (Park & Park 2020).

The study, 'Re-entry survival analysis of tumbling metallic hollow cylinder', by Sim and Kim (2011), examines the survivability of a tumbling metallic hollow cylinder. The authors begin by reviewing NASA's Object Re-entry Survival Analysis Tool (ORSAT) and the new equation used to determine the reradiation heat loss of hollow cylindrical objects (Sim & Kim 2011). The author then used the Survivability Analysis Program for Atmosphere Re-entry (SAPAR) code to validated this equation (Sim & Kim 2011). The authors then used this equation, the ORSAT model and a comparative case performed on the Delta-II stage cylindrical tanks to determine the reradiation heat loss, surface

temperature, emissivity and oxidisation coefficient of the hollow cylinder during re-entry (Sim & Kim 2011). The results revealed that the new equation agreed with the case study when a practical valve for thermal emissivity was used in the analysis (Sim & Kim 2011). However, when compared to the ORSAT, the results from the new equation for the reradiation heat flux revealed that there was an increase in the reradiation heat loss and a decrease in the surface temperature of the hollow cylinder (Sim & Kim 2011). The authors do consider that this partial discrepancy could be due to the ORSAT analysis and the research on the Delta-II second stage cylindrical tank, however, the effects could be negligible in certain scenarios (Sim & Kim 2011). Furthermore, the results revealed that the emissivity of the material had significant influence on the peak temperature while the oxidation coefficient did not (Sim & Kim 2011).

The study, ‘Uncontrolled re-entries of spacecraft and rocket bodies: A statistical overview over the last decade’, by Pardini and Anselmo (2019), examines and explores the past re-entry events from 2008 to 2017. The authors begin by providing statistical background information on the history of and the number of payloads, rocket bodies and orbital debris that have re-entered the Earth’s atmosphere since the beginning of the space age (Pardini & Anselmo 2019). The authors then outline the most relevant and historic uncontrolled re-entries (Pardini & Anselmo 2019). The authors then proceed to catalogue, characterises and determine the cumulative mass of each of these categories of all of the uncontrolled re-entries from 2008 to 2017 by weight and type of object, such as intact objects, spacecraft and upper stages (Pardini & Anselmo 2019). Furthermore, the authors then further categorise these re-entry events into *‘relevance, re-entry frequency, returned mass, distribution in inclination, overflown latitude bands, eccentricity and perigee/apogee altitudes before re-entry’* (Pardini & Anselmo 2019). The author’s main results revealed the following; that over the ten-year period there were 448 large intact objects that have re-entered the atmosphere in an uncontrolled trajectory, the average returned mass per year was approximately 90 metric tons, where object’s heavier than 500kg re-entered every nine days, while an objects with a mass greater than 5000kg re-entered every 215 days (Pardini & Anselmo 2019). The authors then concluded with their final conclusions about the increasing risk of future uncontrolled re-entries (Pardini & Anselmo 2019).

2.5.1 Literature Knowledge and Gap

After examining and understanding the variety of research conducted in the previous section, there are a couple of knowledge gaps that were identified and present within the academic research. One of these knowledge gaps that were identified was in relation to the method on obtaining the data, where

the data collected was obtained from numerical and computational simulation only. Another gap that was present within the academic research was in relation to the characteristics of the re-entry of the object, where only one of the researches conducted took into consideration the effect of a tumbling object during freefall/re-entry. After examining the academic research in the previous section, there has been a lot of research in regards to the re-entry and the predicting re-entry trajectory of freefalling objects. However, more research is still required to perfect the data and implement a system that accurately determines an object's trajectory within the atmosphere.

2.6 Summary

In summary, this chapter establishes the necessity for designing and simulating the effects that a tumbling freefalling object experiences during re-entry within the Earth's atmosphere to predict the object's trajectory. This chapter also explored and examined the current contributions that the space industry provides to society and the global economy. In addition, this chapter explored and established the basic knowledge and theoretical calculations for vehicle re-entry within the Earth's atmosphere, basic fluid mechanics; this includes the types of fluid flow and the Mach cone propagation, the isentropic stagnation properties of fluid flow and supersonic and hypersonic flow. Furthermore, this chapter examines four different academic literatures and their contributions to the field of engineering, in particular fluid mechanics and hypersonic flow.

Chapter 3 – Project Design and Methodology

3.1 Introduction

Within this chapter, the project design and methodology will aim to provide an overview of the design and manufacturing of the project. The chapter begins by briefly identifying and outlining the TUSQ facility major components and operating conditions. The chapter then continues to outline three different design options and testing procedure that would be used in the testing phase of the experiment. Furthermore, the design is also examined in this chapter and implements a decision matrix to identify the most suitable design for this experiment. This chapter then concludes with the calculated expected theoretical forces acting on the test objects during the testing phase of the experiment assuming and approximating the drag coefficient, pitot pressure, duration and distance that the object will cover during testing.

3.2 Design Overview – Testing Facility

The TUSQ facility Ludwieg tube with free piston compression heating is used to generate a Mach 6 hypersonic quasi-steady cold flow for approximately 200ms (Birch 2019, pp. 23-26). Furthermore, this facility located at the Toowoomba campus in Queensland can be configured to produce other Mach numbers and in an atmospheric blowdown mode of operation (Birch 2019, pp. 23-26). The schematic of this TUSQ facility is outlined in Fig 3.1, with the major components outlined and listed in Table 3.1 (Birch 2019, pp. 23-26).

Prior to testing, the TUSQ facility is comprised of three separate volumes of gas; the 350-litre high pressure air reservoir, the air contained within the Ludwieg tube/barrel, and the low-pressure region with less than 1 kPa within the testing container, nozzle and dump tanks (Birch 2019, pp. 23-26). Furthermore, prior to testing the piston inside of the barrel/tube is positioned immediately downstream of the primary valve, where a light Mylar diaphragm used to separate the barrel and the nozzle inlet (Birch 2019, pp. 23-26).

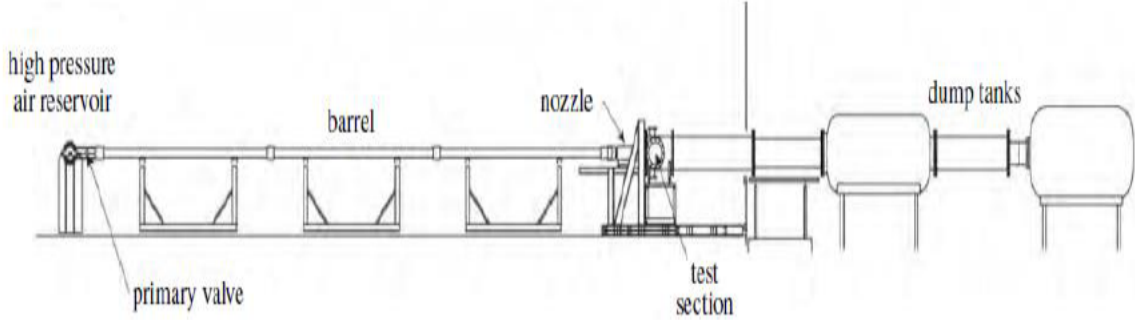


Figure 3.1: Schematic of TUSQ facility with main components (Birch 2019, pp. 23-26).

Component	Characteristics
HP air reservoir	$V = 350 \text{ L}$
Primary valve (Ball Valve)	$\emptyset = 27.6 \text{ mm}$
Piston	$m = 340 \text{ g, Nylatron}$
Barrel	$\emptyset = 130 \text{ mm}, L = 16 \text{ m}$
Test Section	$\emptyset = 600 \text{ mm}, L = 830 \text{ mm}, V = 0.235 \text{ m}^3$
Dump tanks	$V = 12.5 \text{ m}^3$

Table 3.1: TUSQ Facility Components (Birch 2019).

Once an experiment is set up in position and is ready to begin, the pneumatically actuated primary valve begins to open at a relative speed of approximately 500ms (Birch 2019, pp. 23-26). By using a relative low speed, this decreases the magnitude of the piston's oscillations, which in turn decreases the oscillations of the pressure within the barrel during the compression stage (Birch 2019, pp. 23-26). The high-pressure air contained within the reservoir is then released through the primary valve, forcing the piston along the barrel/tube and compressing the gas until it ruptures the diaphragm that is 67mm upstream of the nozzle's throat (Birch 2019, pp. 23-26). Once the diaphragm is ruptured, the gas is then accelerated through the nozzle and into the testing area/section (Birch 2019, pp. 23-26). Furthermore, as stated by Birch (2019, pp. 23-26) the nominal testings condition is outlined in Table 3.2, and supported by other academic sources. Where, ' P_o ' is the nozzle reservoir stagnate pressure, ' T_o ' is the stagnation temperature, ' M ' is the Mach number, ' u_∞ ' is the freestream velocity, ' P_∞ ' is

the freestream pressure, ‘ T_∞ ’ is the freestream temperature, ‘ P_{pt} ’ is the Pitot pressure, ‘ Re_u ’ is the Reynolds number, and ‘ Re_D ’ is the Reynold’s number at the exit nozzle (Birch 2019, pp. 23-26).

P_o (Mpa)	T_o (K)	P_∞ (Pa)	T_∞ (K)	M	u_∞ (m/s)	P_{pt} (kPa)	Re_u (m^{-1})	Re_D
1.0	576	702	71	5.9	1006	31.8	6.98×10^6	1.51×10^6

Table 3.2: TUSQ Facility Standard Operating Conditions (Birch 2019, pp. 23-26).

3.2.1 Design Options

In order to determine the most practical solution to testing this project a variety of options will need to be outlined and considered. These options are as follows;

- Option One – is comprised of multiple batteries including; a three-volt battery holder, holding two AA batteries and a six-voltage battery holder, holding four AA batteries, a six-volt Direct Current (DC) motor rated to produce 9 000 RPM, the apparatus including; the testing platform, the motor housing unit, the stabilising platform, two 3mm bolts and nuts and the pre-fabricated release mechanism.

In order to test this option, the apparatus will be first secured on the release mechanism and locked into position. The motor will then be connected to a battery outside of the chamber. Once the chamber is locked and secured, the batteries will be connected and the motor will start to spin, rotating the test piece. The wind tunnel will then start up and once it reaches the desired speed the release mechanism will be activated and the object will start to freefall. While the object is freefalling, the wind tunnel will have reached the required conditions and the diaphragm will rupture, where the test object will be tracked by a high-speed camera. This will then be repeated for each test piece.

- Option Two – will be comprised of two nine-volt battery holder with the required battery nine-volt batteries in parallel, a six-volt DC motor rated to produce 9 000 RPM, the apparatus including; the testing platform, the motor housing unit, the stabilising platform, two 3mm

bolts and nuts, the pre-fabricated release mechanism and a speed Pulse-width Modulation (PWM) motor controller with a digital display and push start button.

In order to test this option, the motor and the motor housing will be first secured on the assembly and locked into position. The motor will then be connected to the PWM motor controller and battery assembly outside of the chamber. Once the chamber is locked and secured, the start button will be pressed and the motor will start to spin, rotating the test piece. Once the test piece has reached the desired RPM of test object, the wind tunnel will then start up and once it has reached the desired speed the release mechanism will be activated and the object will start to freefall. While the object is freefalling, the wind tunnel will have reached the required conditions and the diaphragm will rupture, where the test object will be tracked by a high-speed camera. This will then be repeated for each test piece.

- Option Three - will be comprised of a nine-volt battery holder with the required battery nine-volt battery, a six-volt DC motor rated to produce 9 000 RPM, the apparatus including; the testing platform, the motor housing unit, the stabilising platform, two 3mm bolts and nuts, the pre-fabricated release mechanism, microcontroller, motor shield and start button.

In order to test this option, the motor and the motor housing will be first secured on the assembly and locked into position. The motor will then be connected to the motor shield and the microcontroller assembly with the correct code loaded on the microcontroller. Once the chamber is locked and secured, the start button will be pressed and the motor will start to spin, rotating the test piece. Once the test piece has reached the desired RPM of test piece, the wind tunnel will then start up and once it has reached the desired speed the release mechanism will be activated and the object will start to freefall. While the object is freefalling, the wind tunnel will have reached the required conditions and the diaphragm will rupture, where the test object will be tracked by a high-speed camera. This will then be repeated for each test piece.

3.3 Final Design

In order to decide the most viable option for performing this project, each option will be analysed via a decision matrix. The decision matrix will be comprised on the design criteria where each option will

be ranked on a scale from one to three. As outlined in Table 3.3 the design criteria include the following; complexity of producing the design, the cost required, the risk of an injury occurring, the reliability of the equipment, the accuracy of the data collected and the material/equipment availability. Therefore, as outlined and presented in Table 3.3 the ideal option is ‘Option Two’.

Design Criteria	Option 1	Option 2	Option 3
Complexity	3	3	1
Cost	3	2	1
Risk of Injury	1	3	3
Reliability	1	2	3
Data Accuracy	1	3	3
Material/equipment Availability	3	2	1
Total	12	15	12

Table 3.3: Design Option Decision Matrix.

3.3.2 Apparatus Design and Limitations

In order to complete this research project, the limitations and design restrictions required to the design of the release mechanism’s mounting apparatus needs to be considered and outlined. Therefore, after recording the release mechanism and the hypersonic wind tunnel dimensions, the limitation to the dimensions for each of the apparatus components were determined and are outlined in Table 3.4 (schematics are displayed in Appendix D). Furthermore, during the design stage, the dimensions of the DC motor were taken into consideration when designing the motor housing unit and the test platform (as outlined in Table 3.4).

Apparatus Components	Height (mm)	Width (mm)	Depth (mm)	Shaft Outer Diameter (mm)	Shaft Inner Diameter (mm)	Diameter of Hole Extrusion (mm)
Motor Housing Unit	32	58.5	45	N/A	N/A	3.3
Test Platform	25	32	32	5	2.4	N/A
Stabilising Plate	2	58.5	45	N/A	N/A	3.3
DC Motor Shaft	12.5	N/A	N/A	2.3	N/A	N/A
DC Motor	38.5	N/A	N/A	27.6	N/A	N/A

Table 3.4: Design Limitations and Equipment Requirements.

3.3.2 Test Objects

In order to simulate the freefalling and tumbling motion of an object, the dimensions of the test shapes will need to be identified. However, due to the time restrictions only one of the objects will be tested and analysed. These test objects are as follows; sphere, cube, cylinder, and rectangle (as seen in Figs 3.2, 3.3, 3.4, and 3.5, respectively). Each of these objects will be modelled within Cero and machined to size comprising of a dense material similar to low grade steel and limited to the maximum size of 25.4mm. Furthermore, the schematics/drawings of these test objects are outlined in Appendix E.

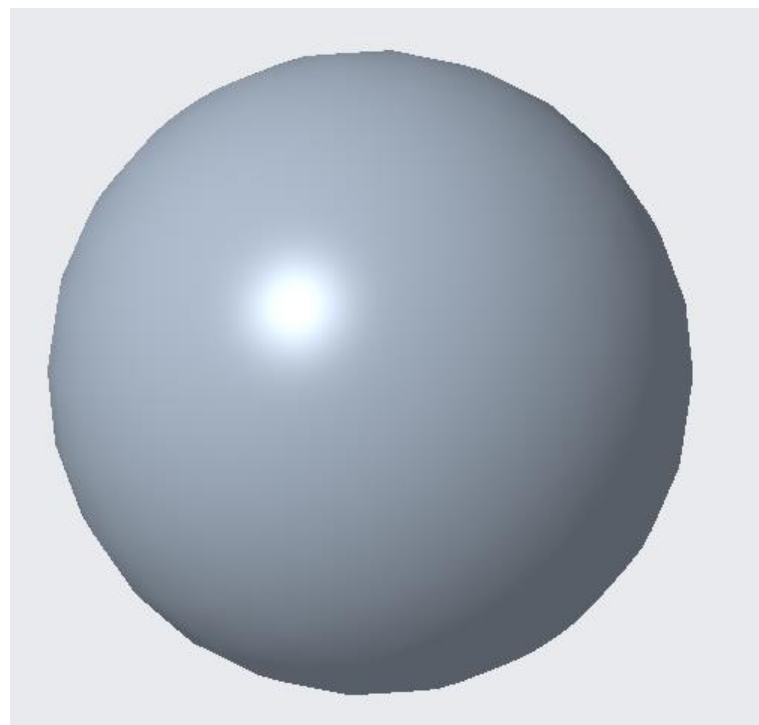


Figure 3.2: Sphere Test Object.

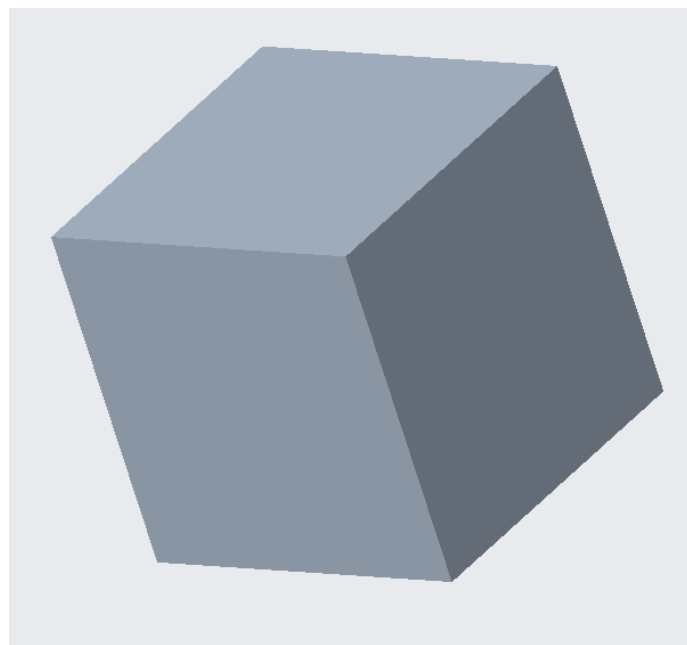


Figure 3.3: Cube Test Object.

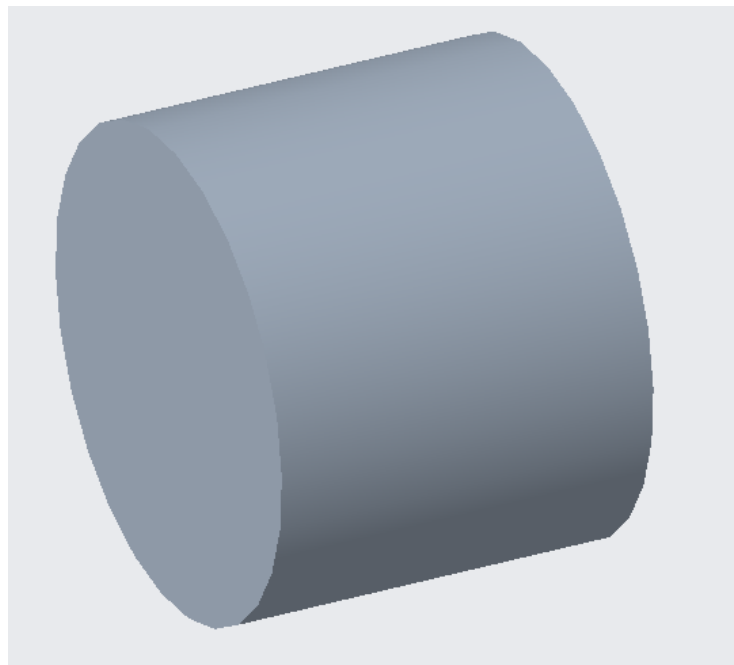


Figure 3.4: Cylinder Test Object.

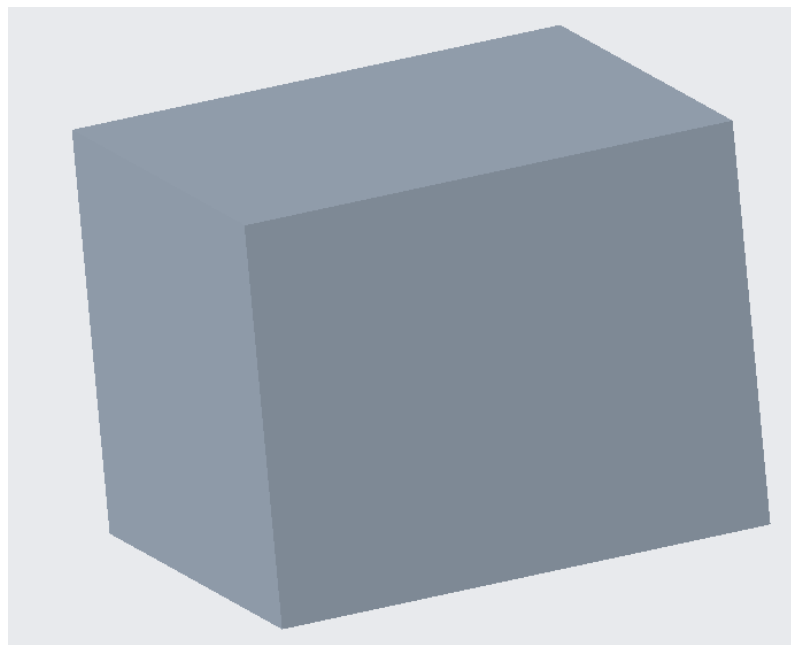


Figure 3.5: Rectangle Test Object.

3.4 Testing Procedure

In order to complete this project, this project will undergo five stages of testing. These include; the freefall test, the performance test, the preliminary/bench test at the TUSQ facility, the final test within the hypersonic wind tunnel and if there is time available the modification test within the hypersonic wind tunnel.

The freefall test will involve test a crude design involving just a motor connected to a battery and a test object. This will be used to provide a basic understanding on the concept of freefalling objects.

The performance test will involve the development and manufacturing (3D printing) of the apparatus that will be attached to the release mechanism. This stage will also incorporate the equipment that will be utilised throughout the project. In addition, this test will also examine the effect of the test object attached to the apparatus. Furthermore, this stage will incorporate any modifications that the apparatus would need before moving onto the preliminary/bench tests.

The preliminary/bench test will involve all of the equipment and all parts of the apparatus including the release mechanism. This stage of the testing will be performed at the TUSQ facility in Toowoomba, Queensland. During this stage, the apparatus and the test object will be mounted to the release mechanism, where each test will be recorded by a high-speed camera and the RPM of the object will be calculated from the recordings and measured by a tachometer. Furthermore, this stage will incorporate any modifications that the apparatus would need before moving onto the final test.

The final test will involve the equipment and all of the finalised parts of the apparatus including the release mechanism. At this stage of the testing procedure, the test will be performed within the TUSQ facility, where the DC motor will start to rotate. Once the object reaches the desired speed the release mechanism will be triggered and the test object will perform its freefall, while simultaneously the piston inside the barrel chamber is triggered and starts to compress the fluid. Once the diaphragm reaches the rupturing point, the fluid will be released into the testing chamber, where it will interact with the test object. Furthermore, this test will also be recorded by a high-speed camera located outside of the testing chamber. Furthermore, if there is enough time, modifications will be performed in order to improve the results of the recorded data where the test object can be retested.

3.5 Theoretical Design Calculations for the Test Objects

As previously stated, the test objects will be a cube, sphere, cylinder, and rectangle. However, before testing commences, certain design calculations are required and are outlined within this section. These requirements are as follows; drag force, frictional force, acceleration, mass, and the number of revolutions experienced during flight. Furthermore, the drag coefficient values for the cube, sphere, cylinder and rectangle are 1.05, 0.45, 1.2 and 2.05, respectively (as outlined in Table 3.5) (Carvill 1993; Nilsson & Aarønæs 2014). In addition, the assumed values for each of the following properties; the distance travelled, time travelled, coefficient of friction and pitot pressure that will be used for theoretical calculations to determine the properties and forces acting on the test objects are outlined in Table 3.5. Additionally, the dimensions for each of the test objects are outlined in Table 3.6. Therefore, by utilising the information contained in Tables 3.5 and 3.6, the determined theoretical properties and forces that each of the test objects will experience during testing can be determined. This is outlined in Table 3.7, where the full details of the calculations for each of the test objects are outlined in Appendix G. Furthermore, the expected number of revolutions per second and the revolutions per 50 msec. for each proposed speed of the test objects are outlined 3.8.

Assumed Properties	Test Object			
	Cube	Sphere	Cylinder	Rectangle
Acceleration (m/s^2)	100	100	100	100
Time (s)	0.2	0.2	0.2	0.2
Coefficient of Friction	0.2	0.2	0.2	0.2
Pitot Pressure (kPa)	31.8	31.8	31.8	31.8
Coefficient of Drag	1.05	0.45	1.2	2.05

Table 3.5: Assume Property Values for Each Test Object

Test Object	Dimensions (mm)			
	Length	Width	Height	Diameter
Cube	0.0254	0.0254	0.0254	N/A
Sphere	N/A	N/A	N/A	0.0254
Cylinder	N/A	N/A	0.0254	0.02
Rectangle	0.02	0.02	0.0254	N/A

Table 3.6: Dimension Limitations for the Test Objects.

Table 3.7 outlines a summary of the theoretical calculations perform on the four test objects.

Object	Force Applied (N)	Mass (kg)	Drag Force (N)	Frictional Force (N)
Cube	20.516088	0.20516088	10.7709462	0.4025256466
Sphere	32.22659567	0.3222659567	3.625492013	0.632285807
Cylinder	17.6827681	0.176827681	10.60966086	0.3469359115
Rectangle	15.0096	0.150096	15.38484	0.294488352

Table 3.7: Summary of Theoretical calculations for all of the test objects.

RPM	Rev/s	Rev/0.05
1000	16.66667	0.833333
2000	33.33333	1.666667
3000	50	2.5
4000	66.66667	3.333333
5000	83.33333	4.166667
6000	100	5
7000	116.6667	5.833333
8000	133.3333	6.666667
9000	150	7.5
10000	166.6667	8.333333

Table 3.8: Object's Revolution Per Second.

3.6 Conclusion

In summary, this chapter outlined the TUSQ facility and the major components and the standard operating conditions that the facility delivers. Furthermore, this chapter also examined, identified and recommended one design out of the three possible design options that could be used to perform this experiment. This chapter also explored the theoretical forces and the testing conditions that will be imposed on the test objects, by assuming and approximating the drag coefficient, pitot pressure, duration and distance that the test object will cover during testing.

4 Results and Discussion

4.1 Introduction

Within this chapter, the results and discussion will aim to establish and outline the results that have been collected for both the preliminary/bench tests and the final test. Furthermore, this chapter will be separated into three sections, the preliminary/bench tests, the final test and the discussion of the results. This chapter begins by first outlining the preliminary/bench test components and equipment used throughout the tests. The chapter will then present images/snapshots of different frames for both with and without a load of 88.7g applied to the apparatus. The chapter will then finalise the first part of this chapter with the results collected from the preliminary/bench tests. For the second stage of this chapter, this section will begin with outlining the components and equipment used throughout the test. The chapter will then present and explain the images/snapshots of different frames that were captured throughout the test. This will then lead to the final stage of this section where it will perform an analysis on the results and calculations on the test object characteristics and the conditions of the fluid's flow properties. This will then lead to the final stage of this chapter, where it will outline and discuss the key findings from the results.

4.2 Preliminary Results

As mentioned in the previous chapter, the preliminary test was designed to test the design of an apparatus with the release mechanism and the test object outside of the TUSQ facility. These tests were comprised of two 9V batteries in parallel, the PWM speed controller, the 6V DC motor, the motor housing unit, the stabilising platform, the test object platform and the test object. During the preliminary/bench test, the apparatus was mounted on the release platform outside of the TUSQ facility (as displayed in Fig 4.1). Once the apparatus was mounted and the DC motor, PWM speed controller and the batteries were connected, the test was able to be carried out. Furthermore, in order to capture the necessary data to determine the RPM of the test object, a high-speed camera and tachometer was employed.

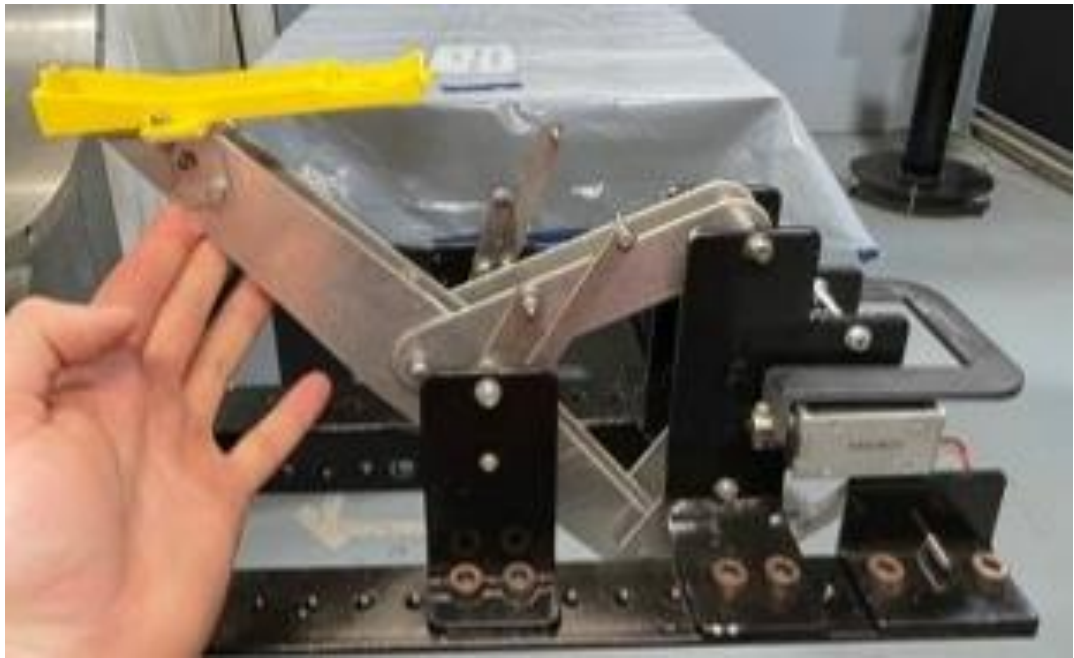


Figure 4.1: Image of the Release Mechanism.

Each of the tests performed followed the same procedure and the footage of each test was then extracted from a video file into images of each frame. An example of a test with a load of 88.7g and no load with the speed controller set at one-hundred percent is displayed from Figs. 4.2 to 4.5 and Fig. 4.6 to 4.7, respectively. Furthermore, the images of the frames for all of the recorded test intervals are displayed in Appendix F.2 to F.11. These images of the frames were taken at intervals of twenty frames until the test object exited out of view. However, due to the poor quality of the footage for some of the intervals, the next best frame was utilised instead. The poor quality of the images was due to the poor lighting.



Figure 4.2: Frame 1 of Test Object at One-Hundred Percent.



Figure 4.3: Frame 60 of Test Object at One-Hundred Percent.

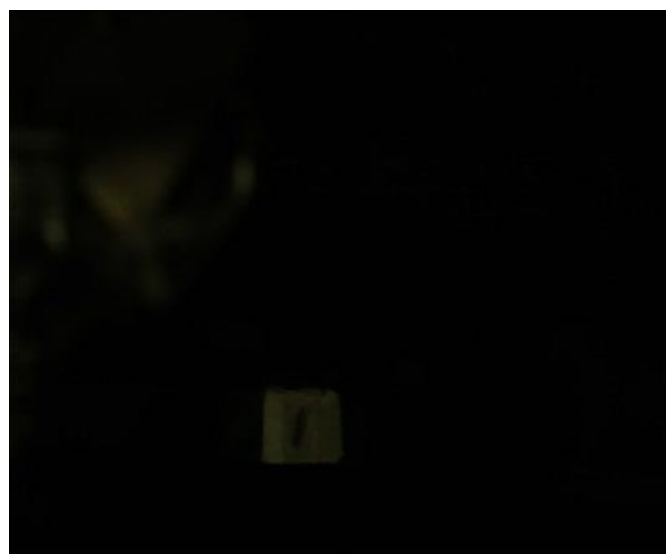


Figure 4.4: Frame 120 of Test Object at One-Hundred Percent.



Figure 4.5: Frame 150 of Test Object at One-Hundred Percent.

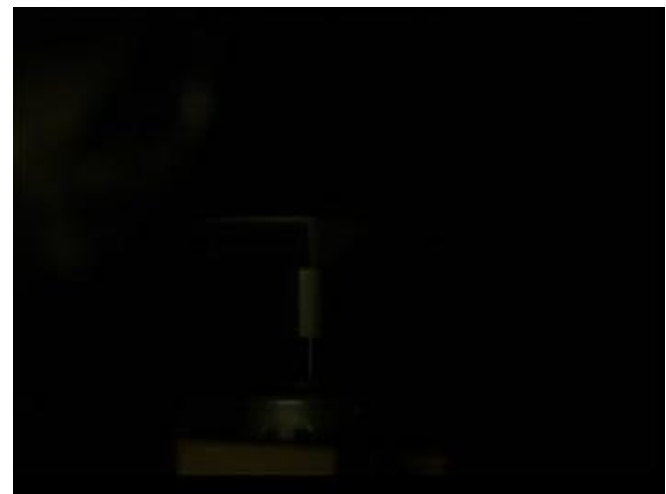


Figure 4.6: Frame 1 with No Load at One-Hundred Percent.

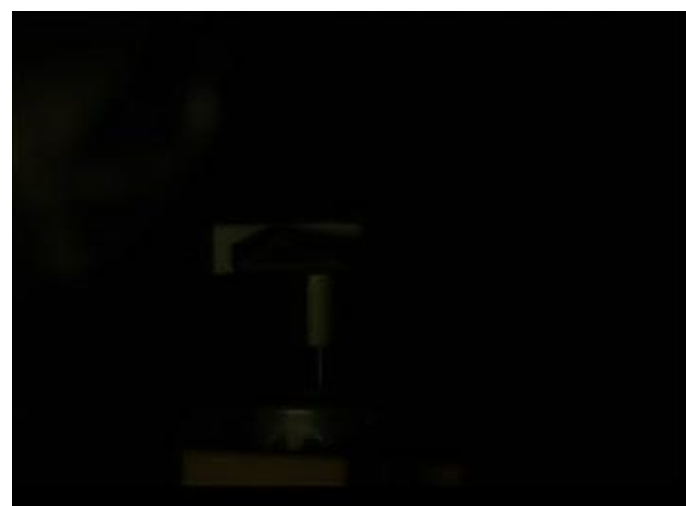


Figure 4.7: Frame 120 with No Load at One-Hundred Percent.

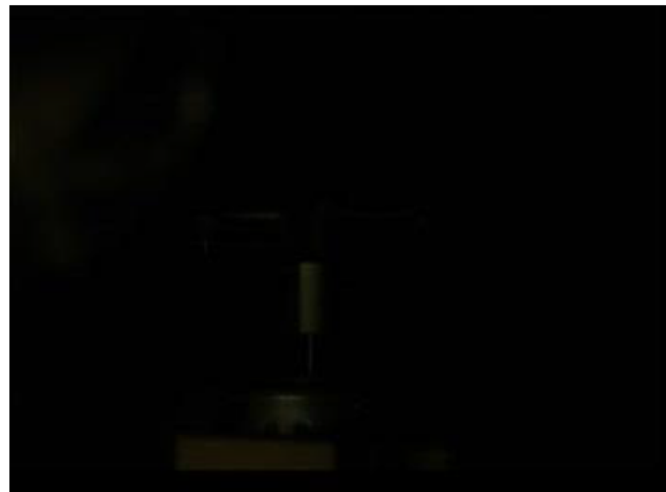


Figure 4.8: Frame 240 with No Load at One-Hundred Percent.

From the recorded and collected data, the approximate measured RPM reading from the tachometer at ten percent intervals starting from twenty percent with no load applied is outlined in Fig. 4.9 and Table 4.1. In addition, the calculated RPM from the footage at one-hundred with no load was also determined.

Percentage (with no Load)	Tachometer RPM Recording	Calculated (approx.)
20	1770	N/A
30	3380	N/A
40	4770	N/A
50	5900	N/A
60	7400	N/A
65	N/A	N/A
70	8300	N/A
75	N/A	N/A
80	8800	N/A
85	N/A	N/A
90	9500	N/A
95	N/A	N/A
100	10600	10688.26

Table 4.1: Test Object's Approximated and Calculated RPM with No Load.

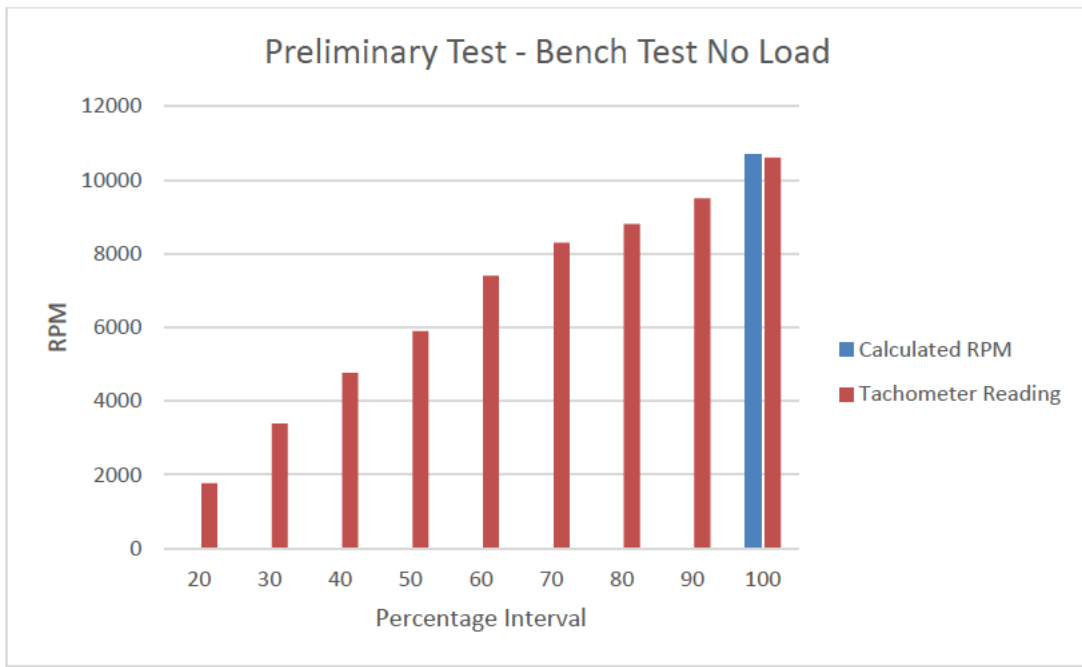


Figure 4.9: Test Object's Approximated and Calculated RPM with No Load.

In addition, from the recorded and collected data, Table 4.2 and Fig. 4.10, outlines the approximate the recorded RPM reading from the tachometer and the calculated RPM from the footage for each test increment, with a test object load of 88.7g. Each test was performed at ten percent intervals starting from twenty percent. However, this then change to five percent intervals after sixty percent. This was due to the uncertainty of the test object staying on the test platform due to centre of mass of the test object being off centre and the vibration from the DC motor.

Percentage (with a load mass of 88.7g)	Tachometer RPM Recording	Calculated RPM (approx.)	Difference	Percentage Error
20 (mass = 88.7g)	1800	3181.82	1381.82	-43.4286
30 (mass = 88.7g)	3400	3448.28	48.28	-1.40012
40 (mass = 88.7g)	4800	4583.33	-216.67	4.727349
50 (mass = 88.7g)	6000	5270.27	-729.73	13.84616
60 (mass = 88.7g)	7200	6666.67	-533.33	7.999946
65 (mass = 88.7g)	7500	N/A	N/A	N/A
70 (mass = 88.7g)	8000	8085.11	85.11	-1.05268
75 (mass = 88.7g)	8400	N/A	N/A	N/A
80 (mass = 88.7g)	8800	8260.87	-539.13	6.52631
85 (mass = 88.7g)	9100	N/A	N/A	N/A
90 (mass = 88.7g)	9400	8260.87	-1139.13	13.78947
95 (mass = 88.7g)	9700	N/A	N/A	N/A
100 (mass = 88.7g)	9900	10000	100	-1

Table 4.2: Test Object's Approximated and Calculated RPM with 88.7g Load.

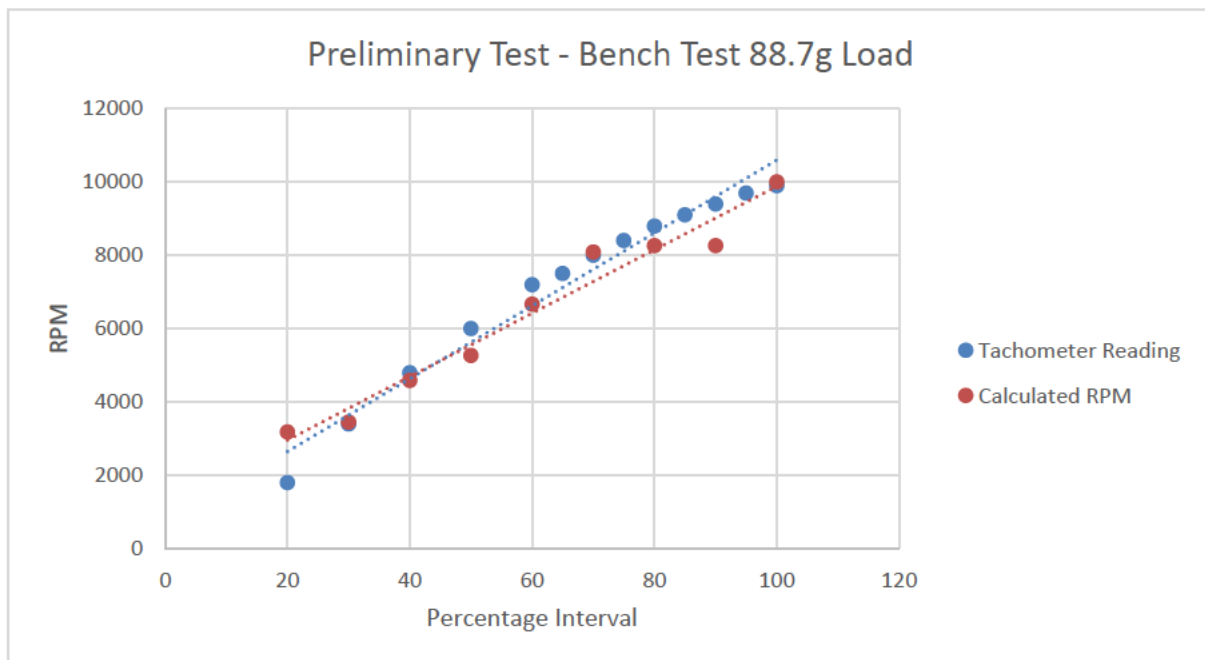


Figure 4.10: Test Object's Approximated and Calculated RPM with 88.7g Load.

4.3 Final Test Results

As previously mentioned, the final tests were initially going to be performed on four different objects, however, due to time restraints the only test piece that was only tested was the cube. In addition, the final test of the test object (cube) was performed at the TUSQ facility at the University of Southern Queensland (USQ) Toowoomba campus in Toowoomba, Queensland Australia. The final and only test conditions were as follows; the test object's dimensions were approximately $25.4 \text{ mm} \pm 0.4\text{mm}$, the supply voltage to the PWM speed controller and the motor was approximately 9.5V and the speed output of the PWM speed controller was set to forty percent. Furthermore, as mentioned in the previous chapters, the voltage supplied to the system was approximately nine volts supplied by two nine-volt batteries in parallel, however, these batteries were changed to a voltage supply unit set at approximately 9.5 volts.

As mentioned in the previous chapter, the final test was to design and test the design of the apparatus with the release mechanism, in combination with the test object in order to simulate a freefalling tumbling object inside of the TUSQ facility. This would be comprised of a power supply unit, the PWM speed controller, the 6V DC motor, the motor housing unit, the stabilising platform, the test object platform and the test object. During the final test the apparatus was mounted on the release platform inside of the wind tunnel (as displayed in Fig. 4.1). Once the apparatus was mounted and the DC motor, PWM speed controller and the power supply unit were connected, the wind tunnel was able to be sealed and the test would be able to be carried out (as seen in Figs. 4.11 to 4.13). Furthermore, once the wind tunnel was sealed the high-speed camera was then placed into position outside of the test section, where it would be used to capture the necessary data and footage.

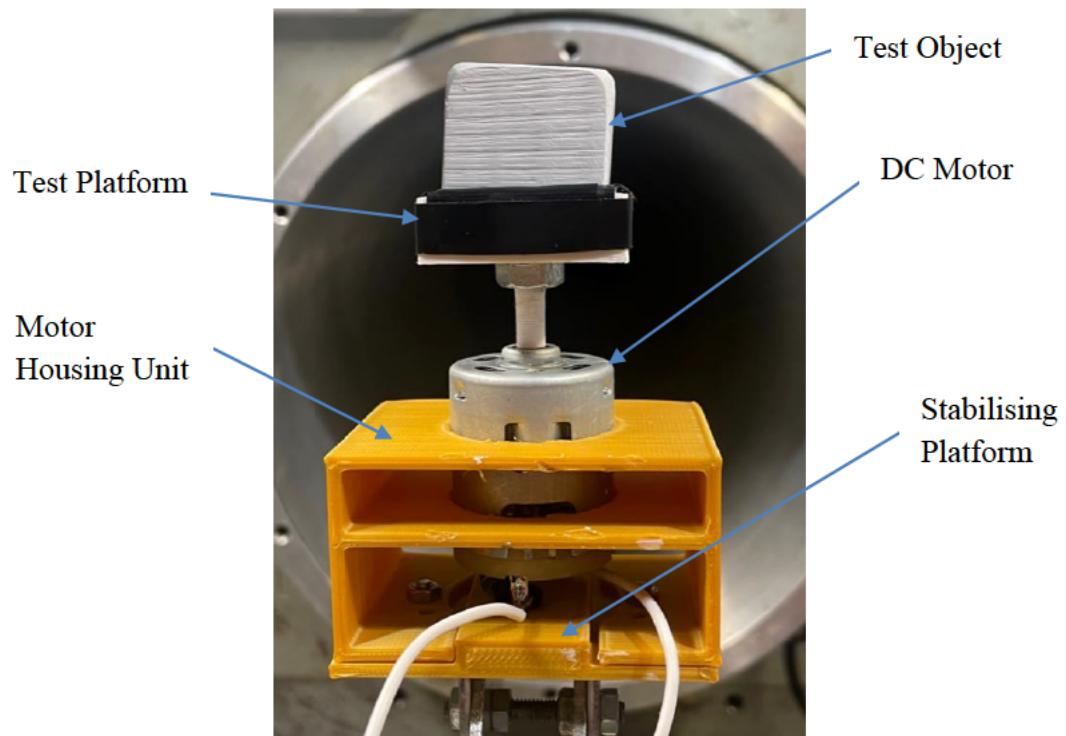


Figure 4.11: Apparatus Assembly on Release Platform.

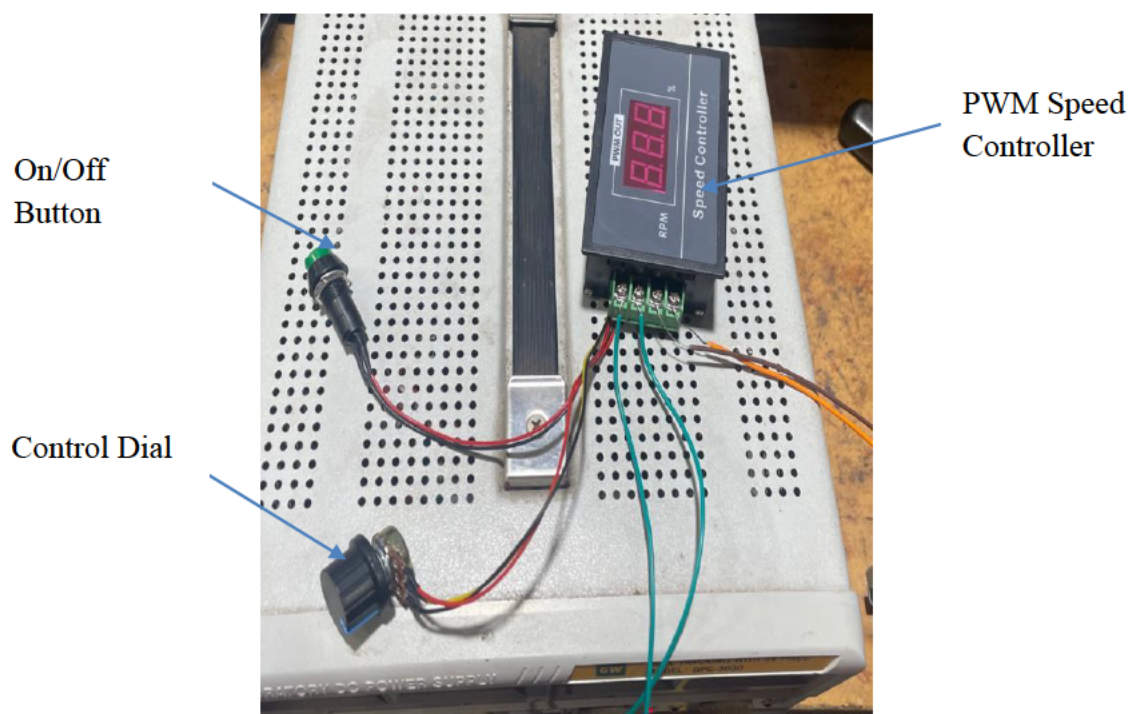


Figure 4.12: Speed Controller.



Figure 4.13: Power Supply Unit.

Once the test was completed and the data was compiled, an analysis of the footage was able to be conducted. The images/snapshots of the selected frames from the final test are outlined in Figs. 4.14 to 4.24. Fig. 4.14 outlines the start of the test, where the test object begins to rotate and reach its maximum speed (at forty percent). This continues until it reaches approximately frame number 200 (0.03125 sec. from the start) as outlined in Fig. 4.16. Where, at this point the release mechanism is triggered resulting in the test object to start to separate from the test platform and perform a freefall while continuing to rotate (as displayed in Figs. 4.16 and 4.17). The test object then continues to freefall until approximately frame 625 (0.09765625 sec. from the start) where the diaphragm ruptures and flow is released into the test section (as displayed in Fig. 4.21). This flow then travels towards the test object, where the flow starts to slows down and exerts a force on the rotating surface face and edge, thus resulting in the formation of the shockwave. This then continues as the test piece continues to rotate until it is pushed out of view of the high-speed camera (as seen in Figs. 4.21 to 4.24). Furthermore, a more detailed video breakdown by frames is outlined in Appendix F.1, where the interval between each frame is twenty-five.

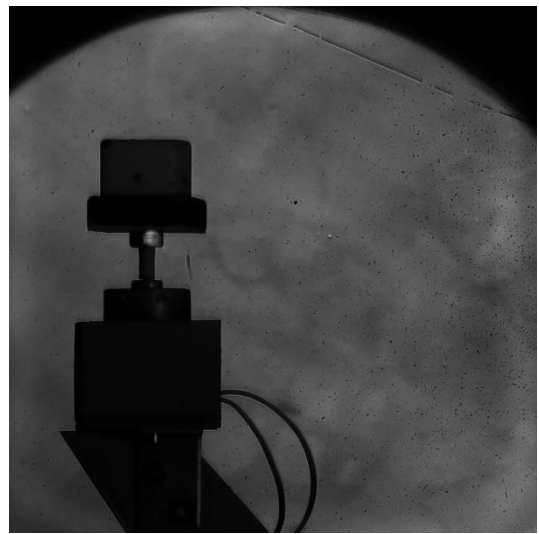


Figure 4.14: Frame 1 of Final Test at Forty Percent.

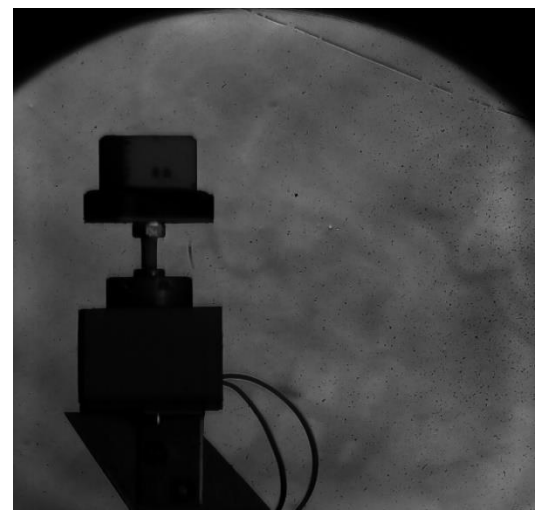


Figure 4.15: Frame 100 of Final Test at Forty Percent.

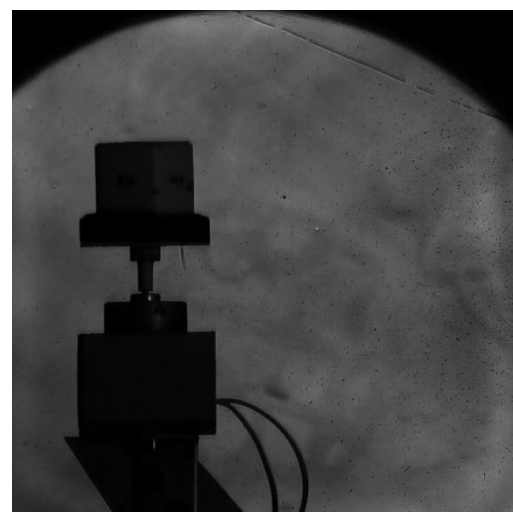


Figure 4.16: Frame 200 of Final Test at Forty Percent.

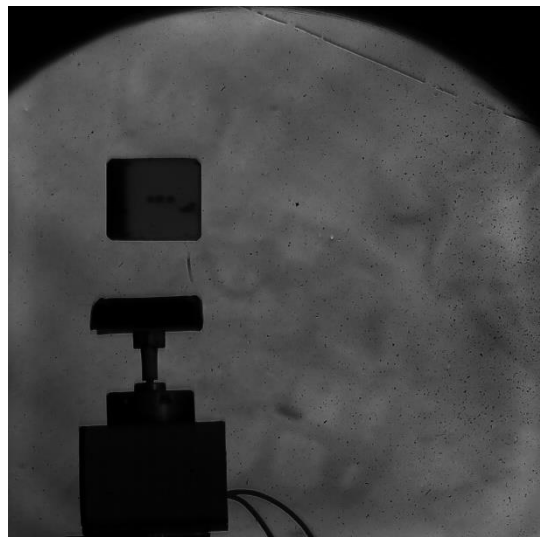


Figure 4.17: Frame 300 of Final Test at Forty Percent.

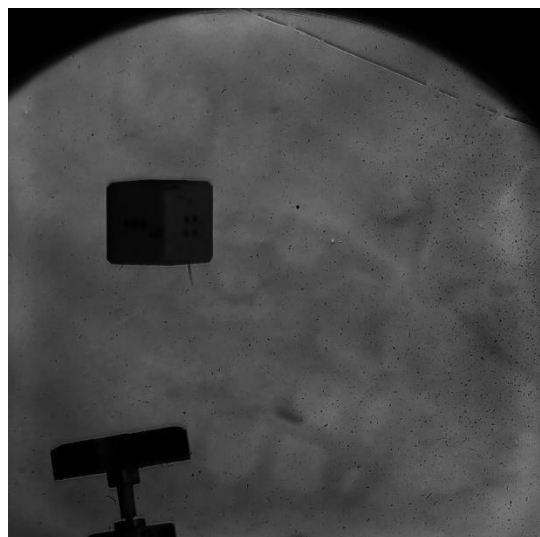


Figure 4.18: Frame 400 of Final Test at Forty Percent.

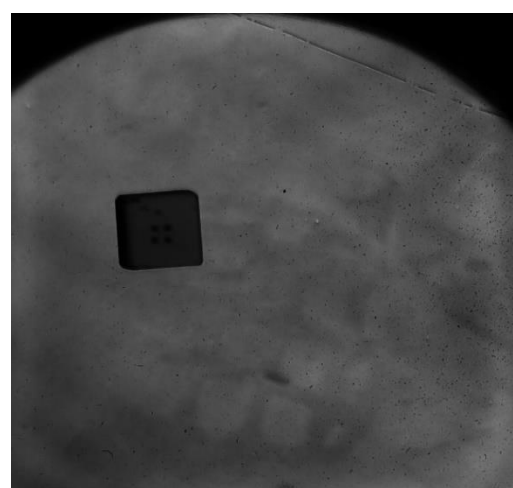


Figure 4.19: Frame 500 of Final Test at Forty Percent.

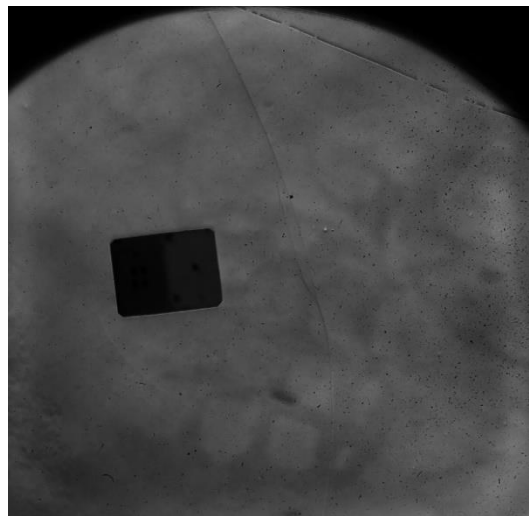


Figure 4.20: Frame 600 of Final Test at Forty Percent.

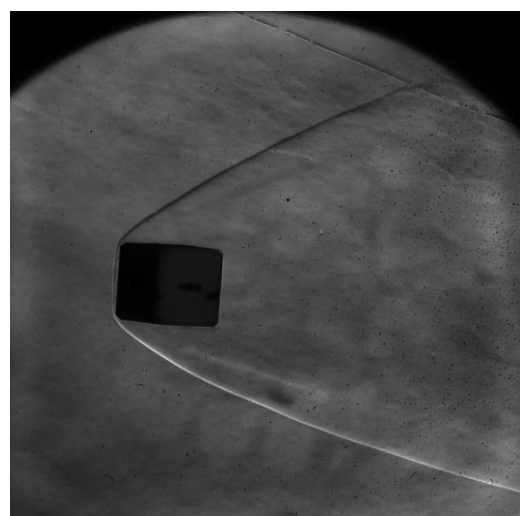


Figure 4.21: Frame 625 of Final Test at Forty Percent.

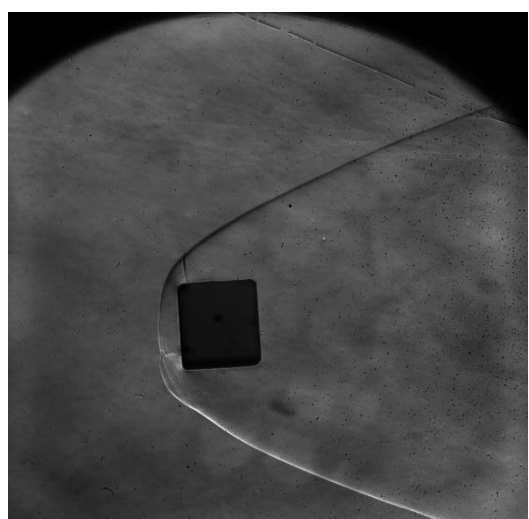


Figure 4.22: Frame 700 of Final Test at Forty Percent.

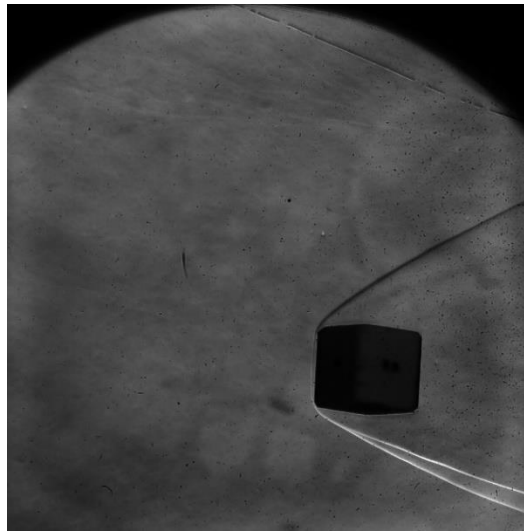


Figure 4.23: Frame 800 of Final Test at Forty Percent.

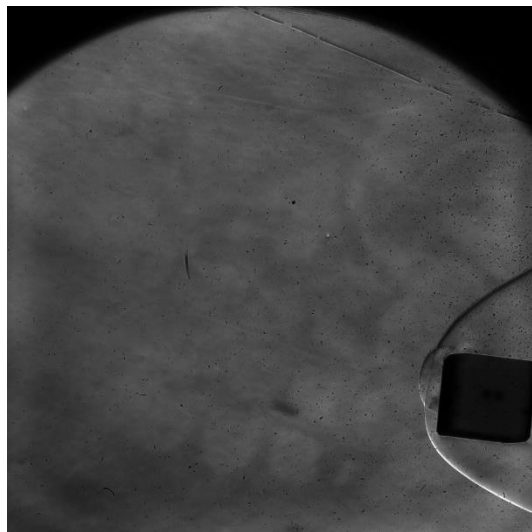


Figure 4.24: Frame 850 of Final Test at Forty Percent.

Furthermore Fig. 4.25 outlines the stagnation pressure and the test section pressure throughout the duration of the experiment. Once the piston was released from the end of the barrel and the flow started to compress (increasing the readings from the stagnation pressure gauge) to a point where the diaphragm ruptured. The pressure within the test section recorded a peaked pressure value above 3500 Pa and then fell below 3000 Pa for the remaining duration. While the recorded stagnation pressure reached within the range of 1.0 to 1.2 MPa.

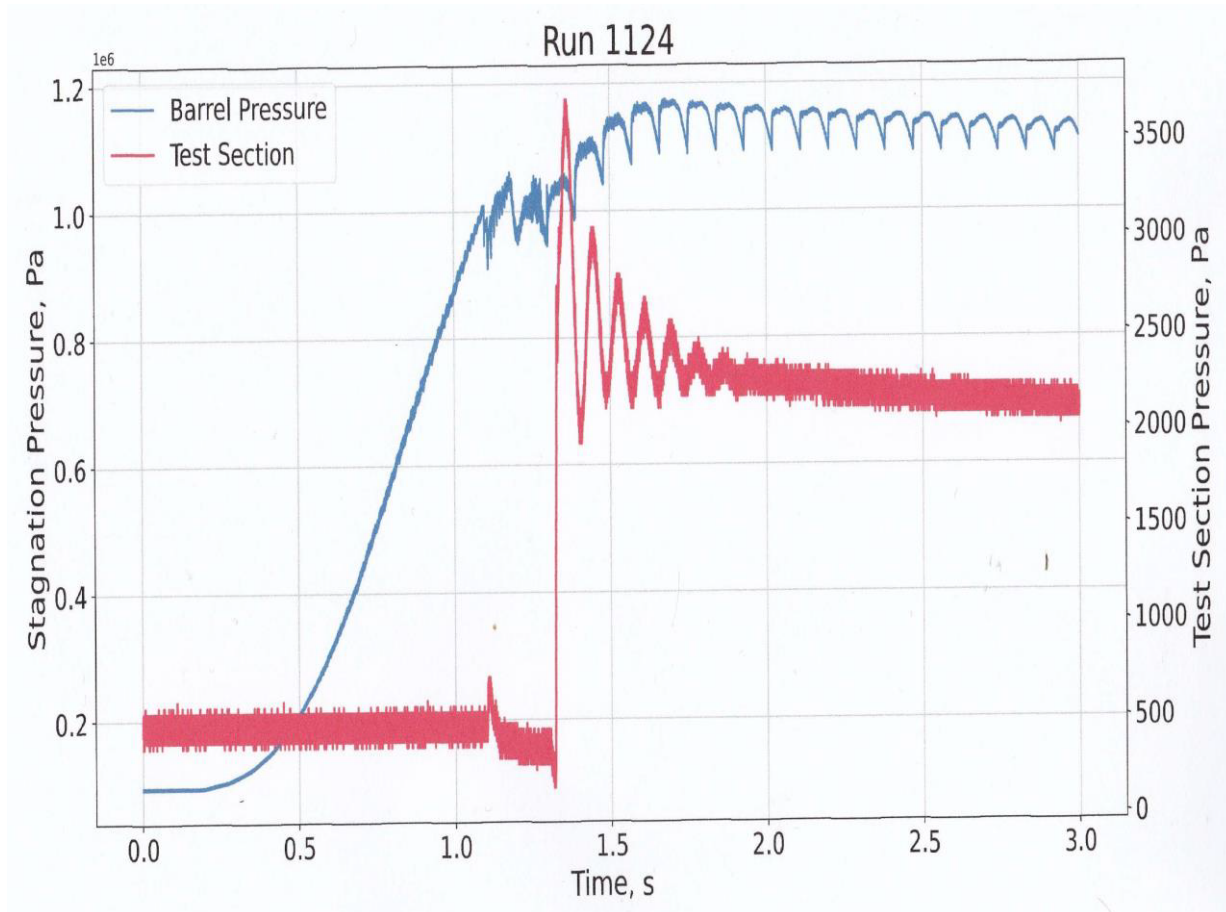


Figure 4.25: Experiment Pressure Results.

After compiling the collected recorded data and processing through Photron FastCam Viewer, the test object's trajectory was able to be obtained at two different locations. These were at the centre of the object and the top left corner of the object. This was achieved by first manually calibrating the scale of the image to 0.164931588mm/pixel by calibrating the distance between two points to 25.3mm and by selecting the recording's origin location (as displayed in Fig. 4.26). Once the calibration of the recording was achieved, the test object's trajectory was able to be determined by manually selecting the same approximate position on the test object for both regions. These selected positions of the test object for both scenarios were then extracted to an excel file and are graphically represented in Figs. 4.27 to 4.32. Figs. 4.27 and 4.28 graphically displays the vertical and horizontal position of the test object in relation to time, for both the centre of the object and at the top left corner, respectively. Figs. 4.29 and 4.30 graphically displays the vertical and horizontal position of the test object in relation to the frame number, for both the centre of the object and at the top left corner, respectively. Figs. 4.31

and 4.32 graphically displays the trajectory of the object with respect to the origin, for both the centre of the object and at the top left corner, respectively.

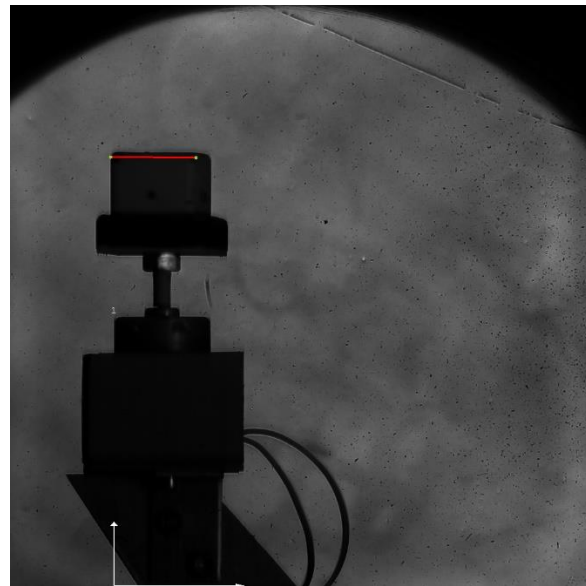


Figure 4.26: Calibration of the Video.

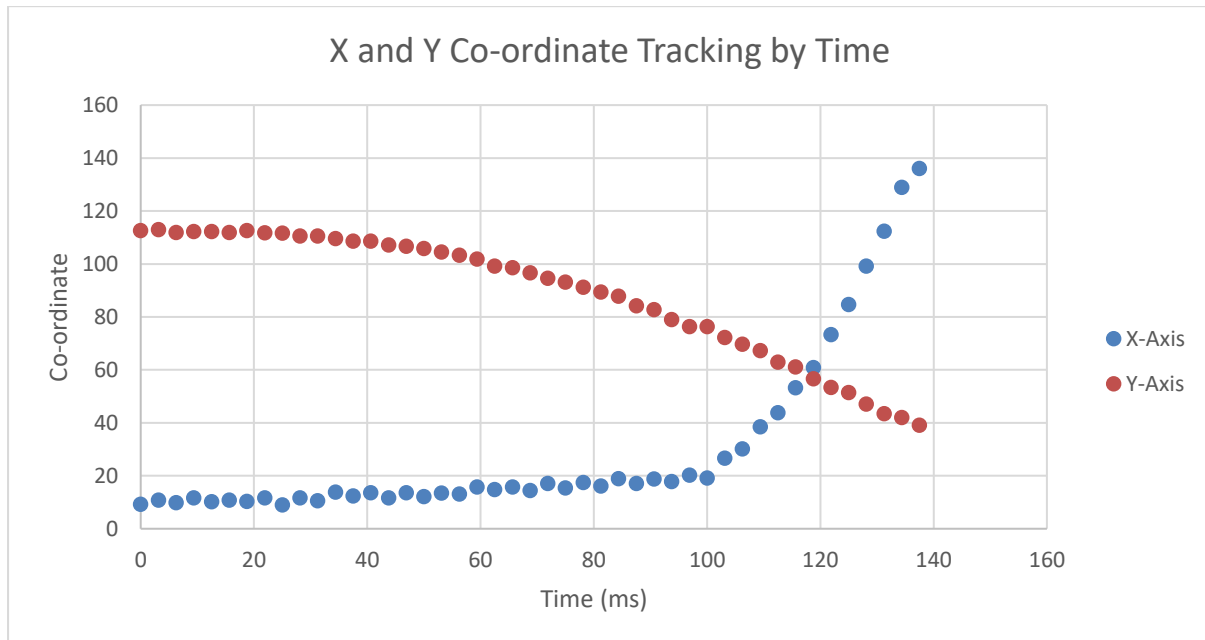


Figure 4.27: X and Y Co-ordinate of the Test Object in Relation to time at the centre of the object.

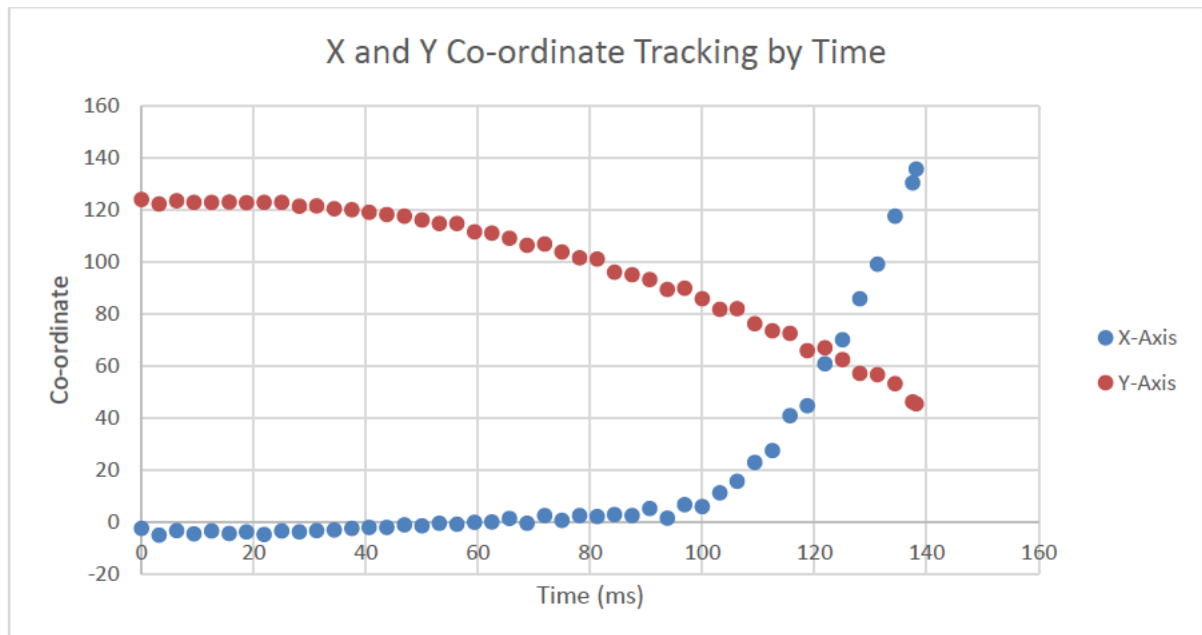


Figure 4.28: X and Y Co-ordinate of the Test Object in Relation to time at the top left edge of the Object.

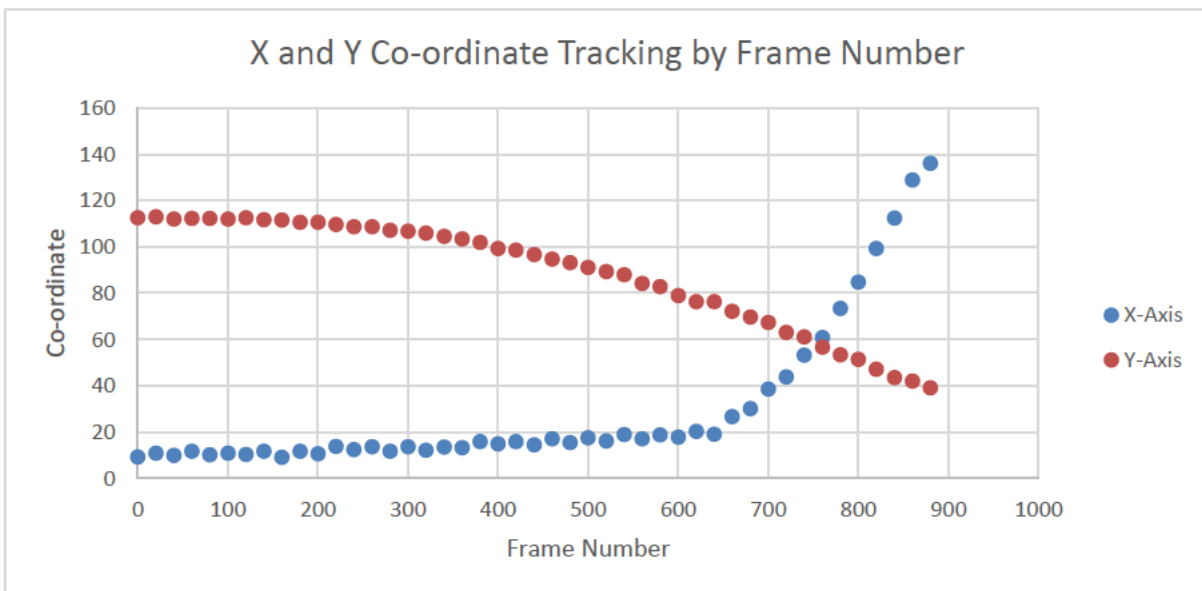


Figure 4.29: X and Y Co-ordinate of the Test Object in Relation to Frame Number at the centre of the Object.

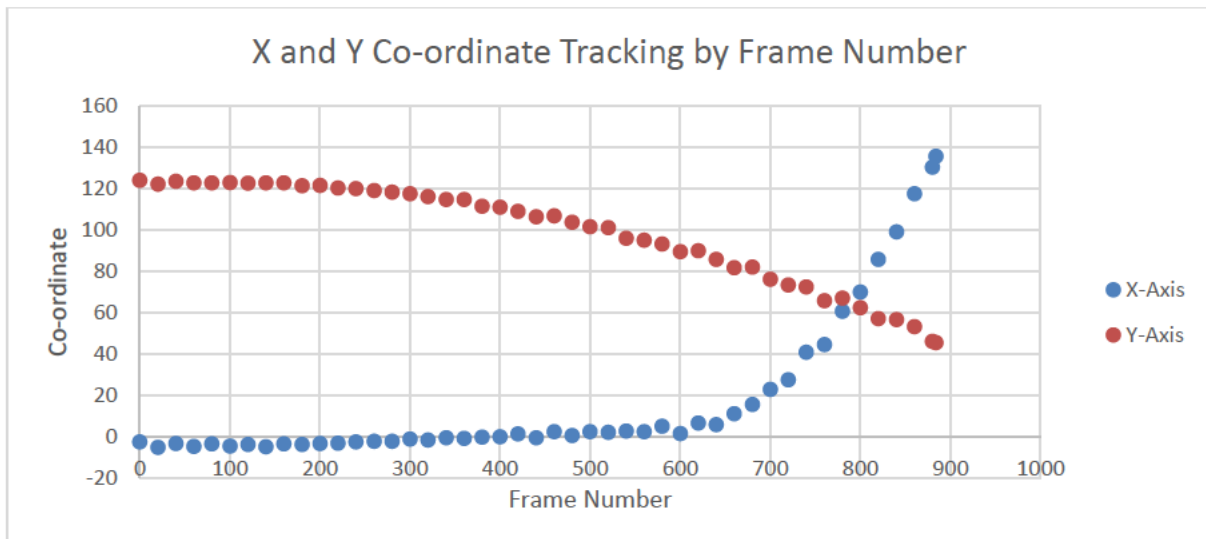


Figure 4.30: X and Y Co-ordinate of the Test Object in Relation to Frame Number at the top left edge of the Object.

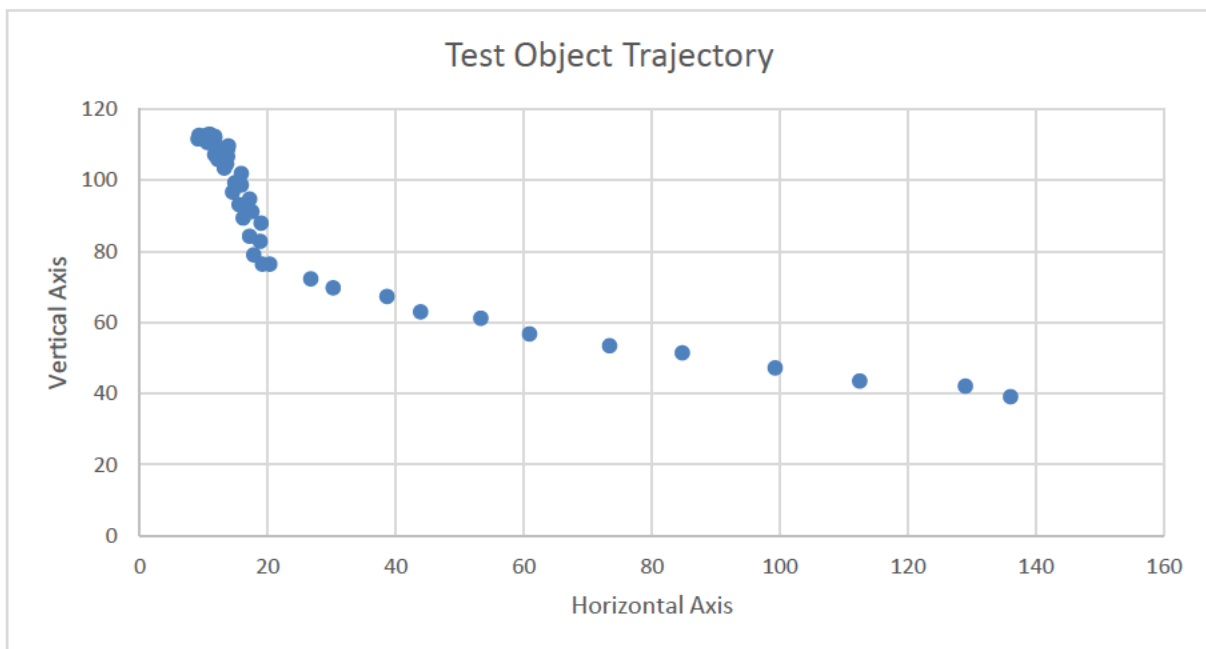


Figure 4.31: Test Object Trajectory at the Centre of the Object.

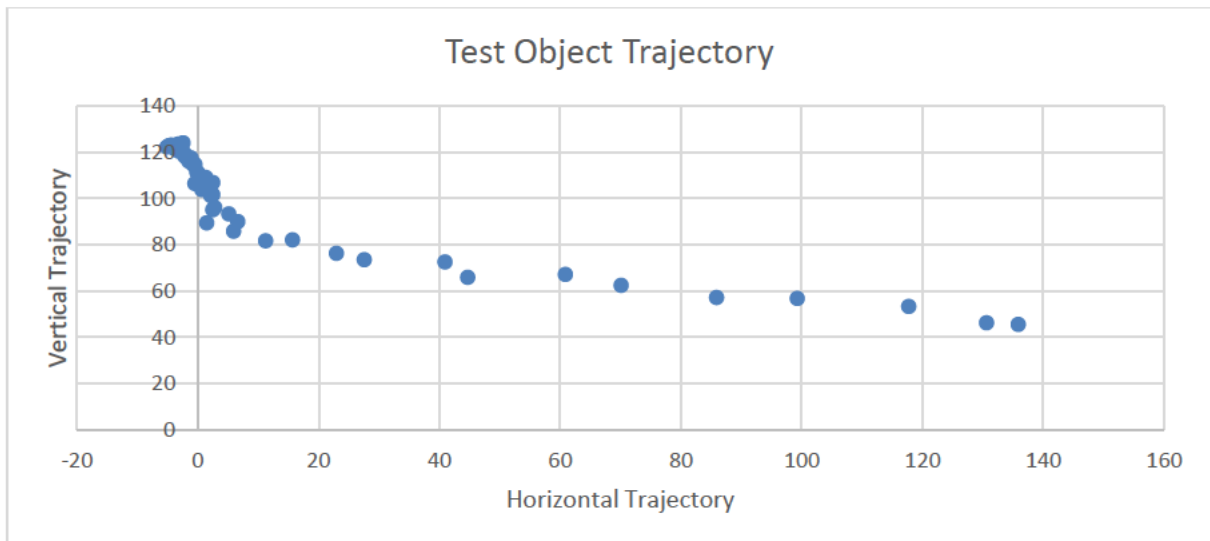


Figure 4.32: Test Object Trajectory at the top left edge of the Object.

4.3.1 Experimental Calculations

By analysis the experiment's test footage and all of the frames (1001 frames over 0.156406 sec.), the footage revealed that the test object performed sixteen full rotations. However, the sixteen rotations were only carried out over 880 frames (over approximately 0.13763 sec.). Therefore, the approximate RPM of the test piece at forty percent is as follows:

$$RPM = \frac{1}{0.13763} \times 60 \times 16 \quad (4.1)$$

$$RPM = 6975.223425$$

$$RPM \approx 6975.22$$

Therefore, the approximate RPM is 6975.22.

Calculating error percentage:

$$Error\ Percentage = \frac{Experimental - Theoretical}{Theoretical} \times 100 \quad (4.2)$$

$$\text{Error Percentage} = \frac{6975.2234525 - 4583.33}{4583.33} \times 100$$

$$\text{Error Percentage} = 52.18680403$$

$$\text{Error Percentage} \approx 52.19$$

Therefore, there is a percentage error between the preliminary/bench test and the final test of approximately 52.19.

Furthermore, the project's testing conditions such as the drag coefficient of the test piece and the test section's temperature, pressure and density are as follows and are determined from the test object's trajectory outlined in Figs. 4.33 and 4.34:

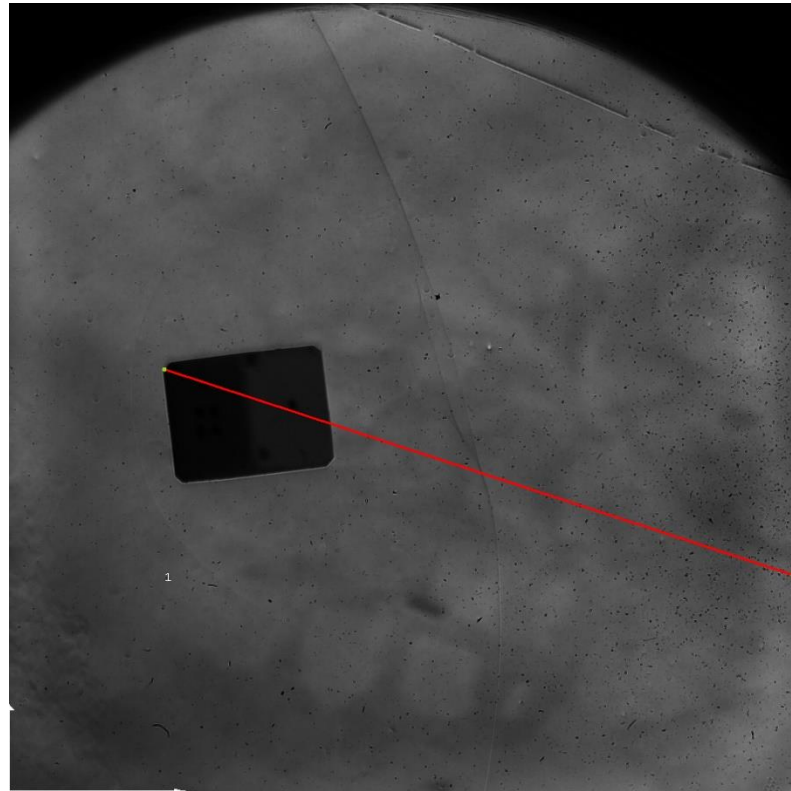


Figure 4.33: Start of Linear Trajectory Path of the Final Test for Drag Coefficient.

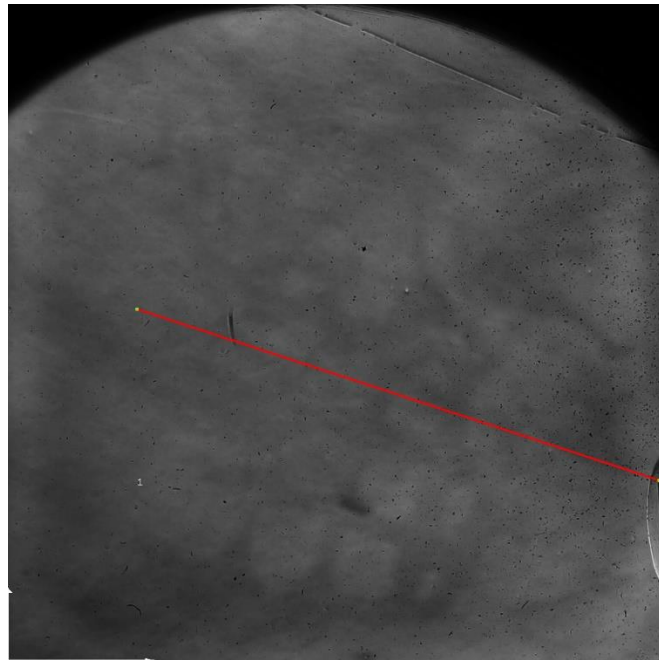


Figure 4.34: End of Linear Trajectory Path of the Final Test for Drag Coefficient.

From the information contained in Figs. 4.33 and 4.34;

$$t_{Total} = 0.15640625 \text{ sec}$$

$$\text{No. of frames after rupture} = 325$$

$$\text{Percentage of the No. of frames} = \frac{325}{1001} = 0.3246753247$$

$$t_{duration} = 0.15640625 \times 0.3246753247 = 0.05078125 \text{ sec}$$

$$d_{Travel} \approx 141.449 \text{ mm} \approx 0.141449 \text{ m}$$

$$\rho v^2 \approx 31.8 \text{ kPa}$$

$$A = 0.0253 \times 0.0251 = 0.00063503 \text{ m}^2$$

$$m = 0.122g$$

Calculating the acceleration of the test object:

$$d = ut + \frac{1}{2}at^2 \quad (4.3)$$

$$d_{Travel} = \frac{1}{2}at^2$$

$$a = \frac{2d_{Travel}}{t_{duration}^2}$$

$$a = \frac{2 \times 0.141449}{0.05078125^2}$$

$$a = 109.7041617 \text{ m/s}^2$$

Therefore, the acceleration of the cube is 109.7041617 m/s².

Calculating the drag coefficient:

$$F_{Drag} = \frac{C_D \rho v^2 A}{2} \quad (4.4)$$

$$C_D = \frac{2F_{Drag}}{\rho u^2 A}$$

$$C_D = \frac{2ma}{\rho u^2 A}$$

$$C_D = \frac{2 \times 0.122 \times 109.7041617}{31.8 \times 10^3 \times 0.00063503}$$

$$C_D = 1.325536121 \approx 1.33$$

Therefore, the drag coefficient is approximately 1.33.

Calculating error percentage:

$$\text{Error Percentage} = \frac{\text{Experimental} - \text{Theoretical}}{\text{Theoretical}} \times 100 \quad (4.5)$$

$$\text{Error Percentage} = \frac{1.33 - 1.05}{1.05} \times 100$$

$$\text{Error Percentage} \approx 26.67$$

Therefore, the calculated drag coefficient is approximately 1.33. When compared to the known coefficient of drag value for a cube, there is a percentage error of approximately 26.67 percent.

Calculating the general conditions within the experiment test area from the isentropic relationship:

Calculating the temperature from the isentropic relationship:

Assume:

$$k = 1.4$$

$$M = 5.9$$

$$T_o = 560 K$$

$$\frac{T_o}{T} = 1 + \frac{k-1}{2} M^2 \quad (4.6)$$

$$T = \frac{T_o}{1 + \frac{k-1}{2} M^2}$$

$$T = \frac{560}{1 + \frac{1.4-1}{2} \times 5.9^2}$$

$$T = 70.33408691 K \approx 70.33 K$$

Therefore, the temperature of the test section is approximately 70.33 K

Calculating the pressure from the isentropic relationship:

Assume:

$$k = 1.4$$

$$M = 5.9$$

$$P_o = 1.1 \times 10^6 Pa$$

$$\frac{P_o}{P} = \left(1 + \frac{k-1}{2} M^2\right)^{\frac{k}{k-1}} \quad (4.7)$$

$$P = \frac{P_o}{\left(1 + \frac{k-1}{2} M^2\right)^{\frac{k}{k-1}}}$$

$$P = \frac{1.1 \times 10^6}{\left(1 + \frac{1.4-1}{2} \times 5.9^2\right)^{\frac{1.4}{1.4-1}}}$$

$$P = 772.3516502 \text{ Pa} \approx 772.35 \text{ Pa}$$

Therefore, the pressure of the test section is approximately 772.35 Pa.

Calculating the density from the isentropic relationship:

$$k = 1.4$$

$$M = 5.9$$

$$P = \rho v^2 \quad (4.8)$$

$$\rho = \frac{P}{v^2}$$

$$\rho = \frac{3500}{(5.9 \times 343)^2}$$

$$\rho = 0.00085462537$$

$$\frac{\rho_o}{\rho} = \left(1 + \frac{k-1}{2} M^2\right)^{\frac{1}{k-1}} \quad (4.9)$$

$$\rho = \frac{\rho_o}{\left(1 + \frac{k-1}{2} M^2\right)^{\frac{1}{k-1}}}$$

$$\rho = \frac{0.00085462537}{\left(1 + \frac{1.4 - 1}{2} \times 5.9^2\right)^{\frac{1}{1.4-1}}}$$

$$\rho = 0.00000477771 \approx 0.0000048 \text{ kg/m}^3$$

Therefore, the density of the test section is approximately 0.0000048 kg/m^3 .

Furthermore, Tables 4.3 to 4.6 outlines the test object's velocity profiles and traveling distance throughout the final test. Tables 4.3 and 4.4 outlines these changes at the top left corner of the test object for each respective selected frame range as the object changes from one edge to the next edge and from one side face to the next side face, respectively. Table 4.5 and 4.6 outlines these changes at the centre of the test object for each respective selected frame range as the object changes from one edge to the next side face and from one side face to the next edge, respectively.

Frame Number	Distance Travelled (mm)	Velocity (m/s)	Change in velocity (m/s)
652-665	2.84662	1401.41	N/A
693-704	3.5597	2071.1	669.69
719-734	6.60424	2817.81	746.71
747-759	5.80907	3098.17	280.36
774-788	7.91692	3619.16	520.99
801-814	8.41152	4141.05	521.89
827-840	9.56562	4709.23	568.18
854-867	10.0805	4962.71	253.48

Table 4.3: Velocity Profiles and Traveling Distance from the edge of the cube to the next edge with respect to its Top Left Corner.

Frame Number	Distance Travelled (mm)	Velocity (m/s)	Change in Velocity (m/s)
659-672	3.3344	1641.8	N/A
686-699	3.79628	1868.94	227.14
712-726	5.97293	2730.48	861.54
739-753	6.1013	3003.72	273.24
767-780	7.44976	3667.57	663.85
794-807	9.2344	4546.17	878.6
820-834	9.8995	4873.6	327.43
847-861	10.4096	4758.68	-114.92

Table 4.4: Velocity Profiles and Traveling Distance from one side of the cube to the next side with respect to its Top Left Corner.

Frame Number	Distance Travelled (mm)	Velocity (m/s)	Change in Velocity (m/s)
720-726	3.96103	4225	N/A
747-753	6.596	7035.73	2810.73
773-780	4.6172	4925.01	-2110.72
801-780	5.12253	6556.84	1631.83
827-834	5.79266	5296.15	-1260.69

Table 4.5: Velocity Profiles and Traveling Distance from the edge of the cube to the side with respect to its centre.

Frame Number	Distance Travelled (mm)	Velocity (m/s)	Change in Velocity (m/s)
739-747	4.94975	3959	N/A
766-774	7.25747	5805.98	1846.98
793-801	7.25747	5805.98	0
820-827	4.66408	4264.3	-1541.68
847-855	9.23587	7388.7	3124.4

Table 4.6: Velocity Profiles and Traveling Distance from the side of the cube to the edge with respect to its centre.

4.4 Discussion

After examining the collected and calculated data for both the Preliminary/bench test and the final experiment test the following key findings were determined. The preliminary/bench test results revealed that the determined RPM of the apparatus from both of the tachometer and the calculated data from the recorded videos followed a linear trend. However, when comparing the data obtained from the tachometer and the calculated RPM for the loaded test, there was a significant difference between these values for the first reading with a calculated percentage error reading of 43.4286 percent. However, this did decrease to a maximum of 13.78947 percent, when analysing the other readings. In regards to the final test, the test object followed a predictable/expected trajectory (as displayed in Fig. 4.31) and the fluid's flow characteristics also followed the expected typical flow conditions of the wind tunnel.

In addition, the final calculations revealed that the approximate RPM, acceleration and drag coefficient of the test object are 6975.22, 109.7 m/s^2 and 1.33, respectively. When comparing the RPM and drag coefficient values back to preliminary/bench test data and the theoretical value, there was a percentage error of approximately 52.19 and 26.67, respectively. In regards to the coefficient of drag value, this error could be contributed to the increase surface area between the fluid's flow and the surface face or edge of the test object, as the object continues to change its angle of attack as seen in Appendix F.1. With regards to the error present with the RPM, this could be contributed to the increase voltage supplied to the motor and speed controller. However, these errors could also be contributed by the accuracy of the dimensions of the test object, the positioning of the test object with respect to the centre of gravity of the apparatus, the interference from the separation of the test platform and the test object and the effect from the vibration from the DC motor. Furthermore, the results displayed in Tables 4.3 and 4.4 reveals that when examining the rotational changes to the next edge or side face, the velocity and distance travelled by the test object increases as time progresses to a point where the object's velocity begins to decrease. However, when analysing the changes from the edge to the side face of the cube and the side face of the cube to the edge, the velocity constantly changes. In addition, from the isentropic relationship of the fluid's flow, the calculated temperature, pressure and density of the flow are approximately 70.33 K, 772.35 Pa and 0.0000048 kg/m^3 , respectively.

4.5 Summary

In summary, this chapter presents the results from both the preliminary/bench tests and the final test of the test object. In addition, this chapter also outlines the components and equipment used throughout both the preliminary/bench test and final test of the object and presents images/snapshots or selected frames capture by the highspeed camera. Additionally, this chapter also calculates and determines the operating conditions of the fluid's flow and the test object's experienced forces. Furthermore, this chapter also discusses and outlines the main findings from the results and also performs an error analysis on the results.

5 Conclusion and Recommendation

5.1 Introduction

Within this chapter, the conclusions and recommendations will summarise the previous four chapters including the main results and key findings of this research project. In addition, this chapter will also outline and discuss any recommendations that could be utilised for this research project and any other future research projects that are related to or expands on from this research project.

5.2 Conclusion

In conclusion, as humanity continues to strive for technological and scientific knowledge and understanding, there will always be problems that arise, these are either known at the time of the discovery or development, or once a problem has been identified and acknowledged through research sometime in the future. This is evident from this research project, whereas society continues to grow and expand its knowledge and understanding of the universe in pursuit of technological advancements. However, as stated in the previous chapters, the following problem has arisen; the risks and hazards associated with the continuous launching of manmade objects such as satellites and spacecrafts into Earth's orbit. The main hazard and risk that this research project identifies and closes the knowledge gap on is monitoring, tracking and deorbiting of old spacecraft and debris due to past manned and unmanned projects/missions. In addition, after conducting a comprehensive literature review, the majority of the research that has been conducted within this field of hypersonic fluid flow and object/vehicle re-entry has involved using numerical and computational simulation. While only one of the examined research articles considered the effect of tumbling objects. Therefore, this research project identified a gap in the knowledge, this was further research and experimentation is still required, in regards to re-entry and the effect of freefalling tumbling objects.

Therefore, as previously stated, the main aim of this research project is to design an apparatus that can artificially simulate and examine the re-entry trajectory of an object tumbling at high speed during freefall from orbit within a hypersonic wind tunnel. In order to achieve the main aim, the following objects will need to be achieved;

1. Review previous academic research and background information on objects re-entering the earth's atmosphere, this includes re-entry and object trajectory calculations and hypersonic fluid flows.
2. Review and examine the design restrictions and limitations of the prototype with the wind tunnel.
3. Design and construct a prototype and a model that can perform the experiment within the wind tunnels.
4. Perform the experiment and capture/collect all data relating to the project.
5. Consolidate and examine the captured/collected data.
6. Provide recommendations on the design of the experiment and future experiments.

Furthermore, this research project intendeds to benefit the scientific community and the future of the space industry. These benefits include;

- The ability to establish a procedure and the technology that could be used to successfully deorbit the objects and track complex trajectories,
- The ability to track and predict the trajectories of unplanned/unexpected freefalling tumbling objects,
- Decrease the risk of damage to structures and injures to the animals, environment and to human life on Earth,
- Promote future research and innovation within the engineering, technology and science fields,
- Provide future investment opportunities for research and innovation in a variety of fields, and
- Contribute to the overall success of private companies and government organisations and institutions.

As previously stated, this research project was conducted within the TUSQ facility located at USQ campus in Toowoomba, Queensland. Before the design stage of the research project could commence, the limitations of the hypersonic wind tunnel and the release mechanism needed to be outlined and established. These limitations that are outlined in Tables 3.1, 3.2, and 3.43.5 were utilised in the theoretical calculations and the design of the apparatus displayed in Tables 3.5, 3.6, and 3.7. Furthermore, in order to complete this project, this project underwent four stages of testing; the freefall test, the performance test, the preliminary/bench test at the TUSQ facility, and the final test within the hypersonic wind tunnel.

Additionally, there were three design options that were identified, however, by using a decision matrix, the matrix identified that option two was the ideal design for this research project. This option

comprised of the following equipment; two nine-volt battery holder with the required battery nine-volt batteries in parallel, a six-volt motor rated to produce 9 000 RPM, the apparatus including; the testing platform, the motor housing unit, the stabilising platform, two 3mm bolts and nuts, the pre-fabricated release mechanism and a PWM motor speed controller with digital display and start button. Furthermore, in order to prove that option two was the ideal design, the design would undergo two performance tests before being tested in the hypersonic wind tunnel. These were the performance test and the preliminary/bench test at the TUSQ facility.

From the design limitations of the release mechanism, the apparatus was limited to the dimensions of the release apparatus and was required to be secured by two 3mm bolts and nuts. Furthermore, by utilising the hypersonic wind tunnel's normal operating conditions, the theoretical mass, drag force, frictional force and the force applied to the test objects could be calculated. Initially, four objects were going to be simulated and examined, however, due to time restraints, only one object was tested within the TUSQ facility.

After conducting the test of the test object (cube) within the TUSQ facility and analysing the collected data, the results revealed the following; the calculated RPM and the drag coefficient of the test object and the temperature, pressure and density of the flow were approximately 6975.22, 1.33, 70.33 K, 772.35 Pa and 0.0000048 kg/m³, respectively. Additionally, when comparing the RPM and drag coefficient back to the data used in the design stage of the research project, there was a calculated percentage error approximately 52.19, and 26.67, respectively. This could be contributed to the errors from the test. In addition, the trajectory of the test object was able to be obtained and is outlined in Figs. 4.31 and 4.32. Furthermore, the change in velocity as the test object rotated from the edge of the test object to the side face of the object was also obtained, these are displayed in Tables 4.3 to 4.6. The data revealed that the velocity of the test object continued to increase as time progressed until it reached the frame region of 847 to 861 this is approximately 0.132 to 0.135 sec. into the test.

Due to some errors that have occurred during the hypersonic wind tunnel test, the accuracy of the data may have affected the final results. These errors could be contributed by the following; the increase surface area that the fluid's flow has on the test object, as the object continues to change its angle of attack, the increase voltage supplied to the motor and speed controller, the accuracy of the dimensions of the test object, the positioning of the test object with respect to the centre of gravity of the apparatus, the interference from the separation of the test platform and the test object and the effect from the vibration from the DC motor. However, the main aim of this research project was achieved, but only one test object was tested and the final test object and data did not involve the investigation and examination of the effect of adding an object that would create a shockwave for the freefalling object to interact with.

5.3 Recommendations

The following section will be broken up into two sections. The first section will outline recommendations in regards to this research project and the second section will outline recommendations for any future projects that continue on from this particular research project or any research project related or relevant to the research area of hypersonic flow during freefall.

5.3.1 Recommendations Related to this Research Project

After conducting this research project and analysing the results gathered from the final test of the test object (the cube) from the TUSQ facility, there are variety of recommendations that can be utilised within this research project. These recommendations include the following;

- Incorporate a wide variety of test objects, sizes and different ratios, these include but are not limited to the following; square based pyramid, triangular pyramid, triangular prism, and a cone. By incorporating a variety of shapes, sizes and different ratios it will provide an opportunity to examine the effect of different shapes as they re-enter the Earth's atmosphere.
- Modify and improve the apparatus used for this research project. These modifications and improvements can include but are not limited to the following; change the material used for the apparatus that is designed to minimise and dissipate the vibration from the motor, modify the design of the apparatus to minimise and dissipate the vibration from the motor and design and manufacture a release mechanism that decreases the vibration from the motor.
- Increase the RPM of the test object. This will provide an accurate simulation of a freefalling tumbling object re-entering the Earth's atmosphere.
- Improve the method for which the test object is manufacture to improve the dimensional accuracy of the test object. This will improve the overall results obtained from the experiment.
- Incorporate a different method for obtaining and measuring the RPM of the test object. This can be achieved by incorporating sensors such as hall effect sensors.
- Incorporate a different controlling method for controlling the motor. This will increase the accuracy of the data and this can be achieved by using microcontrollers.
- Change the motor that was used with a more reliable and durable motor that can minimise the vibrational effect from the motor and improve the RPM speed transferred to the test object.

This will provide an accurate simulation of a freefalling tumbling object re-entering the Earth's atmosphere.

- Improve the design of the separation of test object from the test platform. This will minimise any error that are present in the recording.

5.3.3 Future Work and Experimental Recommendations

After conducting this research project and analysing the results gathered from the final test of the test object (the cube) from the TUSQ facility, there are variety of recommendations that can be utilised for any future research projects or that continues on from this particular research project or any research project related or relevant to the research area of hypersonic flow during freefall. These recommendations include the following;

- Increase the fluid's flow speed within the test section of the TUSQ facility. By increasing the speed of the fluid's flow, it will enable the test facility to provide a more accurate simulation and results that are observed during debris re-entering the Earth's atmosphere.
- Add the addition of multiple test objects freefalling within the same test area. This will provide an opportunity to examine and simulate the effect of multiple debris re-entering the atmosphere and how they may interact with one another during freefall.
- Add the addition of a platform that creates a shockwave and position the test object above the platform of which when the test object is released, it enters the shock wave. This will help simulate the effect of objects crossing paths of other objects that have re-entered the Earth's atmosphere.
- Design an apparatus that can simulate the test object for which the test objects are tumbling on all degrees of freedom.
- Design a system that improves the separation of the test objects from the apparatus. This will minimise any error from occurring.

5.4 Summary

In summary, this chapter summarises the previous four chapters; the Introduction, Literature Review, Methodology and the Results and Discussion including the main aim and objective, and the main results and key findings. Furthermore, this chapter also summarises and outlines the recommendations for this research project and any future research project relevant to or expands from this research project.

Appendix

Appendix A – Project Specification

ENG4111/4112 Research Project

Project Specification

For: Gregory Hartmann

Title: Examining the Re-entry of a Tumbling Object During Freefall

Major: Mechanical Engineering

Supervisors: Professor David Buttsworth

Enrolment: ENG4111 - EXT S1, 2021

ENG4112 - EXT S2, 2021

Project Aim: To design and artificially simulate and examine the re-entry trajectory of an object rotating at high speed during freefall from orbit within a wind tunnel.

Programme: Version 2, 31st July 2021

1. Review previous academic research and background information on objects re-entering the earth's atmosphere, this includes re-entry and object trajectory calculations and hypersonic fluid flows.
2. Review and examine the design strictions and limitations of the prototype with the wind tunnel.
3. Design and construct a prototype and a model that can perform the experiment within the wind tunnels.
4. Perform the experiment and capture/collect all data relating to the project.
5. Consolidate and examine the captured/collected data.
6. Provide recommendations on the design of the experiment and future.

If there is time available:

7. Design and construct an object to create a supersonic shock wave.
8. Reperform experiment with the supersonic shock wave.

Appendix B – Concept Designs

Appendix B outlines the concept designs of the apparatus that would be utilised during this project.

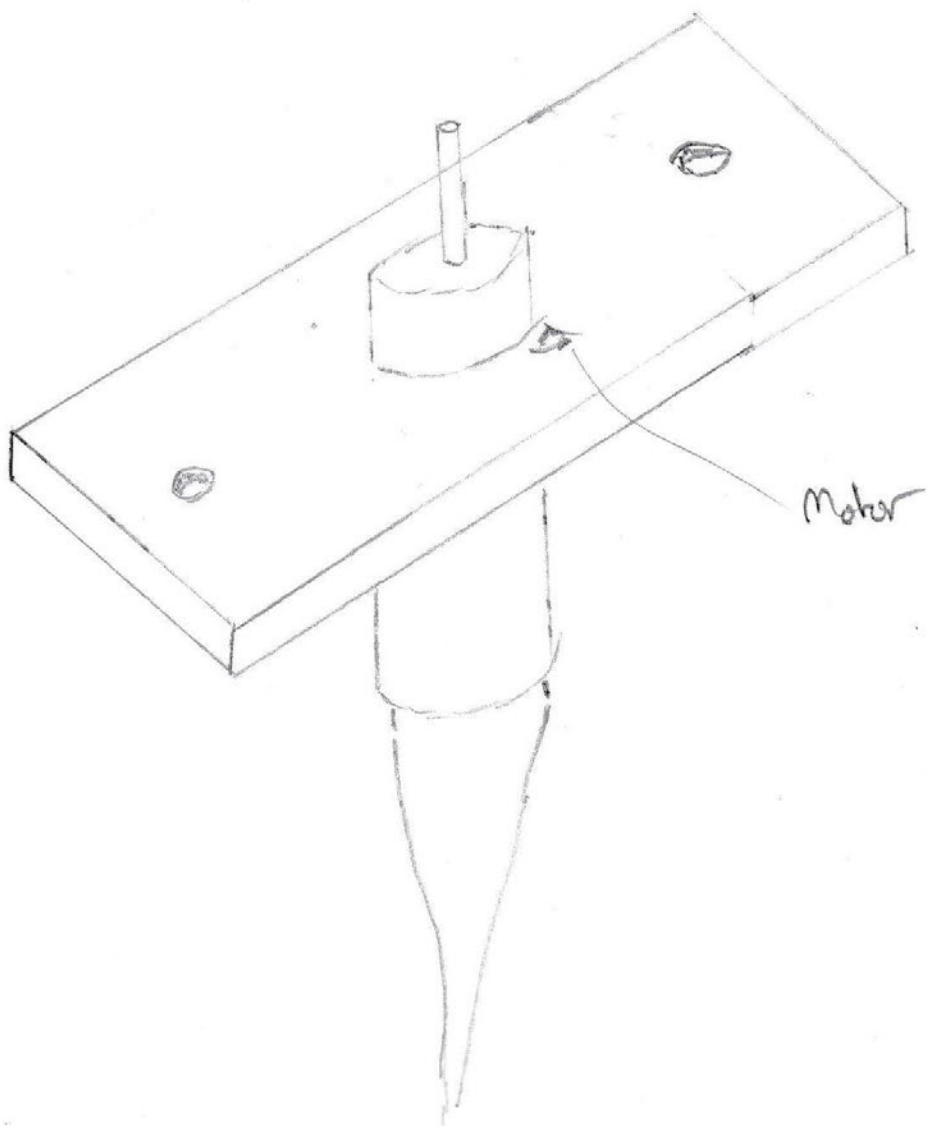


Figure B.1: Design Concept One (Not to Scale).

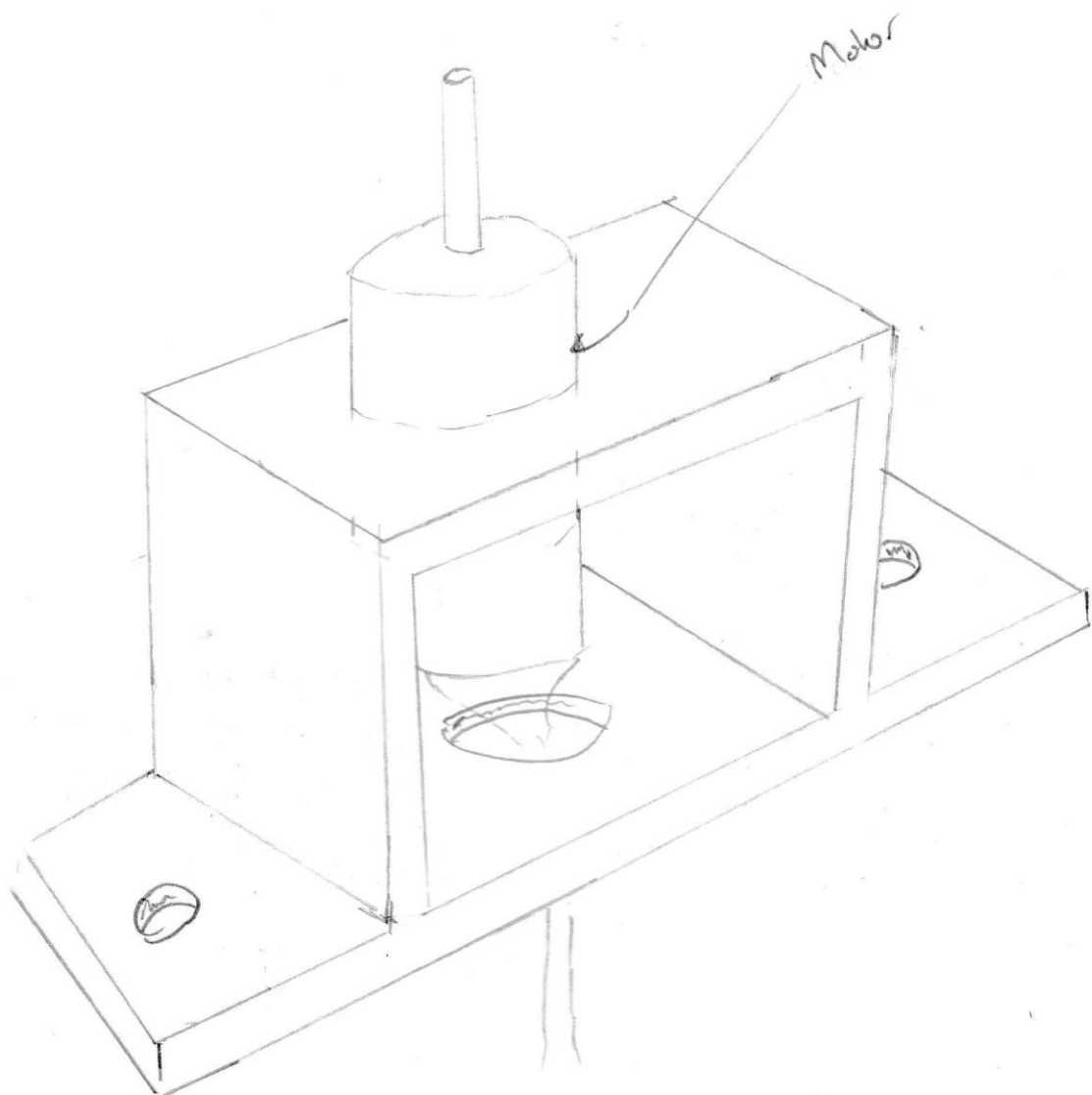


Figure B.2: Design Concept Two (Note to Scale).

Appendix C – Preliminary Methodology

Table C.1 outlines the procedure that will be used to successfully complete the objectives at each stage of this project.

Phase One		Research Proposal and Organisation
A1		Organise and prepare research proposal for the USQ to examine.
B1		Complete Project Specification Report. (Check and confirm equipment availability at USQ and complete any necessary forms required to use equipment).
Phase Two		Gathering Research
A2		Collect and review previous academic research
B2		Collect and review background information in hypersonic fluid flow
C2		Collect and review the design restrictions and limitations of the prototype
Phase Three		Prototype
A3		Design prototype
B3		Construct prototype
C3		Perform preliminary tests outside wind tunnel
Phase Four		Perform Experiment
A4		Perform experiment within wind tunnel
B4		Collect and consolidate data
C4		Modify and perform the experiment with a supersonic shock wave
Phase Five		Dissertation
A5		Complete dissertation draft.
B5		Attend and complete Engineering Professional Practice Two (ENG4903) requirements.
C5		Apply feedback from supervisors to the dissertation.
D5		Complete and submit final dissertation.

Table C.1: Breakdown of Project Plan.

Fig. C.1 uses the data within Table C.1 to graphically represent the project plan.

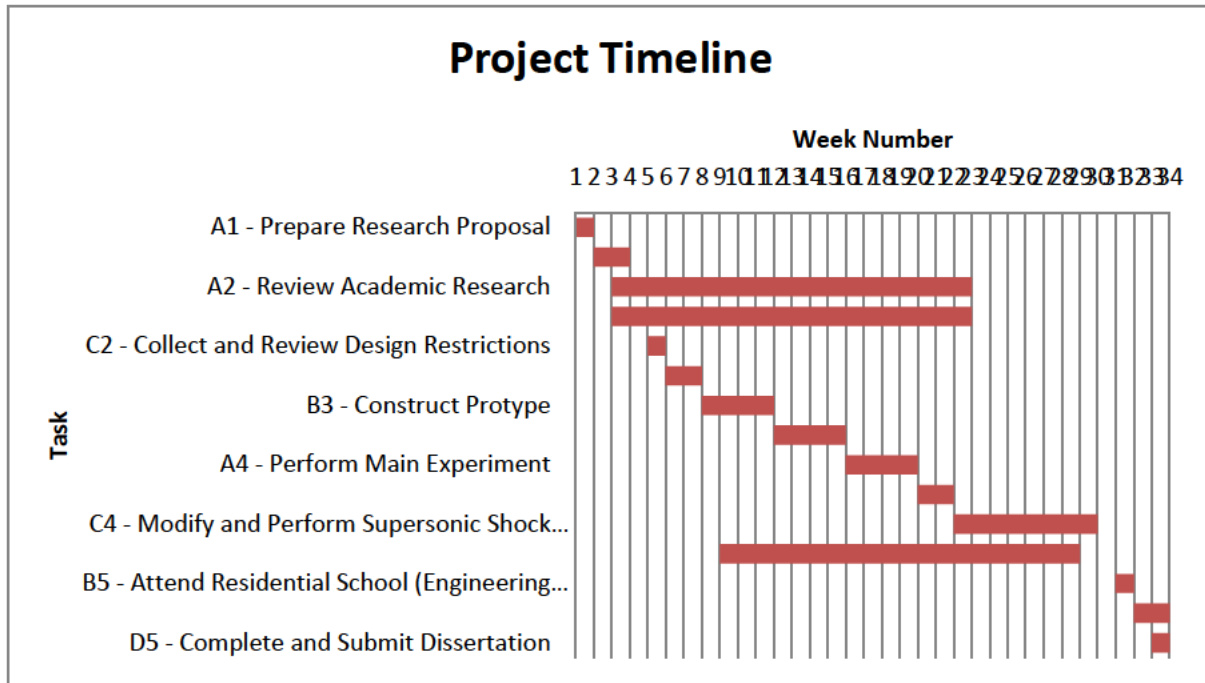


Figure C.1: Project Plan Outline.

Table C.2 outlines an in-depth procedure that will be utilised to conduct and successfully complete the objective of this project.

Stages of the Project's Design	Details
1	Determine design Restrictions
2	Design and draw preliminary prototype and identify required components
3	Construct preliminary prototypes
4	Conduct preliminary tests (Outside of wind tunnel)
5	Determine best preliminary prototype to be use for experiment
6	Construct experiment prototype
7	Determine different types of models to be used
8	Drawn and construct models
9	Perform stress analysis on models
10	Test each model at a selected velocity and rotational velocity

11	Analysis recorded data
12	Design, construct and test shockwave experiment

Table C.2: Preliminary Outline of Project's Design Stages.

Appendix C.1 Resource Planning

In order to fulfill all objectives and requirements of this project, the following resources will be utilised and required, as displayed in Table C.3.

Resources	Supplier/source	Cost
Computer with access to an internet connection	Student	Nil
A wind tunnel with related programs	USQ	Nil
Materials required to construct the model eg bolts and nuts	Student	To be calculated
Tools and machinery	Student and USQ	To be calculated
Solid modelling software in order to design the model	USQ	Nil
Computer software such as Microsoft Word and Excel	Student	Nil
High-speed Camera	USQ	To be calculated
3D Printer	USQ	To be calculated

Table C.3: Resources required for the project.

Appendix C.2 Preliminary Risk Assessment

While performing this project and any future research/projects related to this project, there are a variety of risks that can occur. These are presented in Table C.4.

Hazard	Causes	Consequences/likelihood	Risk	Minimisation Level
Personal Injuries from uses a computer (Research and designing stages)	Poor posture, fatigue, eyestrain	Rare/Minimal	Low	Take regular breaks. Use correct posture while using the computer. Perform stretch exercises prior, during and after each session.
Injuries from travelling to campus	Fatigue, moving vehicles, environmental conditions and surface damages	Rare/Minimal	Low	Take regular breaks. Perform maintenance on vehicle by certified and trained people.
Injuries from using tools or machinery	Fatigue, damage to equipment such as electrical and mechanical faults, not using the correct Personal Protective Equipment (PPE), environmental conditions, slip, trips and spills, and have not been trained to use the equipment and manual	Unlikely/moderate	Low	Use correct PPE, perform regular maintenance on the machinery and electrical equipment, check equipment before starting, and be certified

	handling.			to use the equipment
Injuries from using wind tunnel	Fatigue, damage to equipment such as electrical and mechanical faults, not using the correct Personal Protective Equipment (PPE), environmental conditions, slip, trips and spills, have not been trained to use the equipment and manual handling	Unlikely/moderate	Low	Use correct PPE, perform regular maintenance on the machinery and electrical equipment, check equipment before starting, and be certified to use the equipment

Table C.4: Risk Assessment of this Project and Future Projects

Appendix D – Apparatus Schematics

Appendix D outlines the apparatus schematics for each component that was utilised during this project.

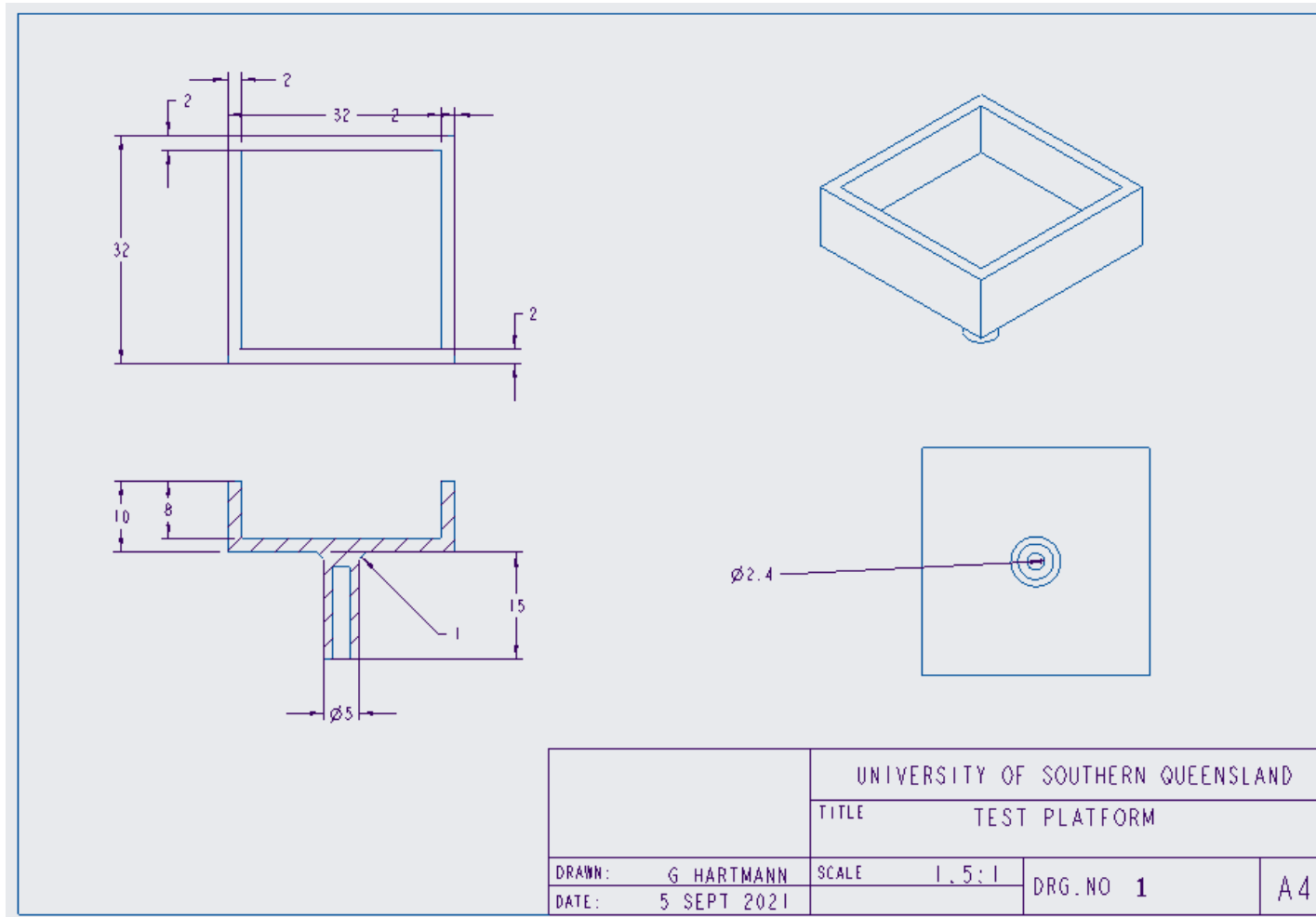


Figure D.1: Schematic of Test Object Platform.

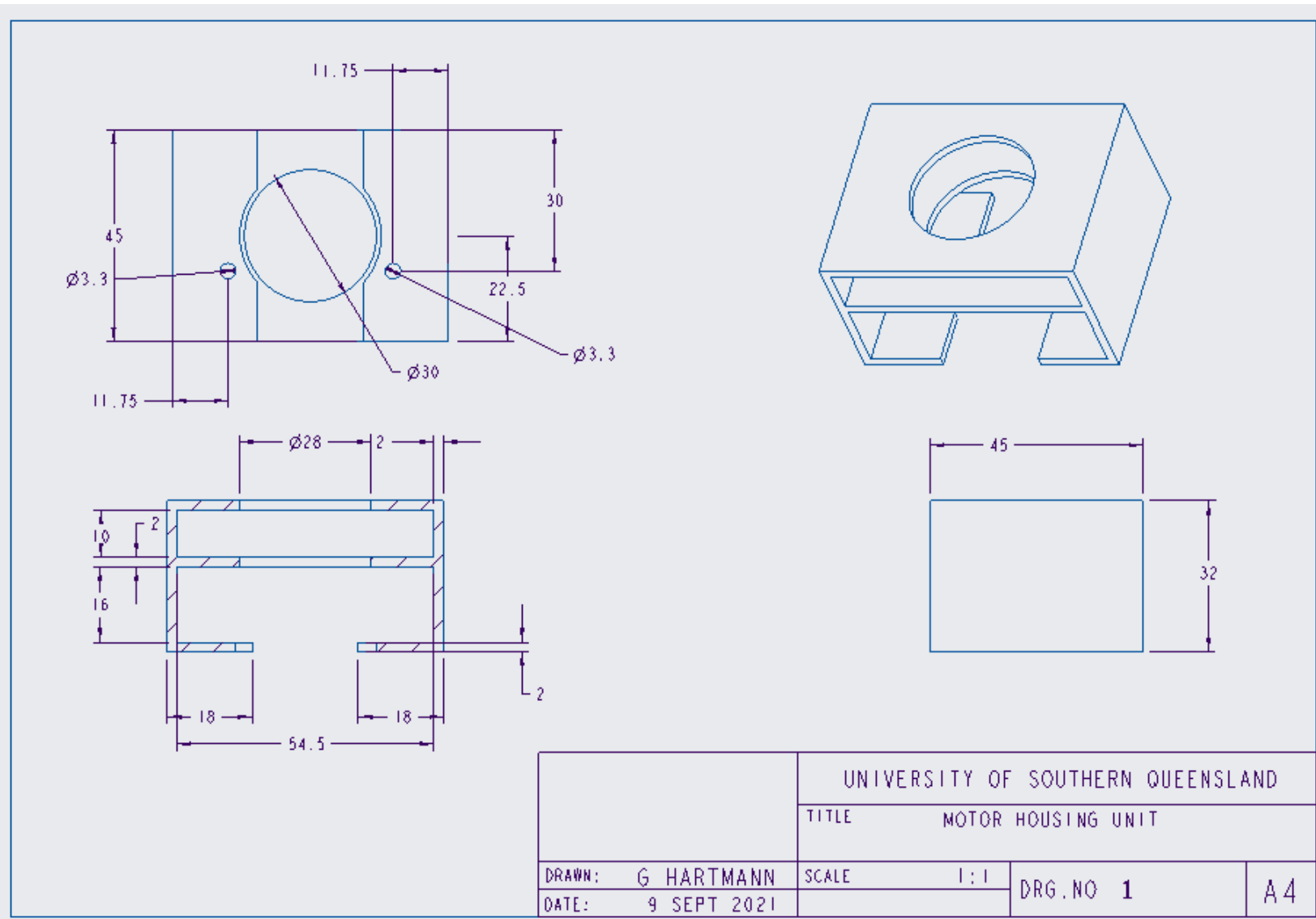


Figure D.2: Schematic of Motor Housing Unit.

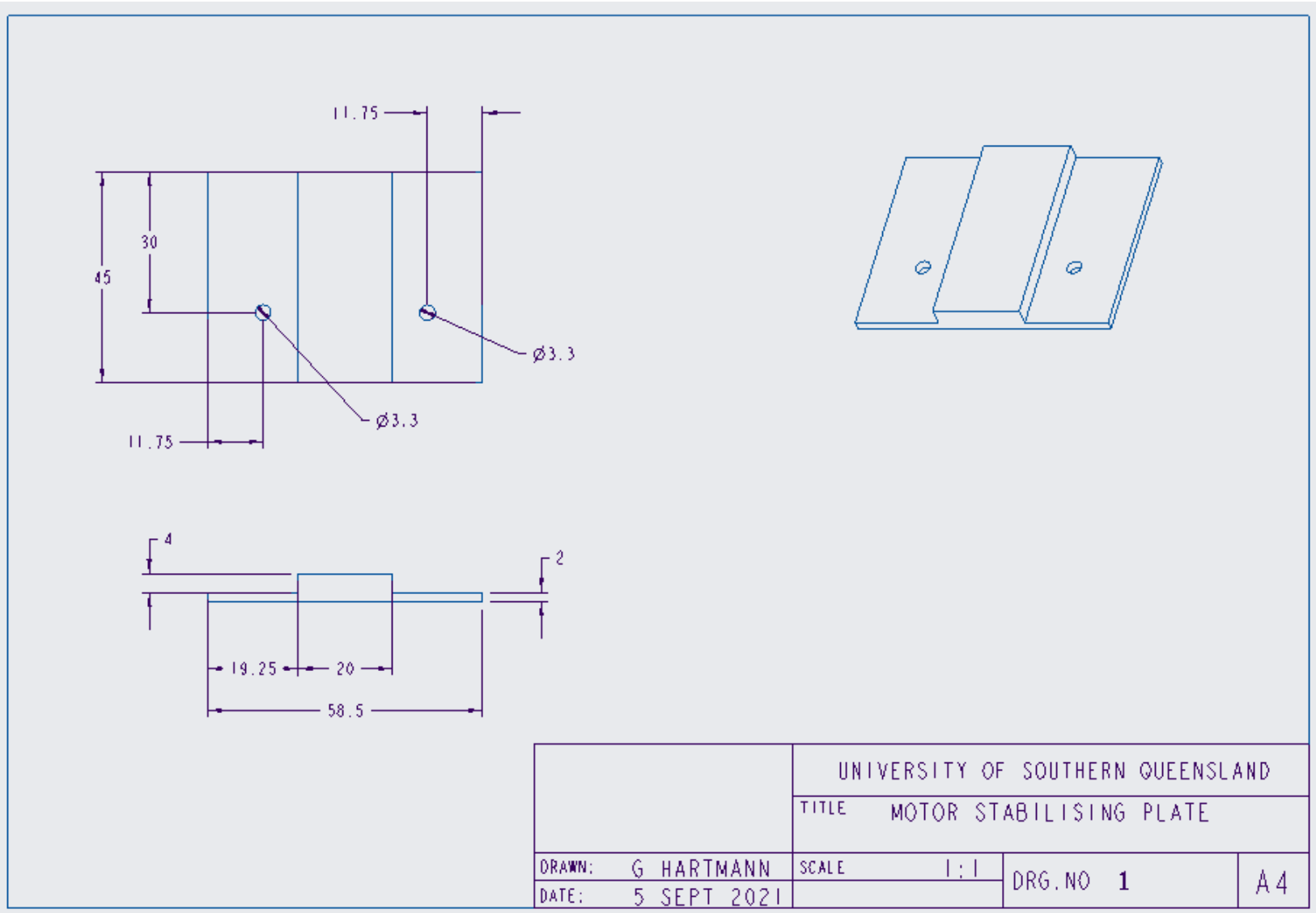


Figure D.3: Schematic of Motor Stabilising Plate.

Appendix E – Test Objects Schematics

Appendix E outlines the test objects schematics for the test objects that were utilised during this project.

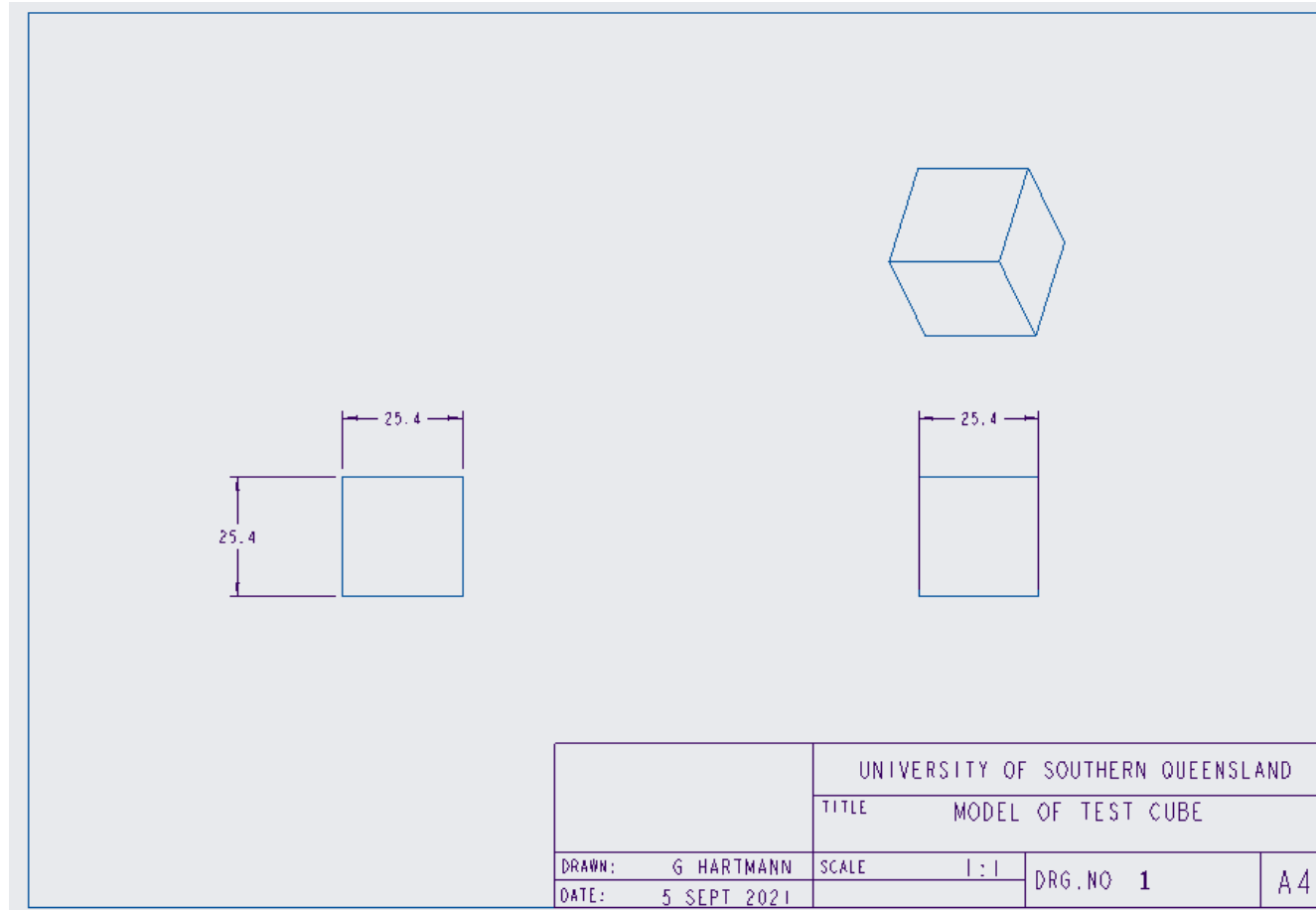


Figure E.1: Schematic of Test Object ‘Cube’.

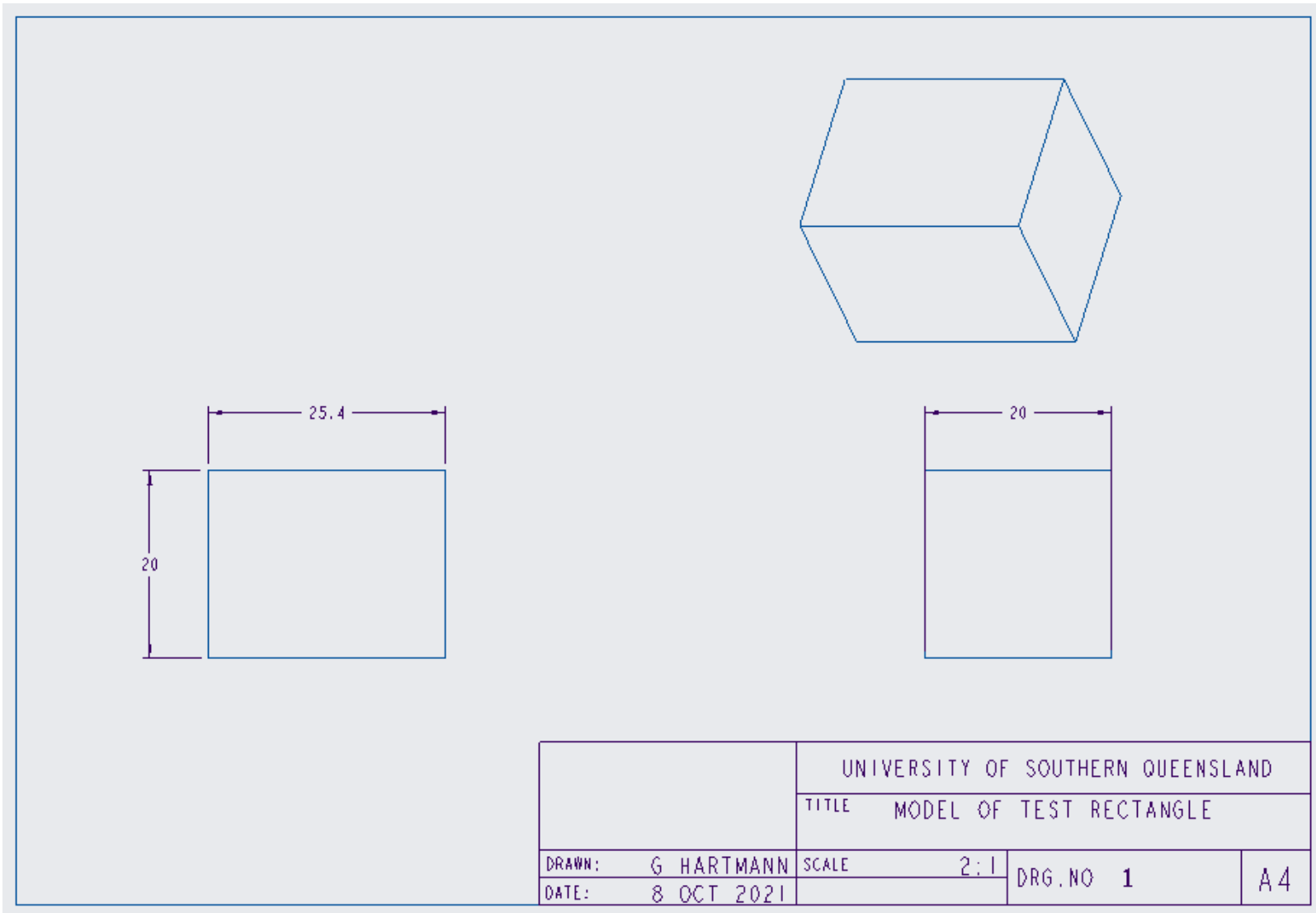


Figure E.2: Schematic of Test Object 'Rectangle'.

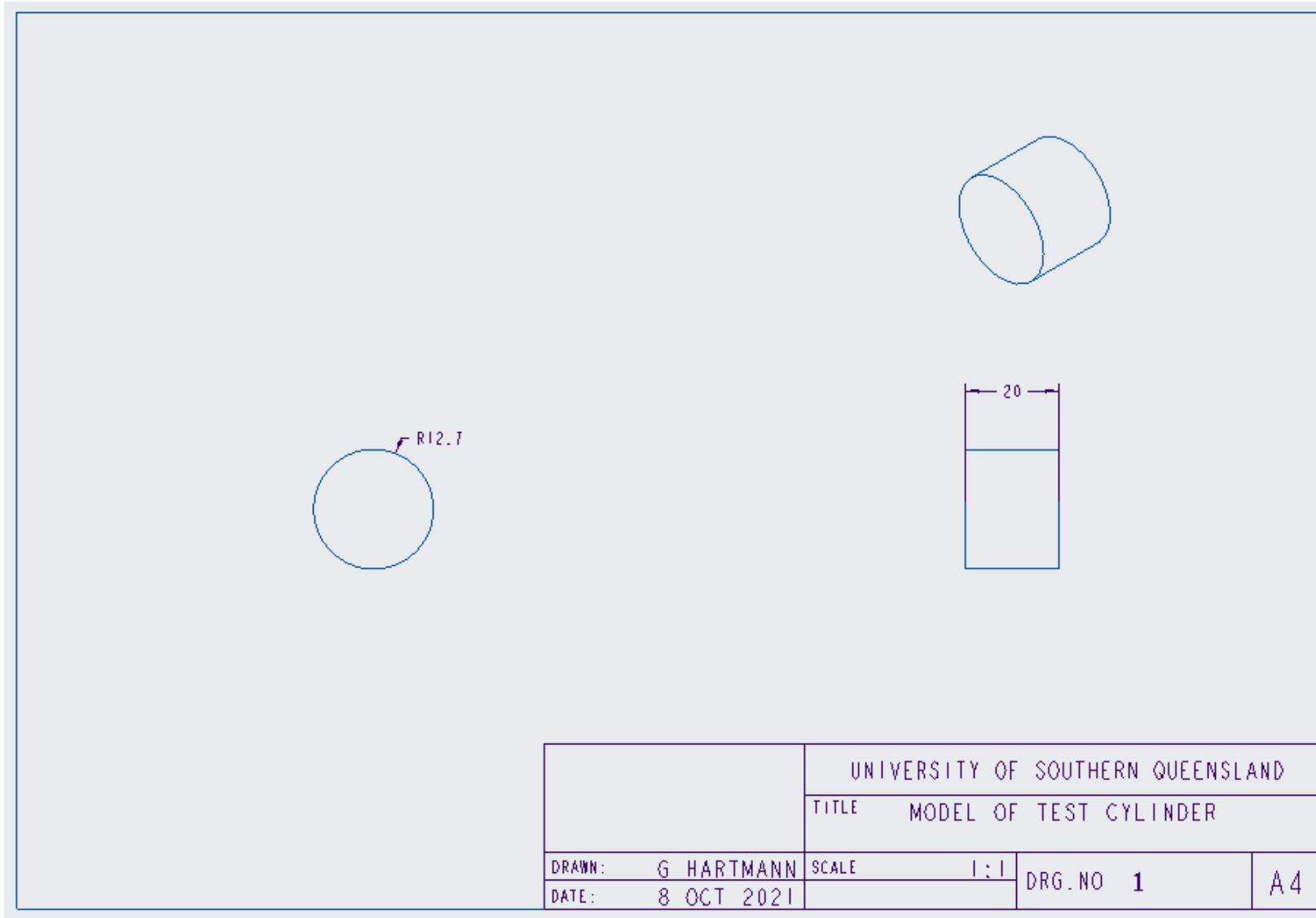


Figure E.3: Schematic of Test Object ‘Cylinder’.

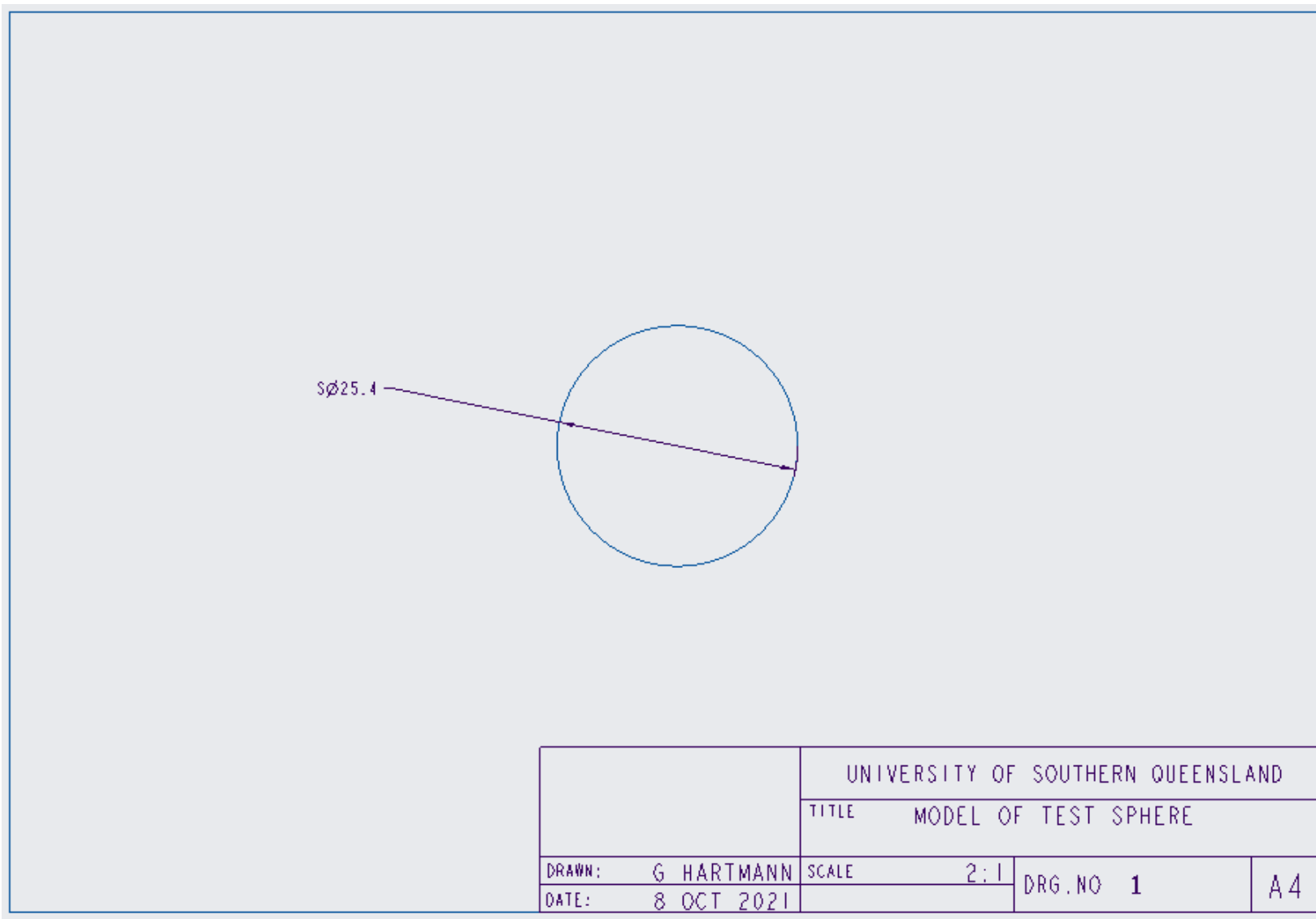


Figure E.4: Schematic of Test Object ‘Sphere’.

Appendix F Preliminary/Bench and Final Test Snapshot Breakdown

Appendix F outlines snapshots of the experiment setup for the final test within the TUSQ facility.



Figure F.1: Experiment Setup Side View.



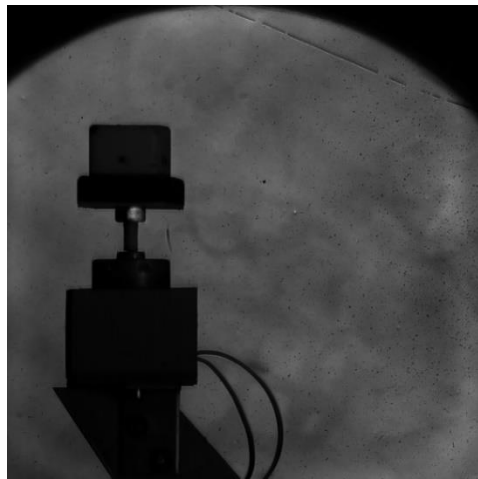
Figure F.2: Experiment Setup Rear View.



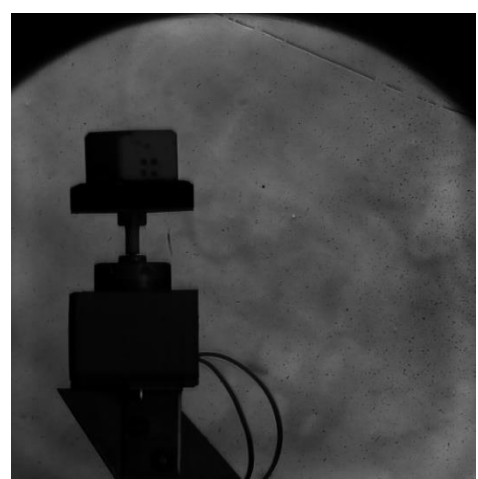
Figure F.3: Experiment Setup Side Close-Up View.

Furthermore, the following images or snapshots of the final and preliminary tests are outline below. These will be images will be grouped and labelled by each test.

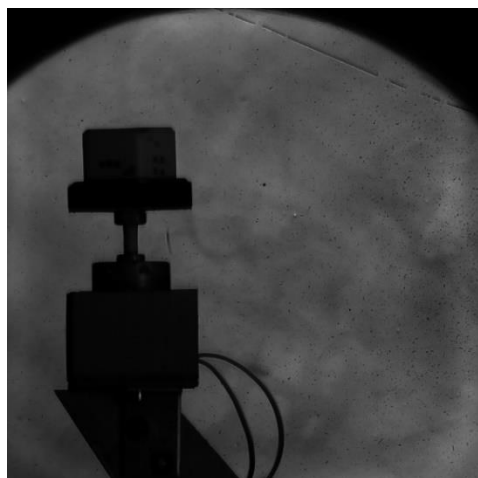
Appendix F.1 Final Test



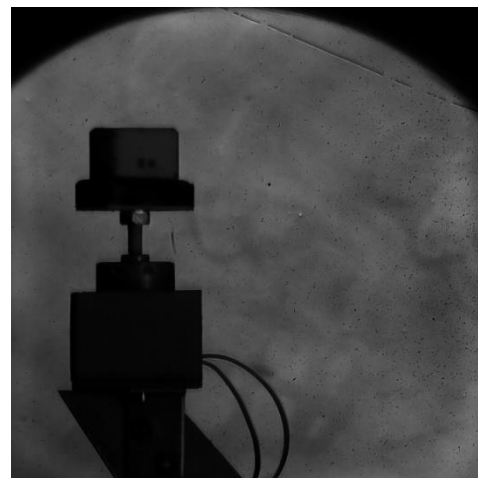
Frame 1



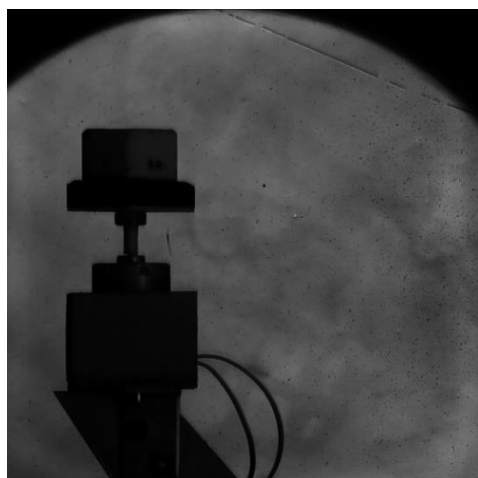
Frame 75



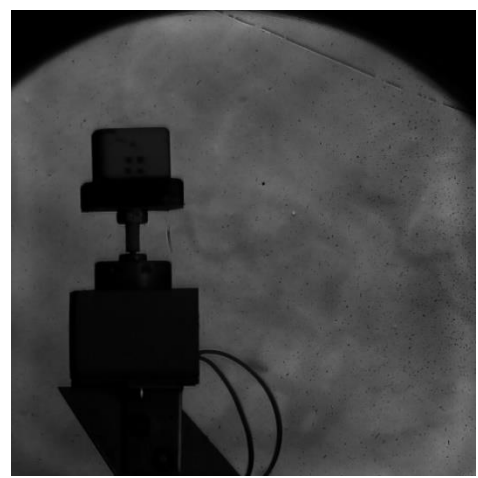
Frame 25



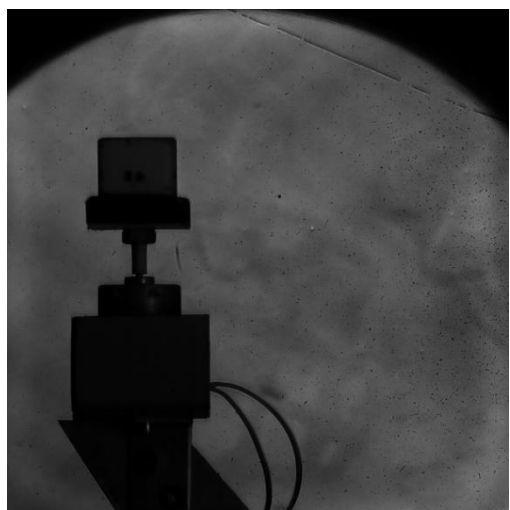
Frame 100



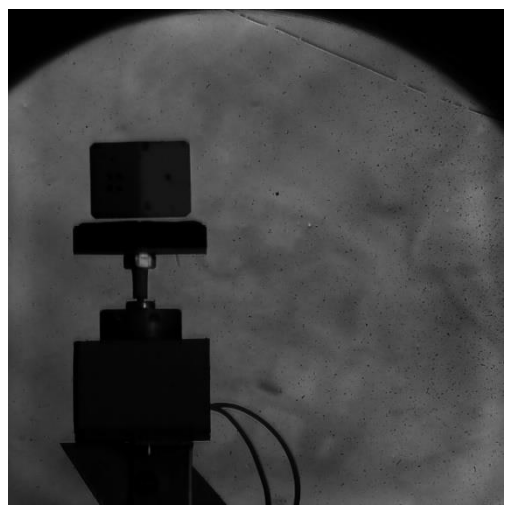
Frame 50



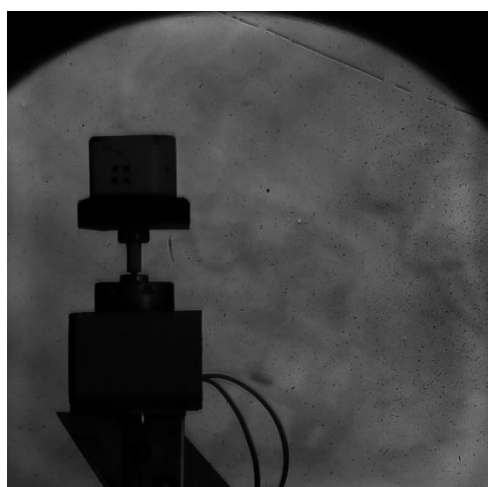
Frame 125



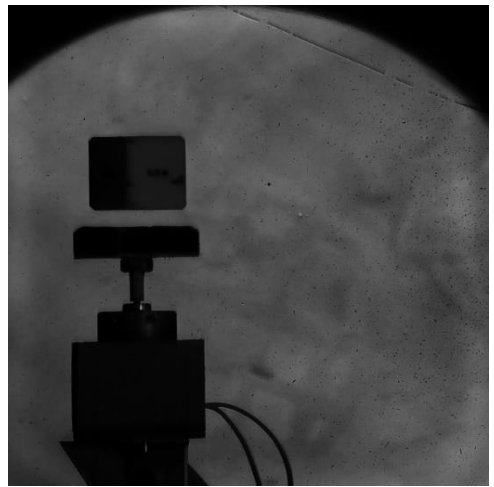
Frame 150



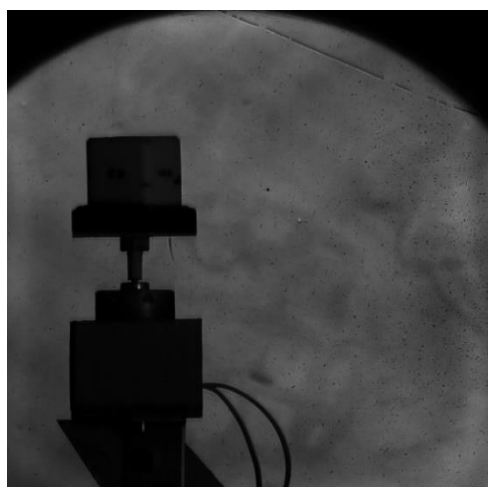
Frame 225



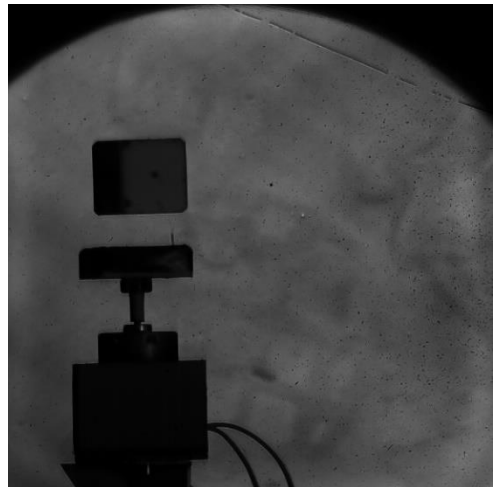
Frame 175



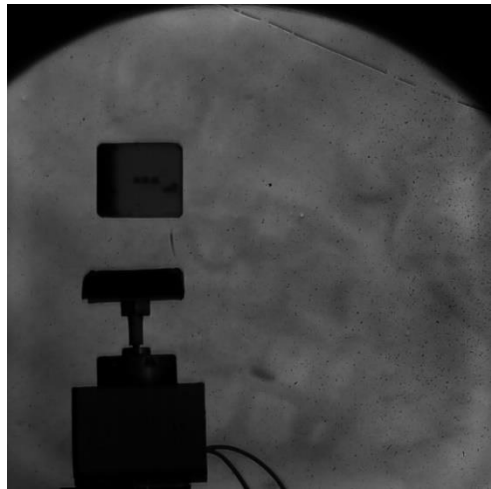
Frame 250



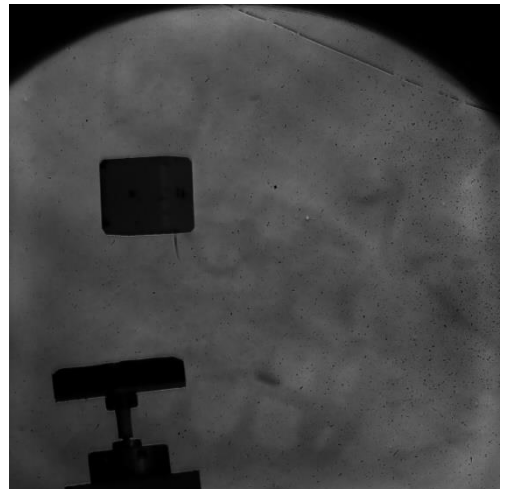
Frame 200



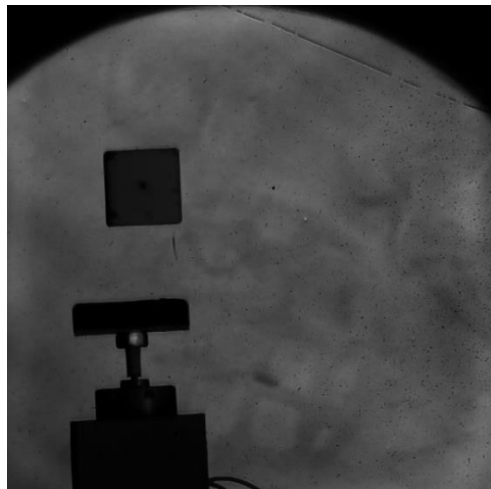
Frame 275



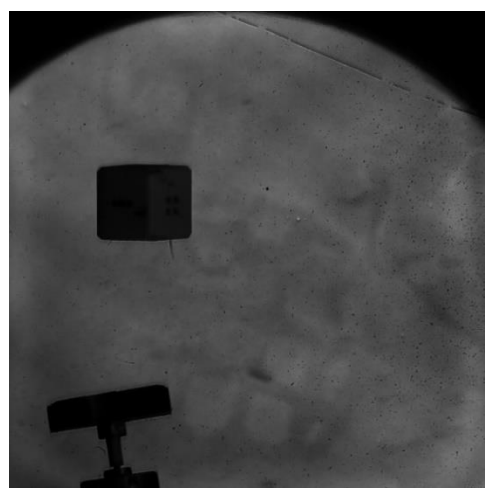
Frame 300



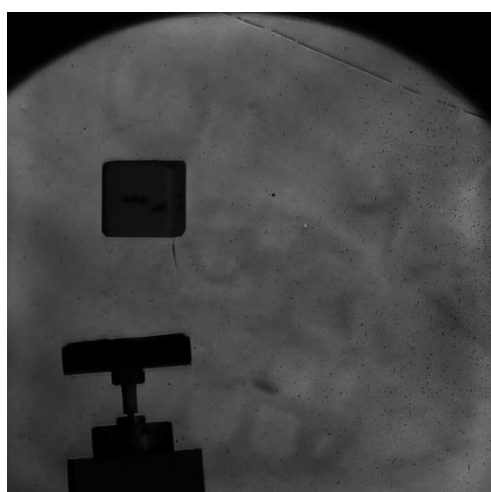
Frame 375



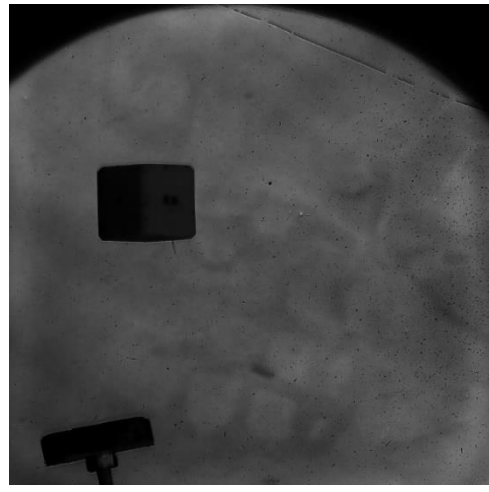
Frame 325



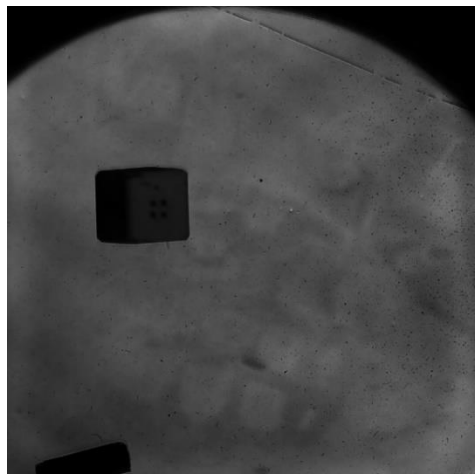
Frame 400



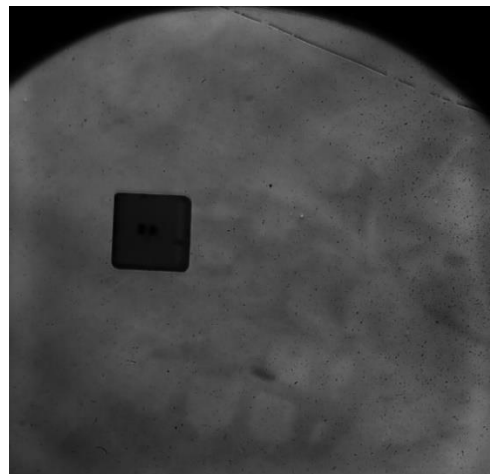
Frame 350



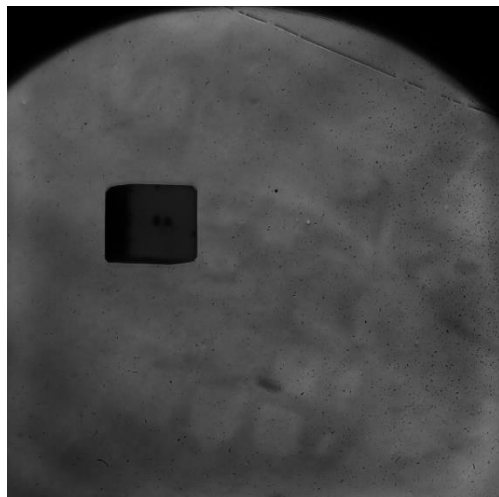
Frame 425



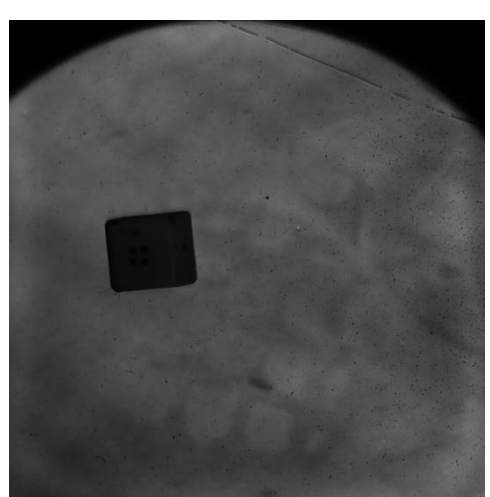
Frame 450



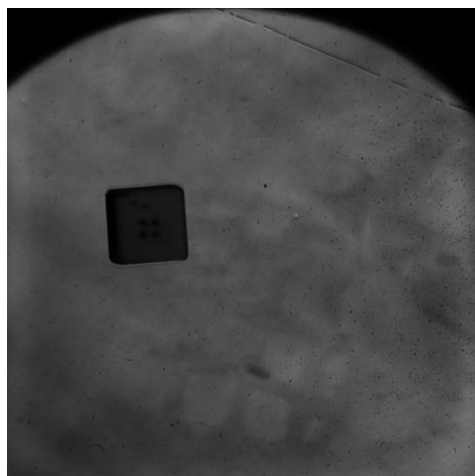
Frame 525



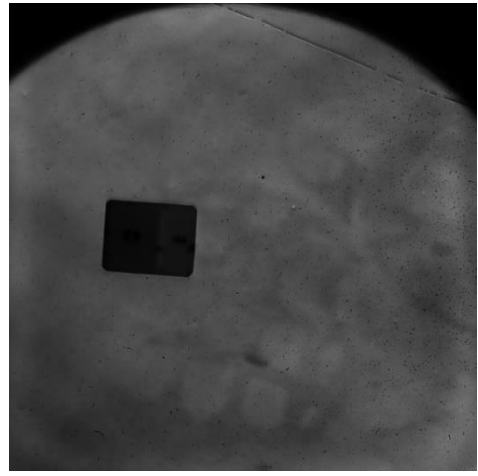
Frame 475



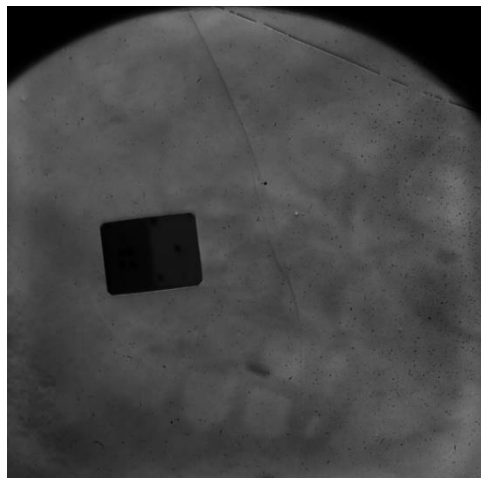
Frame 550



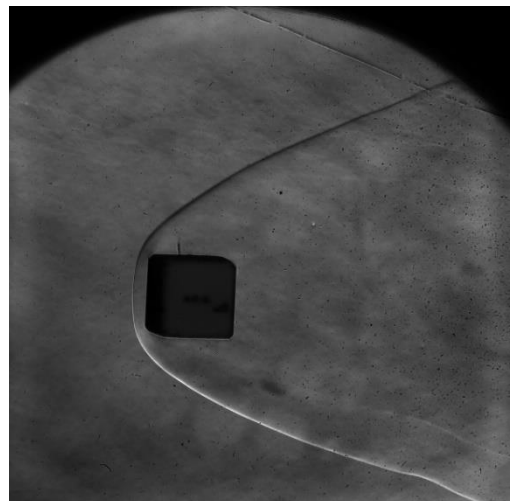
Frame 500



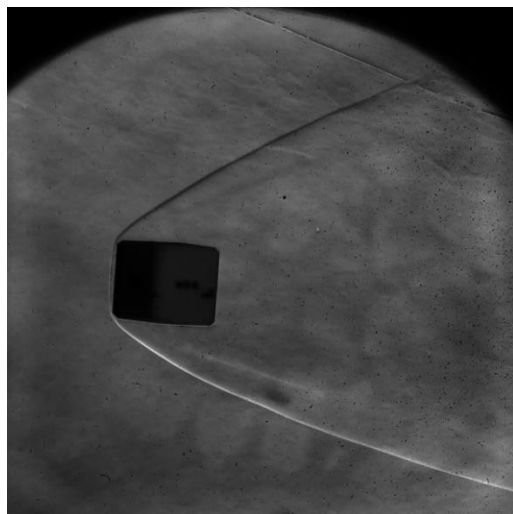
Frame 575



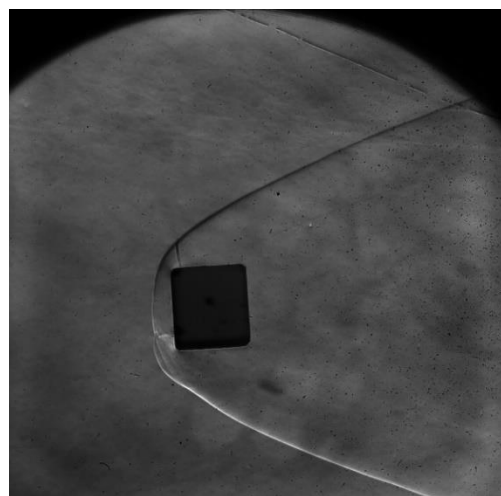
Frame 600



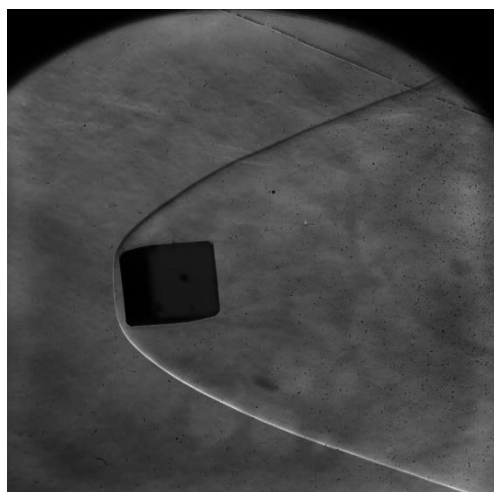
Frame 675



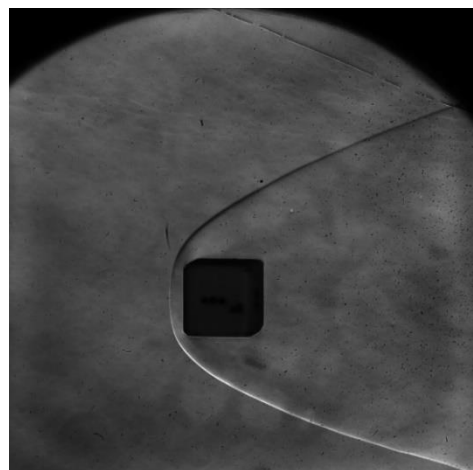
Frame 625



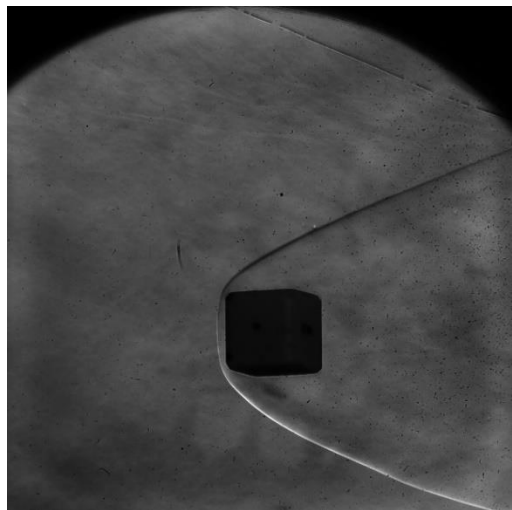
Frame 700



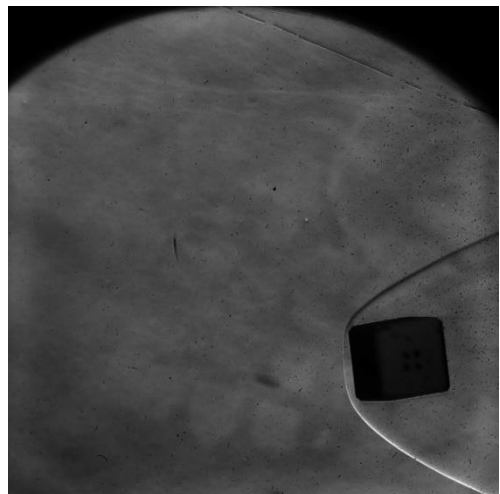
Frame 650



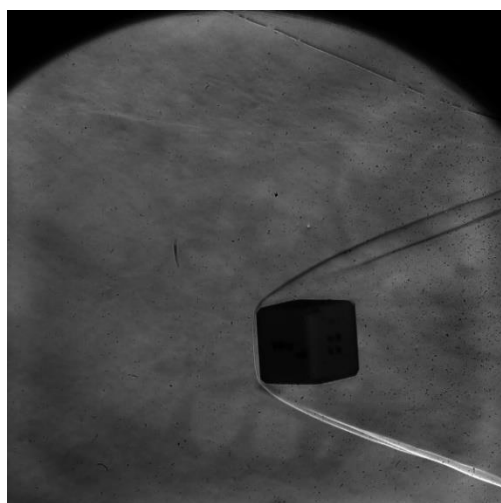
Frame 725



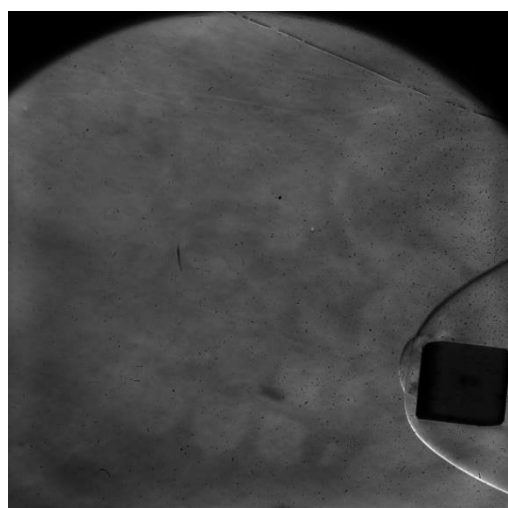
Frame 750



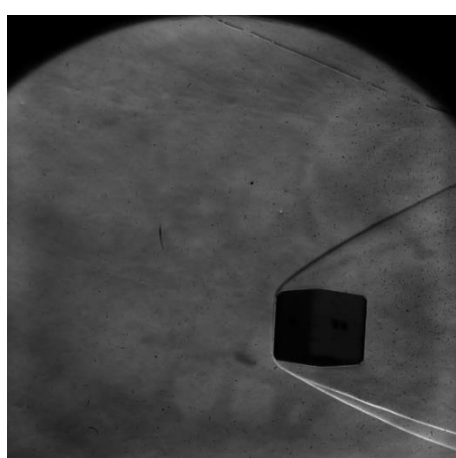
Frame 825



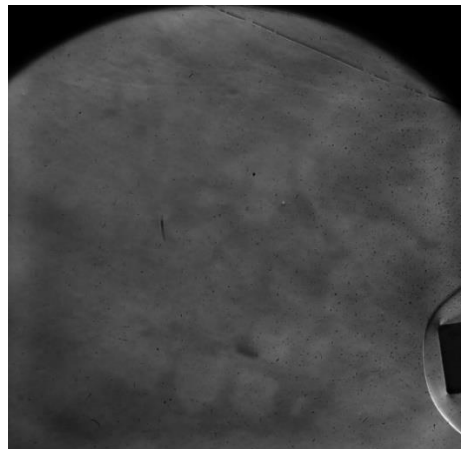
Frame 775



Frame 850



Frame 800



Frame 875

Figure F.4: Final Test Images/Snapshots.

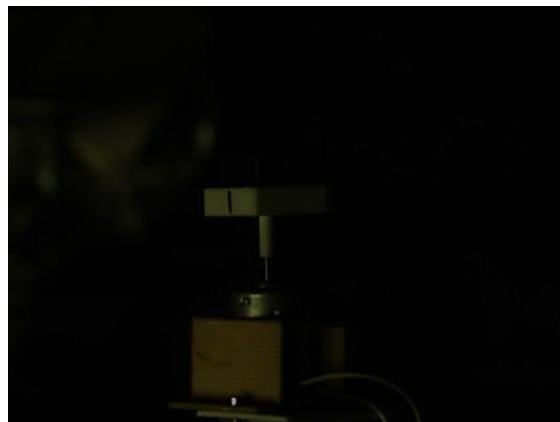
Appendix F.2 Preliminary/Bench Test Load 20 Percent



Frame 1



Frame 60



Frame 20



Frame 80



Frame 40



Frame 101



Frame 121



Frame 140

Figure F.5: 20 Percent Load Preliminary/Bench Test Images/Snapshots.

Appendix F.3 Preliminary/Bench Test Load 30 Percent



Frame 1



Frame 60



Frame 20



Frame 80



Frame 40



Frame 100



Frame 120



Frame 160



Frame 140

Figure F.6: 30 Percent Load Preliminary/Bench Test Images/Snapshots.

Appendix F.4 Preliminary/Bench Test Load 40 Percent



Frame 1



Frame 60



Frame 20



Frame 80



Frame 40



Frame 100



Frame 120



Frame 150



Frame 140

Figure F.7: 40 Percent Load Preliminary/Bench Test Images/Snapshots.

Appendix F.5 Preliminary/Bench Test Load 50 Percent



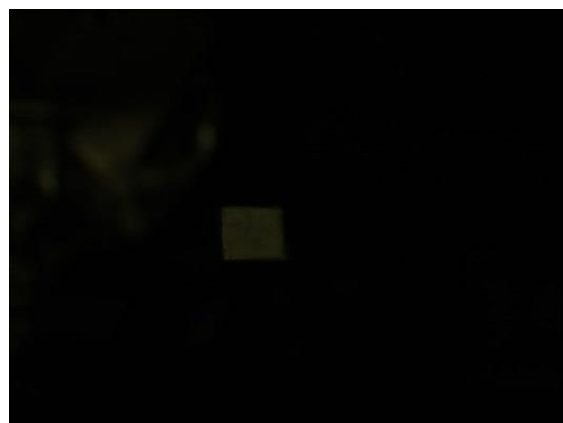
Frame 1



Frame 60



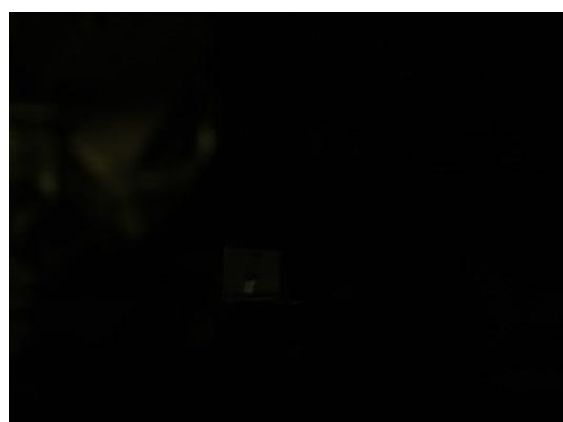
Frame 20



Frame 80



Frame 40



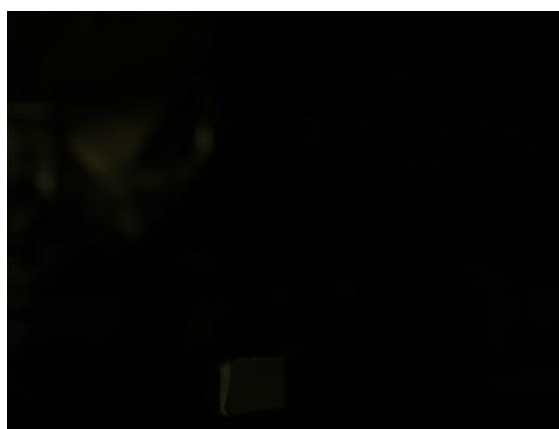
Frame 100



Frame 120



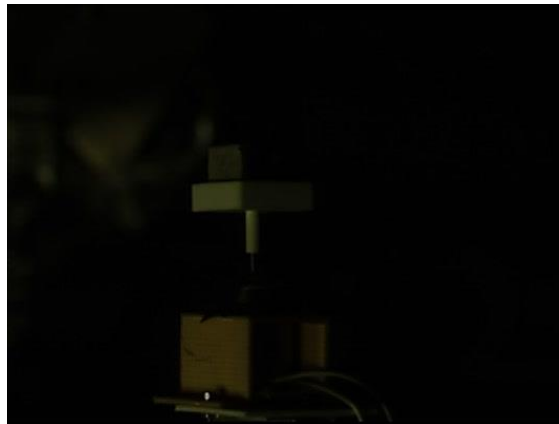
Frame 150



Frame 140

Figure F.8: 50 Percent Load Preliminary/Bench Test Images/Snapshots.

Appendix F.6 Preliminary/Bench Test Load 60 Percent



Frame 1



Frame 60



Frame 20



Frame 80



Frame 40



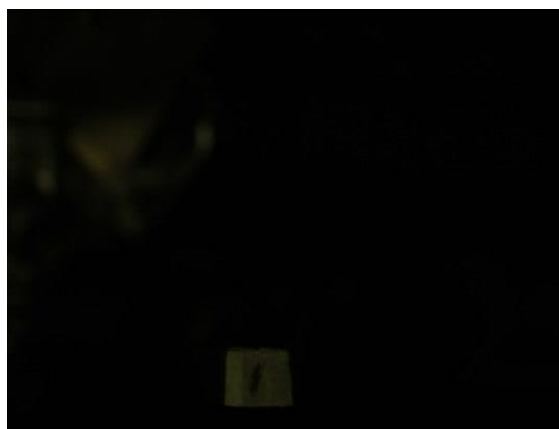
Frame 100



Frame 120



Frame 150



Frame 140

Figure F.9: 60 Percent Load Preliminary/Bench Test Images/Snapshots.

Appendix F.7 Preliminary/Bench Test Load 70 Percent



Frame 1



Frame 60



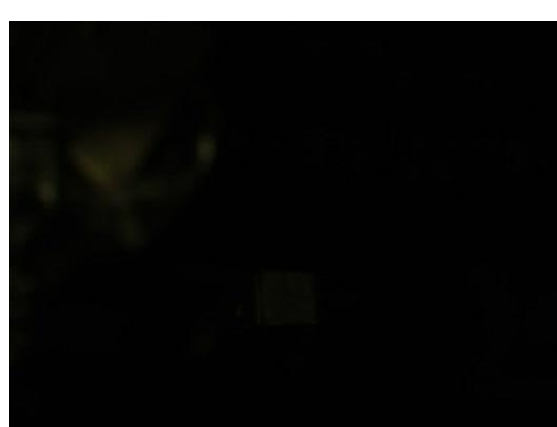
Frame 20



Frame 80



Frame 40



Frame 100



Frame 120



Frame 150



Frame 140

Figure F.10: 70 Percent Load Preliminary/Bench Test Images/Snapshots.

Appendix F.8 Preliminary/Bench Test Load 80 Percent



Frame 1



Frame 60



Frame 20



Frame 80



Frame 40



Frame 100



Frame 120



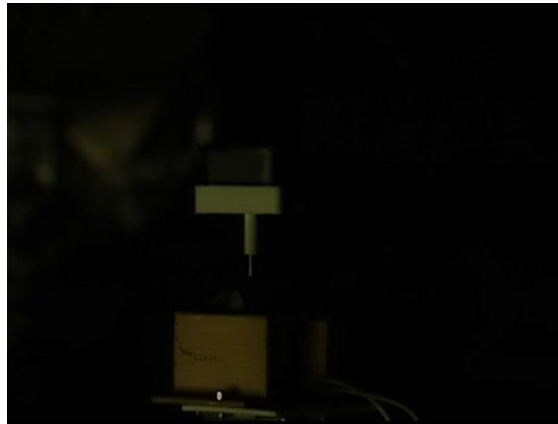
Frame 150



Frame 140

Figure F.11: 80 Percent Load Preliminary/Bench Test Images/Snapshots.

Appendix F.9 Preliminary/Bench Test Load 90 Percent



Frame 1



Frame 60



Frame 20



Frame 80



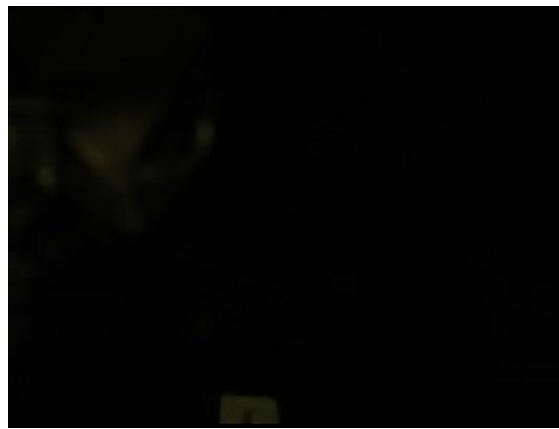
Frame 40



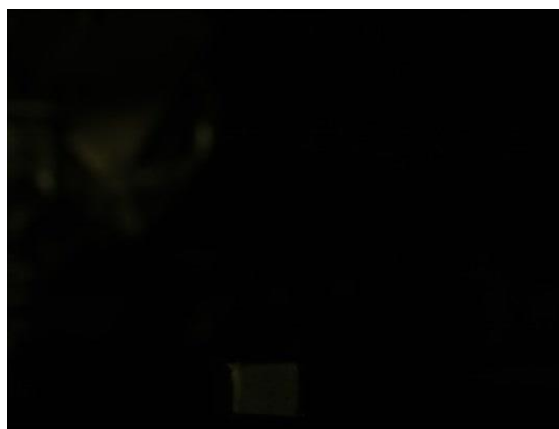
Frame 100



Frame 120



Frame 150



Frame 140

Figure F.12: 90 Percent Load Preliminary/Bench Test Images/Snapshots.

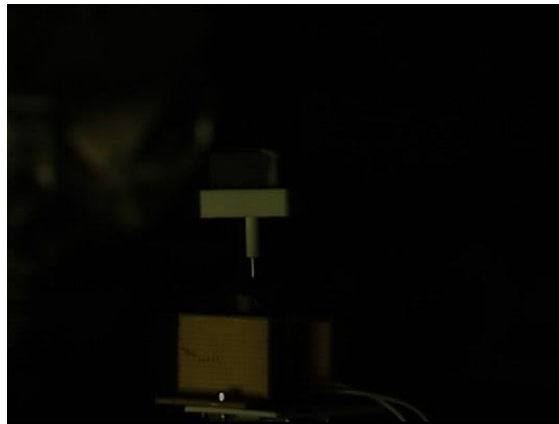
Appendix F.10 Preliminary/Bench Test Load 100 Percent



Frame 1



Frame 60



Frame 20



Frame 80



Frame 40



Frame 100



Frame 120



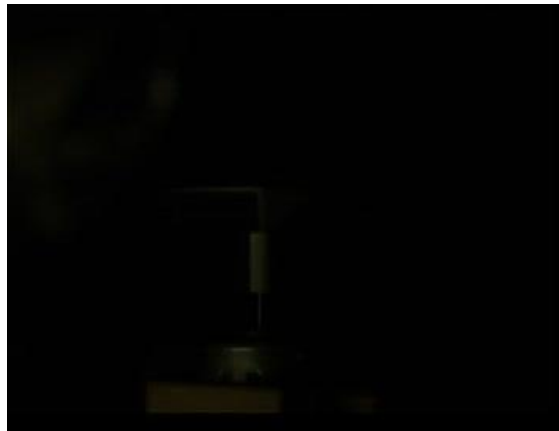
Frame 150



Frame 140

Figure F.13: 100 Percent Load Preliminary/Bench Test Images/Snapshots.

Appendix F.11 Preliminary/Bench Test No Load



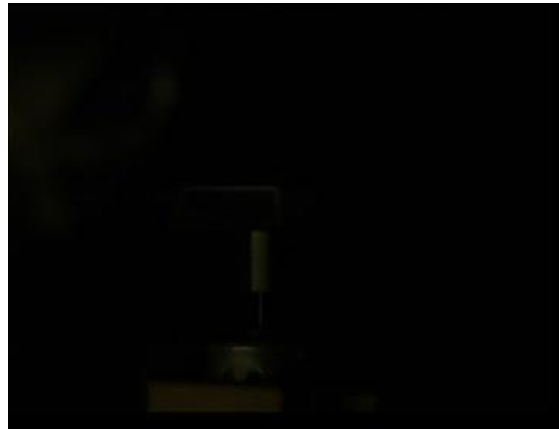
Frame 1



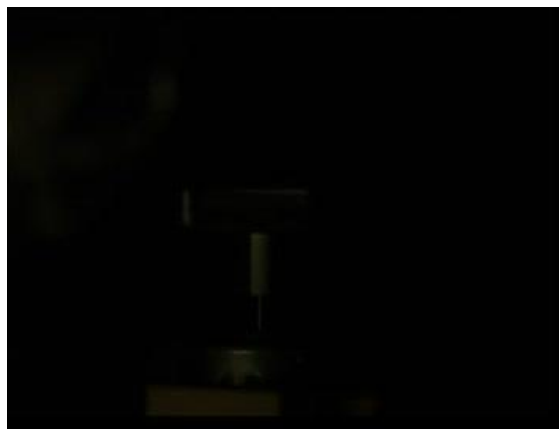
Frame 120



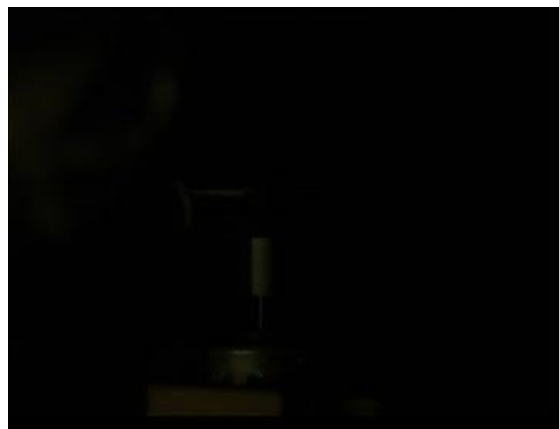
Frame 40



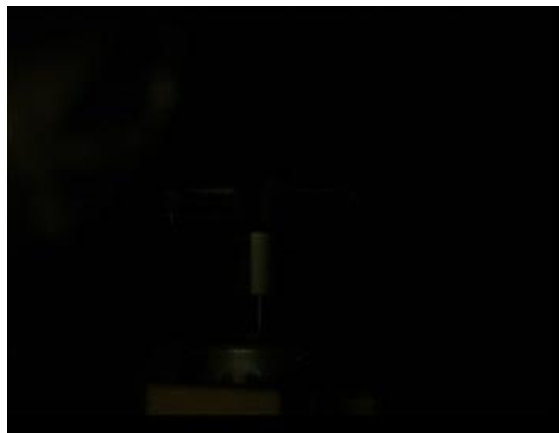
Frame 160



Frame 80



Frame 200



Frame 240

Figure F.14: No Load Preliminary/Bench Test Images/Snapshots.

Appendix G Calculations of Test Objects

Appendix G.1 General Calculations for all Test Objects

Calculating the acceleration of all of the test object's:

Assume:

$$d_{travelled} \approx 2 \text{ m}$$

$$t \approx 0.2 \text{ sec} = 200 \text{ ms}$$

$$d = ut + 0.5at^2 \quad (\text{G.1})$$

$$2 = 0 \times 0.2 + 0.5a \times 0.2^2$$

$$a = \frac{2}{0.5 \times 0.2^2}$$

$$a = 100 \text{ m/s}^2$$

Therefore, the acceleration of all of the test objects is 100 m/s^2 .

Appendix G.2 Theoretical Cube Calculations

Theoretical calculations for the cube test object:

Assume:

$$S = 0.0254 \text{ m}$$

$$C_d = 1.05$$

$$\rho v^2 = 31.8 \text{ kPa}$$

$$\mu \approx 0.2$$

Calculating the force applied to the cube:

$$F = PA \quad (\text{G.2})$$

$$F = 31.8 \times 10^3 \times 0.0254^2$$

$$F = 20.516088 \text{ N}$$

Therefore, the force applied to the cube is 20.516088 N.

Calculating the required mass of the cube:

$$F = ma \quad (\text{G.3})$$

$$m = \frac{F}{a}$$

$$m = \frac{20.516088}{100}$$

$$m = 0.20516088 \text{ kg}$$

Therefore, the required mass of the cube is 0.20516088 kg.

Calculating the drag force of the cube:

$$F_{drag} = \frac{c_D \rho v^2 A}{2} \quad (\text{G.4})$$

$$F_{drag} = \frac{1.05 \times 31.8 \times 10^3 \times 0.0254^2}{2}$$

$$F_{drag} = 10.7709462 \text{ N}$$

Therefore, the drag force of the cube is 10.7709462 N.

Calculating the frictional force of the cube:

$$F_f = \mu F \quad (\text{G.5})$$

$$F_f = \mu mg$$

$$F_f = 0.2 \times 0.20516088 \times 9.81$$

$$F_f = 0.4025256466 N$$

Therefore, the frictional force of the cube is 0.4025256466 N.

Appendix G.3 Theoretical Sphere Calculations

Theoretical calculations for the sphere test object:

Assume:

$$\rho v^2 = 31.8 \text{ kPa}$$

$$\mu \approx 0.2$$

$$C_d = 0.45$$

$$r = 0.0127 \text{ m}^2$$

Calculating the force applied to the sphere:

$$F = PA \quad (\text{G.6})$$

$$F = 31.8 \times 10^3 \times \frac{4}{2} \pi r^2$$

$$F = 31.8 \times 10^3 \times \frac{4}{2} \pi \times 0.0127^2$$

$$F = 32.22659567 N$$

Therefore, the force applied to the sphere is 32.22659567 N.

Calculating the required mass of the sphere:

$$F = ma \quad (\text{G.7})$$

$$m = \frac{F}{a}$$

$$m = \frac{32.22659567}{100}$$

$$m = 0.3222659567 \text{ kg}$$

Therefore, the required mass of the sphere is 0.315702153 kg.

Calculating the drag force of the sphere:

$$F_{drag} = \frac{C_D \rho v^2 A}{2} \quad (\text{G.8})$$

$$F_{drag} = \frac{C_D \rho v^2 \frac{4}{2} \pi r^2}{2}$$

$$F_{drag} = \frac{0.45 \times 31.8 \times 10^3 \times \frac{4}{2} \pi \times 0.0127^2}{2}$$

$$F_{drag} = 3.625492013 \text{ N}$$

Therefore, the drag force of the sphere is 3.625492013 N.

Calculating the frictional force of the sphere:

$$F_f = \mu F \quad (\text{G.9})$$

$$F_f = \mu mg$$

$$F_f = 0.2 \times 0.3222659567 \times 9.81$$

$$F_f = 0.632285807 \text{ N}$$

Therefore, the frictional force of the sphere is 0.632285807 N.

Appendix G.4 Theoretical Cylinder Calculations

Theoretical calculations for the cylinder test object:

Assume:

$$C_d = 1.2$$

$$\rho v^2 = 31.8 \text{ kPa}$$

$$\mu \approx 0.2$$

$$r = 0.01 \text{ m}$$

$$h = 0.0254 \text{ m}$$

Calculating the average surface area of the cylinder:

$$A = \frac{2\pi rh + 2\pi r^2}{4} \quad (\text{G.10})$$
$$A = \frac{2\pi \times 0.01 \times 0.0254 + 2\pi \times 0.01^2}{4}$$
$$A = 0.00055606189 \text{ m}^2$$

Therefore, the surface area of the cylinder is $0.00055606189 \text{ m}^2$.

Calculating the force applied to the cylinder:

$$F = PA \quad (\text{G.11})$$

$$F = 31.8 \times 10^3 \times 0.00055606189$$

$$F = 17.6827681 \text{ N}$$

Therefore, the force applied to the cylinder is 17.6827681 N .

Calculating the required mass of the cylinder:

$$F = ma \quad (\text{G.12})$$

$$m = \frac{F}{a}$$

$$m = \frac{17.6827681}{100}$$

$$m = 0.176827681 \text{ kg}$$

Therefore, the required mass of the cylinder is 0.176827681 kg.

Calculating the drag force of the cylinder:

$$F_{drag} = \frac{c_D \rho v^2 A}{2} \quad (\text{G.13})$$

$$F_{drag} = \frac{1.2 \times 31.8 \times 10^3 \times 0.00055606189}{2}$$

$$F_{drag} = 10.60966086 \text{ N}$$

Therefore, the drag force of the cylinder is 10.60966086 N.

Calculating the frictional force of the cylinder:

$$F_f = \mu F \quad (\text{G.14})$$

$$F_f = \mu mg$$

$$F_f = 0.2 \times 0.1768276817 \times 9.81$$

$$F_f = 0.3469359115 \text{ N}$$

Therefore, the frictional force of the cylinder is 0.3469359115 N.

Appendix G.5 Theoretical Rectangle Calculations

Theoretical calculations for the rectangle test object:

Assume:

$$C_d = 2.05$$

$$\rho v^2 = 31.8 \text{ kPa}$$

$$\mu \approx 0.2$$

$$S = 0.02 \text{ m}$$

$$h = 0.0254 \text{ m}$$

Calculating the average surface area of the rectangle:

$$A = \frac{2S + 4Sh}{4} \quad (\text{G.15})$$

$$A = \frac{2 \times 0.02^2 + 4 \times 0.02 \times 0.0254}{6}$$

$$A = 0.000472 \text{ m}^2$$

Therefore, the surface area of the rectangle is 0.000472 m².

Calculating the force applied to the rectangle:

$$F = PA \quad (\text{G.16})$$

$$F = 31.8 \times 10^3 \times 0.000472$$

$$F = 15.0096 \text{ N}$$

Therefore, the force applied to the rectangle is 15.0096 N.

Calculating the required mass of the rectangle:

$$F = ma \quad (\text{G.17})$$

$$m = \frac{F}{a}$$

$$m = \frac{15.0096}{100}$$

$$m = 0.150096 \text{ kg}$$

Therefore, the required mass of the rectangle is 0.150096 kg.

Calculating the drag force of the rectangle:

$$F_{drag} = \frac{C_D \rho v^2 A}{2} \quad (\text{G.18})$$

$$F_{drag} = \frac{2.05 \times 31.8 \times 10^3 \times 0.000472}{2}$$

$$F_{drag} = 15.38484 \text{ N}$$

Therefore, the drag force of the rectangle is 15.38484 N.

Calculating the frictional force of the rectangle:

$$F_f = \mu F \quad (\text{G.19})$$

$$F_f = \mu mg$$

$$F_f = 0.2 \times 0.150096 \times 9.81$$

$$F_f = 0.294488352 \text{ N}$$

Therefore, the frictional force of the rectangle is 0.294488352 N.

References

- Anbu Serene Raj, C & et al 2020, 'Aerodynamics of ducted re-entry vehicles', *Chinese Journal of Aeronautics*, vol. 33, no. 7, pp. 1837-1849, viewed 21st March 2021, <<https://www.sciencedirect.com/science/article/pii/S1000936120300844?via%3Dihub>>.
- Anderson, J D 2019, *Hypersonic and High-Temperature Gas Dynamics*, 3rd edn, American Institute of Aeronautics and Astronautics, United States.
- Birch, B JC 2019, *Characterisation of the USQ Hypersonic Facility Freestream*, PhD thesis, University of Southern Queensland, Toowoomba.
- Bryce Space and Technology 2019, *Global Space Industry Dynamics*, Report, Australia, viewed 25th April 2021, <https://www.industry.gov.au/sites/default/files/2019-03/global_space_industry_dynamics_-_research_paper.pdf>.
- Carvill, J 1993, 'Fluid mechanics', *Mechanical Engineer's Data Handbook*, pp. 146-171, viewed 21st July 2021, <<https://www.sciencedirect.com/science/article/abs/pii/B9780080511351500091>>.
- Cobb, W W 2019, *How SpaceX lowered costs and reduced barriers to space*, The Conversation, viewed 21st April 2021, <<https://theconversation.com/how-spacex-lowered-costs-and-reduced-barriers-to-space-112586>>.
- Dowling, D, Carew, A & Hadgraft 2013, *Engineering Your Future An Australian Guide*, 2nd edn, John Wiley & sons Australia, Australia.
- Duffy, K 2021, *Elon Musk's SpaceX wins 2 Pentagon contracts for nearly \$160 million to Launch missions with its Falcon 9 rockets*, Business Insider Australia, 21st April 2021, <<https://www.businessinsider.com.au/elon-musk-spacex-won-two-pentagon-contracts-launch-military-rockets-2021-3?r=US&IR=T>>.
- European Space Agency 2021, *Space debris by the numbers*, Darmstadt, viewed 20th April 2021, <http://www.esa.int/Safety_Security/Space_Debris/Space_debris_by_the_numbers>.
- Federal Aviation Administration 2003, *Re-entry Corridor*, Book Chapter, viewed 18th April 2021, <https://www.faa.gov/about/office_org/headquarters_offices/avs/offices/aam/cami/library/online_libraries/aerospace_medicine/tutorial/media/iii.4.1.7_returning_from_space.pdf>.
- Federal Aviation Administration 2003, *Returning from Space: Re-entry*, Book Chapter, viewed 18th April 2021,

<https://www.faa.gov/about/office_org/headquarters_offices/avs/offices/aam/cami/library/online_libraries/aerospace_medicine/tutorial/media/iii.4.1.7_returning_from_space.pdf>.

Federal Aviation Administration 2003, *Vehicle Re-entry Velocity Profile*, Book Chapter, viewed 18th April 2021,

<https://www.faa.gov/about/office_org/headquarters_offices/avs/offices/aam/cami/library/online_libraries/aerospace_medicine/tutorial/media/iii.4.1.7_returning_from_space.pdf>.

Federal Aviation Administration 2016, *Effect of Drag Form when Streamlining Design*, Handbook, Department of Transport, Oklahoma City, viewed 18th July 2021, <https://www.faa.gov/regulations_policies/handbooks_manuals/aviation/phak/>.

Federal Aviation Administration 2016, *Pilot's Handbook of Aeronautical Knowledge*, no. 1, U.S. Department of Transport, Oklahoma City, viewed 18th July 2021, <https://www.faa.gov/regulations_policies/handbooks_manuals/aviation/phak/>.

Fritzsche, B, Lips, T & Koppenwallner, G 2007, 'Analytical and numerical re-entry analysis of simple shaped objects', *Acta Astronautica*, vol. 60, no. 6-9, pp. 737-751, viewed 21st March 2021, <<https://www.sciencedirect.com.ezproxy.usq.edu.au/science/article/pii/S0094576506002682>>.

National Aeronautics and Space Administration 2021, *Forces on an Airplane*, website, National Aeronautics and Space Administration, viewed 18th July 2021, <<https://www.grc.nasa.gov/www/k-12/airplane/forces.html>>.

Nilsson, H M & Aarønæs, A S 2014, *Dynamic response of pipe rack steel structures to explosion loads*, Master's Thesis, Chalmers University of Technology, Sweden, viewed 8th September 2021, <<https://www.semanticscholar.org/paper/Dynamic-response-of-pipe-rack-steel-structures-to-Nilsson-Aar%C3%B8n%C3%A6s/94acace29ad923ce8933de088524e46ec1ebe21c#extracted>>.

O'Carroll, L 2011, 'Nasa satellite has fallen to Earth', *The Guardian*, viewed 21st April 2021, <<https://www.theguardian.com/science/2011/sep/24/nasa-satellite-uars-falls-to-earth>>.

Organisation for Economic and Co-operation and Development 2020, *Measuring the Economic Impact of the Space Sector*, Report, Saudi Arabia, viewed 25th April 2021, <<https://www.oecd.org/innovation/inno/measuring-economic-impact-space-sector.pdf>>.

Pardini, C & Anselmo, L 2019, 'Uncontrolled re-entries of space craft and rocket bodies: A statistical overview over the last decade', *Journal of Space Safety Engineering*, vol. 6, no. 1, pp. 30-47, viewed 15th September 2021, <<https://www.sciencedirect.com/science/article/abs/pii/S2468896718300788>>.

Park, S & Park, G 2020, ‘Separation process of multi-spheres in hypersonic flow’, *Advances in Space Research*, vol. 65, no. 1, pp. 392-406, viewed 21st March 2021, <<https://www.sciencedirect.com.ezproxy.usq.edu.au/science/article/pii/S0273117719307422>>.

Potter, N 2011, ‘NASA UARS Satellite Crashes Into Earth: Location Unknown’, *ABC News*, viewed 21st April 2021, <<https://abcnews.go.com/Technology/nasa-uars-satellite-crashes-earth-location-unknown/story?id=14595092>>.

Pritchard, P J & Mitchell, J W 2015, *Introduction to Fluid Mechanics*, 9th ed, John Wiley & Sons, United States of America.

Reyhanoglu, M & Alvarado, J 2013, ‘Estimation of debris dispersion due to a space vehicle breakup during re-entry’, *Acta Astronautica*, vol. 86, pp. 211-218, viewed 21st March 2021, <<https://www.sciencedirect.com.ezproxy.usq.edu.au/science/article/pii/S0094576513000301>>.

Rourke, A 2021, ‘Out-of-control’ Chinese rocket falling to Earth could partially survive re-entry’, *The Guardian*, 4th May 2021, viewed 15 September 2021, <<https://www.theguardian.com/science/2021/may/04/out-of-control-chinese-rocket-tumbling-to-earth>>.

Royal Museums Greenwich 2021, *Space Race Timeline*, Greenwich, viewed 20th April 2021, <<https://www.rmg.co.uk/stories/topics/space-race-timeline>>.

Sim H & Kim, K 2011, ‘Re-entry survival analysis of tumbling metallic hollow cylinder’, *Advances in Space Research*, vol. 45, no. 1, pp. 914-922, viewed 21st March 2021, <<https://www.sciencedirect.com.ezproxy.usq.edu.au/science/article/pii/S0273117711003097>>.

Sliz-Balogh, J et al 2020, ‘Dynamics of spherical space debris of different sizes falling to Earth’, *Astronomische Nachrichten*, vol. 341, no. 3, pp. 245-257, viewed 21st March 2021, <<https://onlinelibrary-wiley-com.ezproxy.usq.edu.au/doi/full/10.1002/asna.202023688>>.

The Aerospace Security Project 2020, *Payloads Launched by Country*, digital image of recorded launch data, Centre for Strategic International Studies, viewed 15 September 2021, <<https://aerospace.csis.org/data/space-environment-total-launches-country/>>.

Trisolini, M, Lewis, H G & Colombo, C 2018, ‘Spacecraft design optimisation for demise and survivability’, *Aerospace Science and Technology*, vol. 77, pp. 638-657, viewed 21st March 2021, <<https://www.sciencedirect.com.ezproxy.usq.edu.au/science/article/pii/S1270963816311476>>.

University of Newcastle 2019, *Health and Safety Risk Assessment*, Report, viewed 28th April 2021, <https://www.newcastle.edu.au/__data/assets/pdf_file/0009/342747/Risk-Management-Module.pdf>.

Wall, M 2021, ‘Huge Chinese rocket booster falls to Earth over Arabian Peninsula’, *Space.com*, 9 May 2021, viewed 15th September 2021, <<https://www.space.com/chinese-rocket-booster-long-march-5b-space-junk-crash>>.

Wasserman, T 2020, ‘A Chinese rocket weighing 18 tons falls to Earth as space junk crisis hits a tipping point’, *CNBC*, viewed 21st April 2021, <<https://www.cnbc.com/2020/05/16/chinese-rocket-falls-to-earth-space-debris-problem-worsens.html>>.

Whitley, D 2020, *Balladonia, Skylab crash site in Australia: How a fallen space station caused mayhem in the outback*, viewed 21st April 2021, <<https://www.traveller.com.au/balladonia-skylab-crash-site-in-australia-how-a-fallen-space-station-caused-mayhem-in-the-outback-h1q49r>>.

Wood, T 2020, *Who owns our orbit: Just how many satellites are there in space*, World Economic Forum, viewed 21st April 2021, <<https://www.weforum.org/agenda/2020/10/visualizing-easrth-satellites-sapce-spacex>>.

Wu, Z & et al 2011, ‘Space Debris Re-entry Analysis Methods and Tools’, *Chinese Journal of Aeronautics*, vol. 24, no. 4, pp. 387-395, viewed 21st March 2021, <<https://www.sciencedirect.com/science/article/pii/S1000936111600460?via%3Dihub>>.